UNIVERSITÀ DEGLI STUDI DI MILANO-BICOCCA

Facoltà di Scienze Matematiche, Fisiche e Naturali

Dipartimento di Fisica

Corso di Laurea Magistrale in Fisica

Monte Carlo Simulations of the TOSCA Neutron Spectrometer:

Assessment of Current Performance and Future Upgrades

Tesi di Laurea di

Roberto Simone Pinna

Matricola 708837

Relatore

Prof. Dr. Giuseppe **Gorini**

Correlatore

Dr. Svemir **Rudic**

Anno accademico 2013-2014

Contents

1. Introduction

The present thesis has been developed in partnership with ISIS, Rutherford Appleton Laboratory (Oxfordshire, UK) over a ten months of internship period abroad. The project is focused on TOSCA, a broadband indirect-geometry inelastic neutron spectrometer, optimised for high-resolution chemical spectroscopy up to energy transfers of ~500 meV in neutron-energy loss. TOSCA sample position sits at 17 m from a room-temperature water moderator at ISIS Target Station 1 (beamline N8). When TOSCA was initially constructed, consideration was given to incorporation of a neutron guide. However, at that time neutron guides typically had $m \simeq 1$ (where m denotes the reflectivity and is the ratio of the critical angle of the supermirror to that of nickel) and for the relatively hot neutrons required for vibrational spectroscopy, the small gains at low energies did not justify the investment. Neutron guides exploit total external reflection to provide a means to transport neutrons across tens of metres with greatly reduced losses as compared to a simple tube. Furthermore in the last decade, both guide technology and the ability to simulate guides have been advanced significantly.

At the moment there is increased competition in the area of molecular spectroscopy with neutrons. There are two new instruments that can study similar part of the vibrational spectrum as TOSCA: VISION at SNS (USA) and LAGRANGE at ILL (France). The instrument VISION is currently under construction and it is plausible that VISION total flux at the sample position will be 50 or 100 times the flux of TOSCA. This is due to the higher power of SNS source and the fact that VISION has a neutron guide, which directs the neutrons to the sample more effectively than the simple TOSCA collimation tube. These facts, in conjunction with the larger VISION's effective detector area and higher resolution crystal analyzers can make TOSCA less competitive in the field of neutron spectroscopy. To keep TOSCA in a leading position, the most urgent need is for a greater sensitivity of the instrument via provision of a guide in the primary spectrometer, thus a validated Monte Carlo model is needed to test the feasibility of this upgrade. Whitin this framework, the aim of this thesis is to build a detailed computational description of the TOSCA spectrometer using neutron-transport Monte Carlo simulations and assess its performance. The geometry of both primary and secondary spectrometers has been taken from current engineering drawings of the instrument and an extensive benchmarking between the experimental and simulated results has been performed in order to determine the validity of the McStas model. This analysis was performed by use of direct measurements on the instrument, involving all the systems currently exploited on TOSCA (incident beam monitor, diffractometers and INS

assembly). The agreement between expected and measured performance was shown to be satisfactory in terms of the incident flux spectrum, associated time structure, and spectroscopic resolution. Encouraged by the results of the computational model, we eventually proceeded in simulating the potential flux gain associated with the upgrade of the primary spectrometer with a tapered high-m guide. This instrument development offers the exciting prospects of providing order-of-magnitude gains in detected neutron flux over the energy-transfer range of the instrument whilst preserving its outstanding spectroscopic capabilities. Such an increase in incident flux implies an order-of-magnitude reduction in counting times or sample quantity, it would also facilitate the study of non-hydrogenous materials. All Monte Carlo simulations have been performed using the parallelised version of the McStas software package (built to allow the design of components for neutron spectrometers). Computations were performed on the SCARF-RAL cluster using up to 128 nodes.

Given the results assessed in this thesis and the clear benefits for TOSCA, the upgrade was recently endorsed by an International Review Panel who recommended: *"The panel agreed that the guide upgrade has to be taken up with the highest priority"*. The implementation of a guide on TOSCA combined with the planned upgrade of the first target station at ISIS will deliver an instrument that will continue to be at the forefront of vibrational spectroscopy with neutrons for a foreseeable future.

The author can be contacted at pinna.roberto.simone@gmail.com.

The results achieved in this thesis have been presented in the following reports and publications:

- S. Rudic, A.J. Ramirez-Cuesta, S.F. Parker, F. Fernandez-Alonso, R.S. Pinna, G. Gorini, C.G. Salzmann, S.E. McLain, N.T. Skipper, TOSCA International Beamline Review, RAL Technical Reports RAL-TR-2013-015 (2013). Report available at: https://epubs.stfc.ac.uk/work/11216706

- S.F. Parker, F. Fernandez-Alonso, A.J. Ramirez-Cuesta, S. Rudic, R.S. Pinna, G. Gorini, J. Fernandez Castañon, Recent and Future Developments on TOSCA at ISIS, *J. Phys.: Conf. Ser.* in press (2014).

- R.S. Pinna, S. Rudic, S.F. Parker, G. Gorini, F. Fernandez-Alonso, Monte Carlo Simulations of the TOSCA Spectrometer: Assessment of Current Performance and Future Upgrades, *Eur. Phys. J. Web of Conferences* in press (2014).

2. Neutron scattering

2.1. Overview

The first neutron scattering experiment was performed in the 1940s on fission reactors, even though they were built for different purposes such as radioisotopes production. Since then the community of neutron users has expanded constantly. Crystallographers were the first soon followed by condensed matter physicists interested in magnetic and vibrational properties of crystals. Later chemists, biologists and more recently engineers and earth scientists joined the community. These kind of studies are performed at large scale facilities that have capability to produce an intense neutron beam. In the early years of neutron scattering, nuclear reactors were the main neutron sources, but today accelerator-based pulsed sources have achieved equal prominence. The following chapter describes the neutron properties, with particular attention on thermal neutrons. Then the basic theory of neutron scattering is briefly introduced. Section 2.3 is significant for the remainder of this thesis, as it relates to the theory governing the reflection of a neutron by a guide.

2.2. Neutron properties

The neutron is a subatomic hadron particle and its existence was first predicted by Ernest Rutherford in 1920's and it was finally discovered by James Chadwick in 1932. The interaction of neutrons depends on their energy (see Tab. 2.1), hence neutrons can be classified depending on their kinetic energy. Thermal neutron properties allow experiments very different from other techniques, such as X-rays and Raman spectroscopy.

- Thermal neutrons have wavelength comparable to lattice spacing in solids. Therefore, they offer an ideal probe for determining the atomic arrangement in condensed matter and for studying excitations mode, such as phonons and magnons in crystals.

- They have a weak interaction with matter and thus a high penetration capability.

- The atomic scattering amplitude is not linked to the number of shell electrons, therefore the magnitude of the interaction changes for different isotopes of an element.

- The neutron magnetic moment interacts with the magnetic moment of un-paired electrons, allowing the study of magnetic properties in materials.

Classification	Kinetic energy range
High energy neutrons	> 40 MeV
Fast neutrons	100 KeV - 40 MeV
Slow neutrons	1 - 100 Kev
Epithermal neutrons	0.2 eV - 1 KeV
Thermal neutrons	0.025 eV
Cold neutrons	0 - 0.025 eV

Table 2.1. – Classification of neutrons depending on energy [30].

Lifetime τ	886 ± 1 s
Rest mass m_n	939.57 MeV
Wavelength λ	1.798 Å at 2200 m/s
Energy E	25.3 meV at 2200 m/s
Spin S	1/2
Magnetic moment μ_n	-1.913043 nuclear magnetons

Table 2.2. – Main properties of the neutron [30].

The wavelength λ of a neutron is related to its velocity v through the de Broglie relation Eq. 2.1 [30].

$$\lambda = \frac{h}{m_n v} \tag{2.1}$$

2.2.1. Lifetime

A free neutron is not a stable particle and it undergoes radioactive decay. It is a beta-emitter, decaying spontaneously into a proton, an electron and an electron anti-neutrino Eq. 2.2 [30].

$$n \rightarrow p^+ + e^- + \overline{\nu}_e \tag{2.2}$$

The neutron lifetime, see Tab. 2.2, is denoted by parameter τ and corresponds to the time after which $1/e$, or 0.37 of the original population remains.

$$N(t) = N(0)e^{-\frac{t}{\tau}} \tag{2.3}$$

In a typical neutron scattering experiment, the time taken by neutrons to traverse the distance from source to detector is much less than their half-life. Thus a thermal neutron with velocity of 2200 m/s takes only 45 ms to travel 100 m, and consequently the fraction of neutrons decaying in this period of time is negligible. It is safe to assume that the lifetime of the neutron is of no practical significance in a scattering experiment.

2.2.2. Energy

By means of the de Broglie law it is possible to relate the wavelength and the kinetic energy of a neutron. Hence the corresponding kinetic energy E, which is $\frac{1}{2}mv^2$, is given by

$$E = \frac{h^2}{2m_n\lambda^2} \tag{2.4}$$

Assuming that $E = k_bT$, where E is in eV and T is in Kelvin, it results that at room temperature, 300 K, the energy of a thermalized neutron in a water moderator is distributed around 0.025 eV.

The atoms in a solid material are not perfectly stationary: the thermal motion can move an atom from its equilibrium position and waves that propagate in the lattice of the solid are created. The energy associated with these waves is quantized in energy quanta called phonon, phonons are collective excitations of the crystal lattice. In the inelastic scattering of neutrons, an exchange of energy causes these excitations thus a phonon is generated or absorbed in the sample and the neutron loses or gains that amount of energy. Neutrons also exchange energy, causing vibrations and rotations of molecules, diffusion processes of particles in the solid and magnetic excitations. Thermal neutrons are used to study these excitations, as the typical exchange of energy is of the same order of magnitude as the initial kinetic energy of the neutrons.

2.2.3. Magnetic moment

The magnetic moment of a neutron is only 1/1000 of the magnetic moment associated with the spin of an electron [30]. Notwithstanding this fact, the magnetic moment of the neutron can interact with unpaired electrons in magnetic atoms.

Elastic magnetic scattering (or magnetic diffraction) studies concentrate on magnetic structures, that is the arrangement of the magnetic moments of atoms in the lattice. Inelastic magnetic scattering yields information about the magnetic excitations, in which there are oscillations in the orientation of successive spins in the lattice. These spin waves are quantized in energy units called *magnon*s. If a magnetic field is applied along the neutron path, the neutron spin results aligned parallel or anti-parallel to it. A polarized beam is created when the number of neutrons with parallel magnetic moments (spin up) is different from the number of neutrons with anti-parallel moments (spin down). Typical way to polarize a neutron beam is by using a magnetized crystal, which has a high cross section for a certain spin state. Almost half of the neutrons are removed from the beam (and hence wasted) but on the other hand a polarized beam is obtained.

2.3. Neutron scattering

2.3.1. Elastic scattering

Let us consider scattering by a single nucleus, as shown in Fig. 2.1. Neutron can be seen as a plane wave $\psi(z) = e^{ikz}$ traveling in z direction incident to a nucleus in O. The result of the interaction is a spherical wave $\psi'(r) = -\frac{b}{r}e^{ikr}$ centered in the nucleus position. Where b is the *scattering length* of the nucleus, r the distance from the nucleus and k the wavenumber. We assume the nucleus is fixed so that the scattering is elastic.

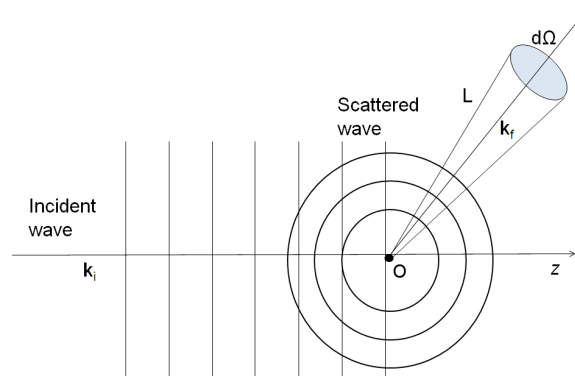**Figure 2.1.** – The scattering of a plane wave of neutrons by a single nucleus.

In the Born approximation, only a small fraction of the incidents neutrons are scattered because the nuclear potential is short range. Consider now a plane wave incident to a lattice of nuclei, each of them contributes with a diffracted wave and constructive interference occurs if the path difference between the scattered waves

equals the wavelength of the incident plane wave. The same constructive interference appears also if the path difference equals an integer multiple of the wavelength. This leads to the Bragg law, Eq. 2.5 and Fig. 2.1.

$$n\lambda = 2dsin\theta \qquad (2.5)$$
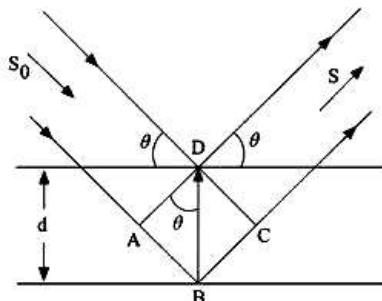
Figure 2.2. – Plane wave incident and reflected by two lattice planes at the angle θ. The constructive interference between the reflected waves occurs only if the Bragg condition is met.

Where λ is the neutron wavelength, n is an integer, d is the lattice spacing and θ is the angle of incidence.

In reality, nuclei are not stationary because of their thermal motion. This causes a decrease in intensity I of the diffracted beam because waves may not be in phase. The Bragg law is indeed affected by lattice thermal vibration, to account for this d is replaced by the average value $< d >$ and the peaks intensity I is reduced, Eq. 2.6. The so called Debye-Waller W factor is introduced to damp the scattering and it depends on the temperature of the material.

$$I = I_0 e^{-2W} \qquad (2.6)$$

2.3.2. Coherent and incoherent scattering

The scattering length b of a nucleus determines its cross section in scattering a neutron. The different isotopes of a chemical element have their own characteristic scattering lengths. The nucleus spin also influence the scattering length in relation with the spin of the incident neutron. The existence of isotopes and spin effects gives rise to cross-sections with components of coherent and incoherent scattering. As shown in Fig. 2.3, the coherent part determines interference effects and shows space and time relationships between different atoms, its pattern is composed of peaks (e.g. Bragg peaks). The incoherent part arises from the deviation of the scattering lengths from the mean value of the material, it does not cause interference so its pattern is a flat background and gives information about the properties of individual atoms [30]. The scattering differential cross section can be summarized as follow

$$\frac{d\sigma}{d\Omega} = \sum_{j,j'} <b>^2 \, exp\left[i\mathbf{Q} \cdot (\mathbf{r}_j - \mathbf{r}_{j'})\right] + \sum_{j} \left(<b^2> - <b>^2\right)_j \qquad (2.7)$$

Where $\mathbf{Q} = \mathbf{k}_i - \mathbf{k}_f$ and $\mathbf{r}_j$ is the position of the j-th nucleus.

The first summation in Eq. 2.7 describes the coherent scattering component, in which there is scattering from each nucleus in $\mathbf{r}_j, \mathbf{r}_{j'}$. In this picture each nucleus possess a scattering length equal to the average of the compound $<b>$. The second summation represents the incoherent scattering component, interference peaks are not possible and its magnitude is determined by the mean-square deviation of the scattering length from its average value [30].
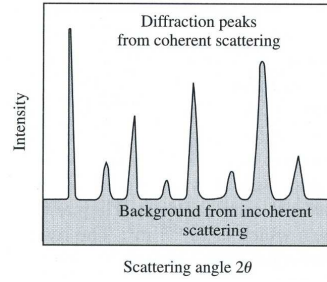
Figure 2.3. – A schematic diffraction pattern for neutron scattering [30].

2.3.3. Inelastic neutron scattering

In inelastic neutron scattering (INS) the wavevectors are $\mathbf{k}_i \neq \mathbf{k}_f$, so the momentum transferred is

$$\hbar\mathbf{Q} = \hbar\left(\mathbf{k}_i - \mathbf{k}_f\right) \qquad (2.8)$$

While the energy transferred is

$$\hbar\omega = E_i - E_f = \frac{\hbar^2}{2m}\left(\mathbf{k}_i^2 - \mathbf{k}_f^2\right) \qquad (2.9)$$

Thus a scattering event is characterized by $(\mathbf{Q}, \omega)$ and because of the energy conservation law there is only one accessible region of the $(\mathbf{Q}, \omega)$ space. Thus the scattering law results

$$\mathbf{Q}^2 = k_i^2 + k_f^2 - 2k_i k_f cos\theta \qquad (2.10)$$

Which reduces to the Bragg law for elastic scattering $(k_i = k_f)$.

2.3.4. INS spectroscopy

Nowadays, optical techniques like infrared and Raman spectroscopy are widely used for studying molecular vibrations. INS plays an important role in extending the field of research because it has some advantages in comparison to these techniques [14].

- INS measurements are useful to study hydrogen atom vibrations. In fact, the neutron incoherent scattering cross section of hydrogen is high and its signal is ten times more intense than any other atom. Optical techniques are used to investigate vibrations involving heavier atoms, because of their high Z value.

- INS techniques do not consider the rules of optical selection, all vibrations are theoretically measurable in INS. Neutrons exchange momentum during the scattering process with the atom thus INS measurements are not confined at the Brillouin zone centre, like the optical techniques are. The measured INS intensities are also sensitive to the relative concentration of components in the material.

- Neutrons are neutral and thus penetrating, while photons are easily scattered or absorbed. The penetration capability of neutrons allows the study of bulk properties in samples.

- INS spectrometers are capable to investigate the molecular vibrational range of interest (16 - 4000 cm^{-1}, see Fig. 2.4). The energy range below 400 cm^{-1} is also accessible, while infrared and Raman spectroscopies falter in this energy range.

- INS experiments can measure the neutron scattering intensity as a function of momentum and energy transfer. The spectrum is generally presented in neutron energy loss and energy is exchanged from the incident neutrons to the atoms in the material.

However, it is worth to say that neutron scattering as a spectroscopic technique is demanding of time and effort. To use this technique the experimentalists have to travel to a neutron facility with their samples and, sometimes, with their equipment. Detailed understanding of a molecular structure is achieved also by using diffraction techniques, these offer a direct approach to molecular structure. However, many systems of interest do not appear as single crystals. Wherever long range order is absent or confused, diffraction techniques are not effective and the INS spectroscopy can fulfill this task.

2.4. Neutron guides

The trajectory of a neutron is difficult to influence arbitrarily, thus the path of a neutron that reaches the sample is mostly rectilinear and the neutron flux has a

Inelastic neutron scattering spectrum
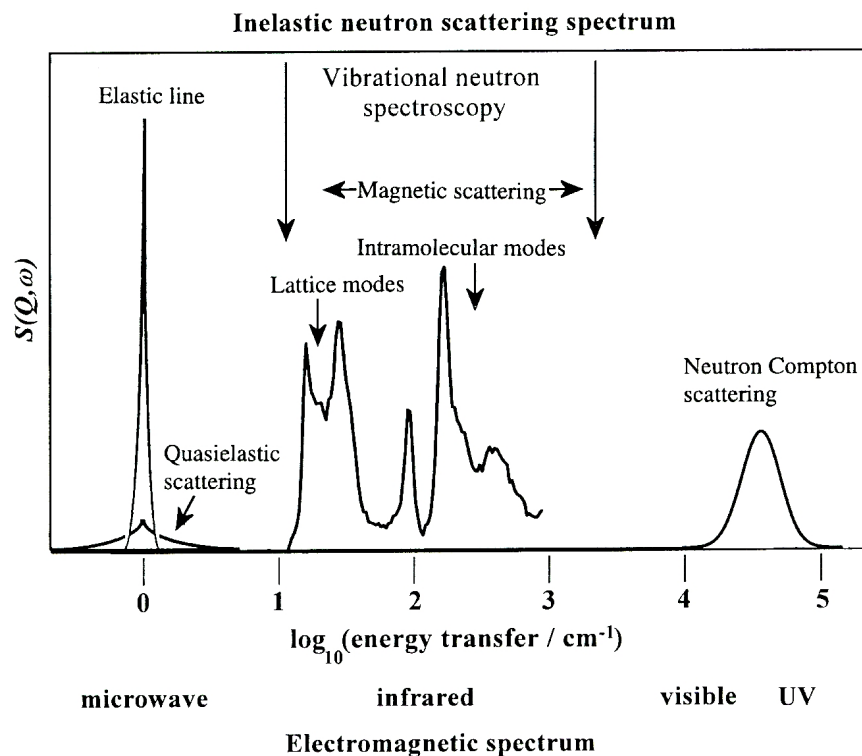
Figure 2.4. – INS spectrum in relation to optical spectroscopies. The vertical axis is the neutron scattering intensity expressed as the scattering function [14].

geometrical decrease. Along a beam-line having a distance d_i from moderator to sample, the neutron flux varies as $\frac{1}{d_i^2}$. The need to reduce d_i can be obviated, at least for instruments requiring long wavelength (low energy) neutrons, by the use of neutron guides. These are square or rectangular section tubes made from optically flat glass that has been metal coated. They work because long wavelength neutrons undergo total external reflection from the metal surface and are retained within the guide. The small critical angle of reflection γ_c relative to the guide surface, below which the reflection occurs, is given by Eq. 2.11.

$$sin\gamma_c \approx \gamma_c = \lambda \cdot \sqrt{\frac{<\rho_N><b_{coh}>}{\pi}} \tag{2.11}$$

Where λ is the neutron wavelength in Å, $<\rho_N>$ is the mean numerical density of scattering atoms and $<b_{coh}>$ is their mean coherent scattering length.

Neutron guides are used to:

- Reach higher value of neutron flux on the sample.

- Optimize the utilization of the source.

- Optimize the use of spaces.

- Curve the neutron beam (if curved guides are in use).
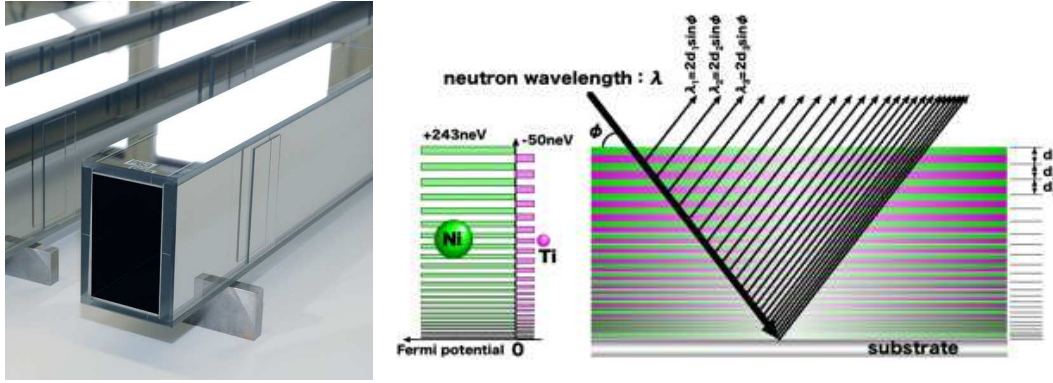
Figure 2.5. – Appearance of a supermirror neutron guide of rectangular cross section (left) and multilayer coating of a supermirror which leads to multiple constructive interference enhancing the reflection capability of the surface.

Neutron guides take advantage of the reflection of neutrons on surfaces with a refraction index higher than vacuum. The law of total reflection exists for electromagnetic waves and by virtue of the dualism between wave and particle, the total reflection is possible for neutrons too, although with much smaller angles. The preferred metal is ^{58}Ni since this has a large value of $< b_{coh} >$ and hence $\frac{\gamma_c}{\lambda} \approx 0.1\,\text{Å}^{-1}$. Although an ideal guide transports all of the flux to its exit, many of these neutrons would follow paths that diverge considerably from the central axis of the beam. A modest degree of energy selection can be introduced through the use of bent neutron guides. This kind of guides describes circumferences with a very long radius of curvature, ca. $1\,km$. Energetic neutrons fail to accomplish these gentle curves and only long wavelengths are transmitted. Unfortunately the wavelength dependence in Eq. 2.11 means that nickel guides are ineffective for the epithermal energies needed in vibrational spectroscopy. A recent development has been the use of supermirrors, which comprise alternating layers of different scattering length densities, commonly ^{58}Ni and ^{48}Ti, see Fig. 2.5. This increases the critical angle by a factor m, where m is the ratio of the critical angle of the supermirror to that of nickel. The value m has steadily improved over the last decade and the state-of-the-art supermirrors presently have $m = 7$. Such devices constitute a considerable improvements for neutron vibrational spectroscopy instruments, see Fig. 2.6. Tab. 2.3 lists the potential gains in flux for the instrument TOSCA by the use of a $m = 4$ supermirror [14]. Even at $2500\,cm^{-1}$ there is a gain of more than a factor of three and performance improves dramatically as the neutron energy diminishes. It is evident from this fact that the vibrational spectroscopy instruments should use supermirror guides rather than simple beam tubes, as evidenced for TOSCA. For supermirrors, the critical angle of reflection for neutron is predicted roughly by Eq. 2.12.

$$\gamma_c = m \cdot \lambda \cdot \sqrt{b \cdot \rho} \qquad (2.12)$$

Where b is the average scattering length of the nuclei that compound the guide walls, ρ is the density of the guide material and m is the ratio mentioned above. γ_c is evaluated between the guide surface and the direction of the incident neutron, every neutron which collides against the surface with an angle below γ_c will be likely reflected. In a coarse manner, it is possible to evaluate the critical angle for thermal and epithermal neutrons up to 0.5° in nickel guides. Therefore, because of this very small angular value, the reflection is rare but it is still suitable to guide neutrons for distances within 50 m. On TOSCA, the distance between moderator and sample is equal to 17 m, thus installing a neutron guide represents a natural upgrade path. Although, a well known problem of neutron guides consists in the increase in beam divergence at the exit of the guide, especially for tapering guides and guides with high m factor; this problem for some instruments is not negligible.

Energy (meV)	Gain
13	37
36	19
83	10
169	6
330	3.7

Table 2.3. – TOSCA preliminary gain prediction in different energy ranges after the installation of a $m = 4$ supermirror guide [14].
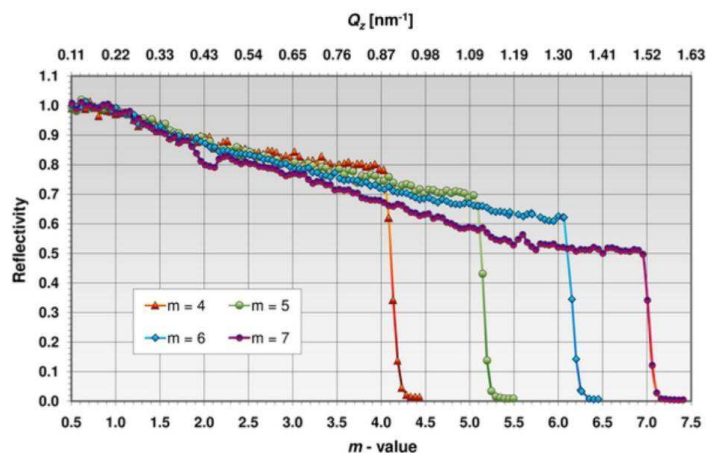
Figure 2.6. – Guide reflectivity curve for different m values. Courtesy of Swiss Neutronics.

2.4.1. Cost evaluation of a neutron guide

To the reader might be useful to understand how to compare between the effectiveness of a simulated configuration and its cost. An equation can be set to evaluate a roughly the price of a guide. The variables taken into account in this evaluation are:

- $L=$ Length of a section.
- $Ca=$ internal coating area.
- $m=$ supermirror reflectivity factor.
- $Ppl=$ price per unit of length.
- $Ppa=$ price per unit of coating area.
- $Off=$ additional cost of a section.

As a rule of thumb, we can consider that the cost of a guide section doubles for every increment in m value. Also, the cost for the shutter section is foreseen to be much higher than the other sections because of the additional cost due to the replacement of the shutter monolith and the moving mechanism. Furthermore, the shutter is radioactive and has to be handled carefully and decommissioned. For this reason a higher price offset must been set for the global cost of having a guide inside the shutter. A guide can be composed of several sections of different m values, the total price of the neutron guide is the sum over the cost of every $i-th$ section, see Eq. 2.13.

$$P = \sum_i Off_i + L_i \cdot Ppl_i + Ca_i \cdot Ppa_i \qquad (2.13)$$

2.5. Neutron detection and instrument shielding

Neutrons are unique particles because they are neutral and penetrate deeply into the matter. The consequent disadvantage is that neutrons are difficult to stop, either to detect and eliminate. On TOSCA, high efficiency ^3He detectors are in use, these unique and expensive detectors allow TOSCA to improve its use of the neutron beam.

2.5.1. Neutron detection

An important requirement of a particles detector is that it should detect only the particles of interest and an ideal detector would discriminate between particles of different energy. This is not possible in neutron detectors because they use nuclear reactions triggered by neutrons and the energy of the particle is insignificant in comparison with the energy of the reaction used. All methods rely on nuclear reactions to produce the charged particles that ionize the surrounding medium. The most useful reactions are:

$$n + {}^3He \rightarrow {}^3H + {}^1H + 0.77\,Mev \quad \sigma_{th} = 5330\,barns$$

$$n + {}^6Li \rightarrow {}^4He + {}^3H + 4.79 \, Mev \quad \sigma_{th} = 940 \, barns$$

$$n + {}^{10}B \rightarrow {}^4He + {}^7Li + \gamma(0.48 \, Mev) + 2.3 \, Mev \quad \sigma_{th} = 3840 \, barns \, B.R. = 93\%$$
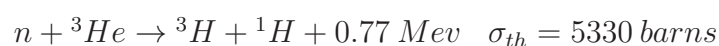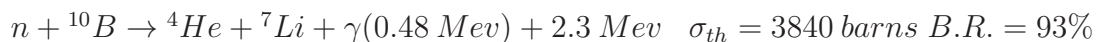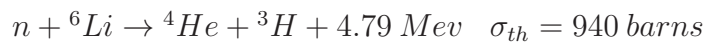
These reaction cross sections are strongly dependent on the incident neutron energy E and have roughly a $1/\sqrt{E}$ dependence [12]. Two main kind of neutron detectors exist, gas chambers and scintillation detectors. ^3He and ^{10}B (in form of BF_3) are used in gas chambers and ^6Li is used in scintillators. For research purposes the BF_3 is not widely used because of its low detection efficiency and safety, for vibrational spectroscopy ^3He gas chambers are commonly used. To reduce errors due to false detections, the electrical pulses from the detector are sorted by the electronics. The used method is to discriminate against signal that are too weak or too strong, so the fast analogue electronics set a lower and a higher level of discrimination to accept and transmit the signals in between. Every signal transmitted is stored like a count.

2.5.2. Helium detectors

Fig. 2.7a shows an example of ^3He neutron detector. The assembly consist of a earthed steel chamber filled with ^3He gas and an anode wire along the axis of the tube, the gas pressure is usually around 10 bar. Between the wire and the chamber's wall, a high voltage (1'800 V) is applied. Once a neutron crosses the chamber, if it is involved in a nuclear reaction, a proton and a triton are produced with high kinetic energy. The energetic ions cause ionization inside the chamber and the resultant charges are accelerated towards the anode generating further ionization (avalanche effect). This charge multiplication guarantees a signal gain up to 10^5 and allows the detection of a single neutron.

Fig. 2.7b shows an idealized output from a helium tube. At low energy (keV range) there are a large number of events from gamma ray ionization. One can see steps at 0.19 MeV and 0.58 MeV, and a large peak with a sharp cut-off at 0.77 MeV. Conservation of momentum requires that the proton and triton are emitted in opposite directions and the total energy released, 0.77 MeV, is partitioned as 0.58 MeV to the proton and 0.19 MeV to the triton. Because of the "wall effect" two steps are present, they correspond to the event where the triton or the proton is trapped by the detector wall before traveling a significant distance in the gas. The intense peak at 0.77 MeV is where both particles contribute to the ionization and maximize the electric pulse collected at the anode. ^3He chambers can also be arranged in an array to obtain a position sensitive detector. Discriminating which tube detects the neutron, it is possible to have informations about the position in a single direction. To measure the position along a single tube a resistive wire is used as central anode. The charge collected by a single neutron event travels along the wire towards both ends. The spatial resolution in such an assembly is typically 10-20 mm, this resolution is generally worse compared with other kind of detectors.

^3He tubes present some advantages in neutron spectroscopy, they are insensitive to gamma rays and magnetic fields and they have low background ($\approx$ 4 counts/hour for the class installed on TOSCA). Some disadvantages of this kind of detectors can be the spatial resolution mentioned above and the presence of a blind zone at both ends of the tube because of the electrical connections. It is worth to observe that these detectors are not suitable for high count-rate applications, because of the slow ion drift speed. However, for vibrational spectroscopy this is not a problem because count-rates are generally low.
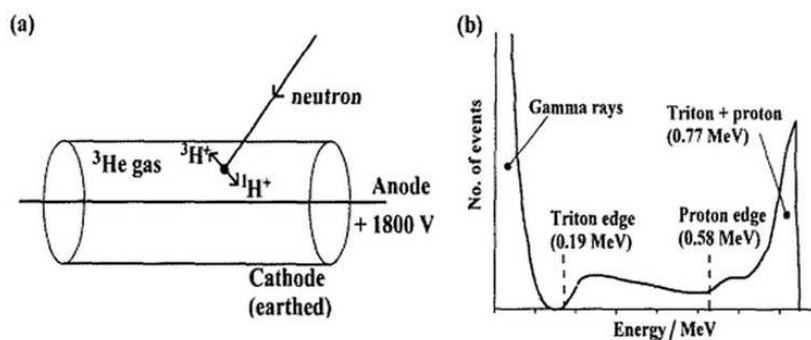
Figure 2.7. – a) Schematic of ^3He gas tube and b) its idealized pulse height spectrum.

2.5.3. Scintillator detectors

On TOSCA, a lithium glass scintillator is used as a beam monitor. All neutron instruments require beam monitors to measure the incident flux. There may also be a transmission monitor after the sample. Since the incident flux should remain as high as possible, monitors are nearly transparent to neutrons. Monitors can be either a low pressure ^3He tube or a low efficiency scintillator. For cases where the limitations of helium tubes are a problem, scintillator detectors are used. These are solid state detectors where the ^6Li is doped into a scintillating glass, usually ZnS, which emits a flash of light as the ions from the reaction pass through it. The flash is detected by a photomultiplier tube (PMT). The PMT can be attached directly to the scintillator or can be remotely coupled to it by a light pipe, lens or fiber optic system. The scintillator material is much denser than a gas so it can be much thinner (1 mm is typical), hence their spatial resolution can be much better. Unfortunately scintillators are sensitive to light and gamma rays, their PMTs also require shielding against magnetic fields.

15

2.5.4. Instrument shielding

Ideally, detectors would only be exposed to neutrons with the correct characteristics; all the other neutrons simply contribute to the instrument background and they must be reduced to a minimum. This goal is achieved by using appropriate shielding. The neutron shielding exploits the moderation process found at the source but now followed by absorption. In general, slower neutrons are more easily absorbed, in fact most materials have a $(velocity)^{-1}$ dependence to their absorption cross section. (The $1/v$ dependence is due to the fact that the slower the neutron, the longer it spends near an absorbing nucleus). As explained in [14], boron, cadmium and gadolinium are the most common materials used in neutron shielding. The three elements have different absorption behavior. Fig. 2.8 shows their absorption cross sections as a function of energy. Metal shielding materials are often chosen upon their neutron-capture resonances, most metals have several resonances, usually at MeV energies. Cadmium presents a low energy resonance (at 800 cm^{-1}), this metal is effective in absorbing low energy neutrons. Its main disadvantage is that when it absorbs neutrons, it decays emitting a gamma ray that requires further shielding. Boron is a typical $1/v$ absorber, thus it is effective for thermal neutrons and is used in mixture with a moderating compound. For bulk shielding, borated wax tanks are used; when this material solidifies it has sufficient mechanical strength to be used as a structural element in the beam-line, while having excellent shielding properties. Boron is also used as B_4C particles in resin; the resin content varies depending on the application. Low resin content (4-10 wt %) is used when it is important to absorb rather than scatter neutrons. Nevertheless, to shield small items, borated polyethylene can be used. Furthermore, gadolinium has a considerable absorption cross section at low energies and has nuclear resonances at high energies. However, it is expensive and is most often found as gadolinium paint giving a layer of shielding to fine surfaces.
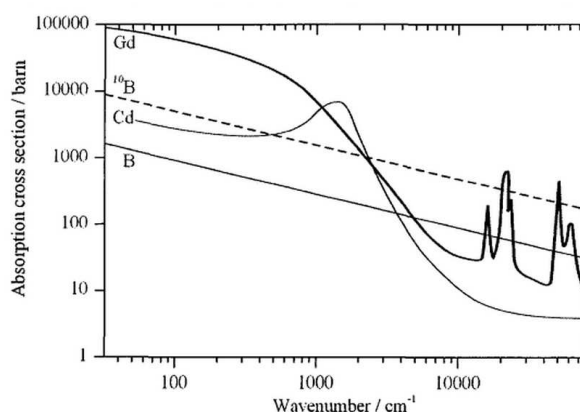
Figure 2.8. – Absorption cross section of boron, cadmium and gadolinium as a function of energy.

3. ISIS – neutron spallation source

3.1. Overview

The ISIS pulsed neutron and muon source at the Rutherford Appleton Laboratory in Oxfordshire, UK is a world-leading centre for research in the physical and biological sciences. It is owned and operated by the Science and Technology Facilities Council (STFC). ISIS produces beams of neutrons and muons that allow scientists to study materials at the atomic level by using a suite of instruments. It supports a national and international community of more than 2000 scientists who use neutrons and muons for research in physics, chemistry, materials science, geology, engineering and biology. Since the first beam produced in 1984, ISIS has become one of the UK's major scientific achievements. Across the globe, the spallation neutron sources are less common than reactor sources because spallation facilities have an increased complexity and are difficult to run and maintain. In many cases, the two types of source are complementary because of the different spectrum and brilliance they produce. The main feature of spallation sources is the pulsed nature of the beam; this allows use of time-of-flight spectrometers which can achieve high neutron energy resolution.

3.2. Spallation process

In Fig. 3.1, one can see a schematic representation of the spallation process, in which a high-energy proton pulse from an accelerator bombards a heavy material target. Protons hit the nuclei in the target and leave them in a highly excited state, causing the emission of nucleons and gamma radiation as de-excitation products. Typically a single incident proton results in about 1000 collisions in the target and its surrounding components [3]. Moreover, the incident protons can trigger an intranuclear cascade, where pions and nucleons are emitted. Some neutrons, emitted by these nuclear reactions will leave the target, whilst other neutrons will instead lead to further reactions within the target. The high-energy proton range is long, tens of cm, thus the neutron yeld is high. In fact, each proton that crosses the target causes the emission of about 20-30 neutrons [34]. This process results in a very intense neutron pulse and only a limited heat generation compared to reactor source. At ISIS spallation neutron source, the time averaged heat production within the target is about 160 kW, but during the pulse, the neutron flux exceeds that of

the most advanced steady state sources; the power of a reactor with an equivalent steady flux would be 16 GW [14]. Neutrons produced at ISIS emerge from the target with an average energy of ~ 2 MeV and theoretically they can reach energies up to the proton beam energy (800 MeV).
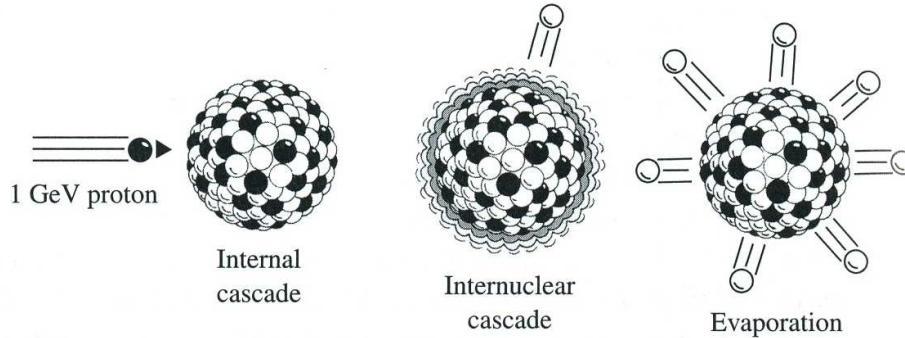
Figure 3.1. – Diagram which shows the process of proton spallation on heavy nuclei.

3.3. Proton production and acceleration

The Fig. 3.2 shows the ISIS facility, constituted from four main sections: the linac, the synchrotron, the Target Station 1 (TS-1) and Target Station 2 (TS-2). In this section are described the main processes that lead to the production of the 800 MeV proton beam.

3.3.1. Ion source

The generation of the proton beam starts in the ion source, where H^- ions are produced from a plasma discharge that causes dissociation of H_2 gas and subsequent electron transfer from a caesium-coated cathode that sits on a high voltage platform at -35 kV. The ion source uses a gaseous mixture of hydrogen and caesium; it consumes ~20 ml/minute of hydrogen gas and slightly less than ~1 g of caesium per week. The role of the caesium is to reduce the work function of the cathode, enhancing its capability to donate electrons to the positively charged hydrogen ions, and thus improving H^- production. The beam is also passed through a 90 degrees magnet to remove any free electrons from the beam. The system delivers ~50 mA H^- current pulses that are ~200–250 μs long at the repetition rate of 50 Hz. The particles energy at the end of this section is 35 keV. Typical ion source lifetime is ~4 weeks, and the time required to change an ion source is ~3 hours [9].

3.3.2. Linac

The 35 keV H^- ions are extracted by an electric field towards a quadrupole radio-frequency (RFQ) accelerator which operates at 202.5 MHz and accelerates the beam to an energy of 665 keV. The discrete bunches of H^- ions, 4.94 ns apart, are then injected into the linear accelerator (linac). Similar to the RFQ, the ions acceleration in the linac is provided by high intensity radio-frequency fields at 202.5 MHz. The linac accelerates the beam up to 70 MeV (37% of the speed of light), generating 20-25 mA pulses of H^- with duration of 200-250 μs [22]. Exiting the linac, the beam is passed through an aluminium oxide foil, 0.3 μm thick, in order to strip all the electrons from the H^- ions and thus to obtain a proton beam. The proton beam is then injected in the synchrotron.

3.3.3. Synchrotron

ISIS synchrotron is a 52 m diameter ring that for a single pulse receives the beam from the linac during 130 cycles to allow the accumulation of $4.2 \cdot 10^{13}$ protons with limited spatial charge effects [14]. Once the accumulation is completed, protons are confined in two bunches and accelerated up to 800 MeV (84% of the speed of light). This acceleration is performed in 10 ms by 10 radio-frequency resonant cavities that provide an electrical potential of 140 kV, in order to accelerate the protons at each revolution inside the accelerator ring. Simultaneously, ten dipole bending magnets keep the beam traveling on a circular orbit, and quadrupole magnets keep the beam tightly focused. The proton beam makes around 10000 revolutions before being extracted from the synchrotron by kicker magnets, in these magnets the current is raised from 0 to 5 kA within 100 ns. In this way, an intense magnetic field is generated in order to send the proton beam towards the target station. Just before the extraction from the synchrotron, the two bunches are separated by 230 ns and they have duration of 100 ns, these constitute a single beam pulse with a total time-width of 430 ns. One beam pulse is sent toward a target station every 20 ms (a frame). As shown in Fig. 3.3, all the protons from the synchrotron are then transported along a 155 m long extracted proton beam-line (EPB-1) to TS-1, or along a second proton beam-line (EPB-2, 143 m long) into which one pair out of every five pair of proton pulses is deflected by a *septum magnet* from EPB-1 and transported to TS-2 [9]. Along the EPB-1 the proton beam is lifted from the synchrotron to remove vertical and horizontal dispersions and it is shaped to produce a 70 mm spot on the target in TS-1 [3]. ISIS neutron source can reach an average proton current of 180-200 μA distributed in 50 pulses per second, a time averaged neutron flux of $2 \cdot 10^{13} \frac{n}{s\,cm^2}$ and a peak flux of $8 \cdot 10^{15} \frac{n}{s\,cm^2}$, see Fig. 3.4.
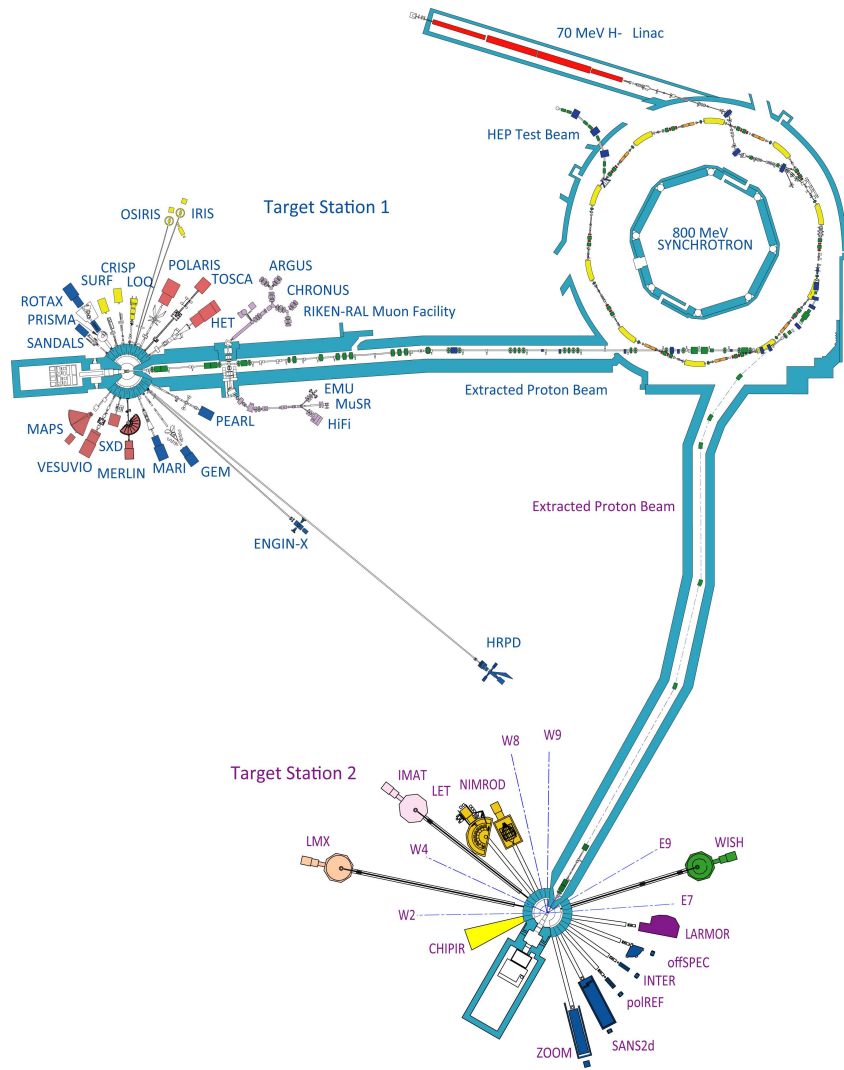
Figure 3.2. – Schematic drawing of the ISIS facility, the Linac, the Synchrotron, TS-1 and TS-2. In each target station several instruments are operational.
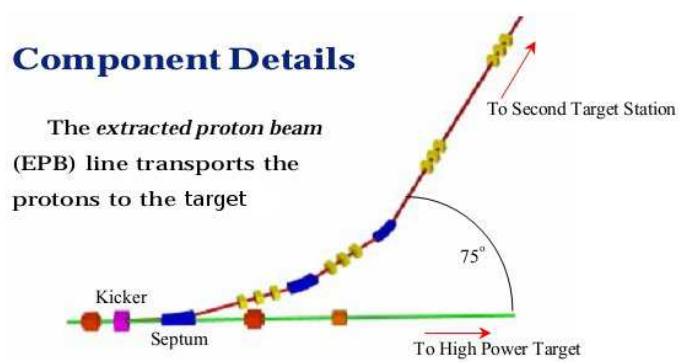
Figure 3.3. – Section of ISIS beam-line which allows the diversion of the proton beam; please note that one pulse out of five is redirected towards TS-2.
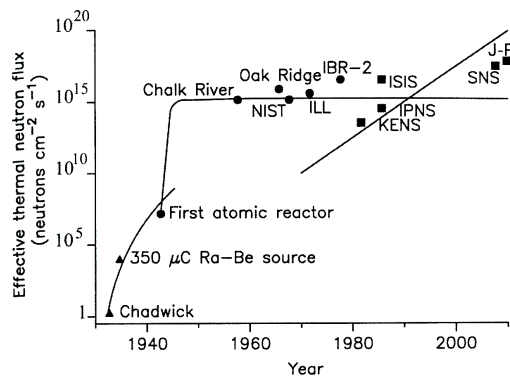
Figure 3.4. – Effective thermal neutron flux in different facilities.

3.4. Neutron production and moderation

This section presents the components dedicated to the neutron production by means of the proton beam and the subsequent neutron moderation which brings the spallation high-energy neutrons to useful energies.

3.4.1. Targets

ISIS was originally built with a depleted uranium neutron-producing target, but in the early 1990s the target material was changed to tantalum, and more recently in 2001 to tantalum-coated tungsten, see Fig. 3.5. ISIS targets are at the end of the extracted proton beam (EPB), which is ~150 m long. Each target consists of several thin plates that are surrounded by flowing D_2O acting as a coolant, which is necessary because the average heat load sustained by the target is 160 kW and its temperature can reach 600 K at the centre line [34]. The target lies within the beryllium reflector, with small moderators below and above it. Neutrons produced in the target pass through the moderators and lose their energy in each collision with the nuclei. The neutrons exiting from the moderator towards an open neutron port can reach the instrument and so can be used in experiments. Otherwise, neutrons have a chance to be reflected back into the moderator by the beryllium reflector or can possibly escape the target assembly. The target assembly is heavily confined and shielded. The biological shielding required in spallation neutron sources is larger than the one in fission reactor sources, because most of the neutrons emitted from the target remain unmoderated and thus highly energetic and very penetrating. The average energy of the neutrons emerging from the target is about 2 MeV and the duration of each fast neutron pulse is ~ 100 ns. The exact spectrum is unimportant for determining the moderated neutron spectrum, but it is fundamental to the design of the biological shielding. In TS-1, around the target there are 4 moderators and 18 beam channels, 9 per side, which feed the neutron scattering instruments.

As mentioned before, depleted uranium targets with a suitable cladding have also been used. Compared to tungsten, the use of uranium is more advantageous since it gives a larger (up to double) neutron yield per proton. That is a consequence of fission reactions that occur in uranium even after the proton pulse. As a result, the uranium target produces an almost continuous neutron beam that can be useful for some instruments, as well as detrimental for instruments which need low background. A considerable problem related to the use of uranium targets is that under the conditions they are subjected to during the spallation process anisotropic crystallization of the material itself occurs. This can lead to the puncture of the cladding and the consequent release of radionuclides in the cooling water and eventually to the contamination of the system. This problem has proven to be difficult to solve, therefore uranium targets are not in use at any spallation source, presently.

A remote handling chamber is used to replace a target or a moderator and to perform any required maintenance. In operation, all components become highly radioactive, and the purpose-built chamber is integrated into the target station. It has a pair of manipulators on each side, and operations are viewed through large shielding windows and video cameras. The service area provides water cooling for the target, target pressure vessel, moderators and reflector, plus cryogenic systems for the methane and hydrogen moderators. All these circuits can be remotely monitored.

Additionally, there is an intermediate target which is 1 cm thick graphite sheet and is employed to produce muons. It is oriented at 45° to the beam and is placed ~20 m before the neutron-producing target. Upon collision the proton beam produces pions in the graphite and subsequently pions decay to muons. The proton beam undergoes a scattering angle of ~3 mrad and the graphite target absorbs a thermal power of 1 kW [9].

Figure 3.5. – Unirradiated ISIS TS-1 slab that has been cut in two, showing a hole drilled for a thermocouple. The tantalum cladding on the tungsten (1-2 *mm* thick) is visible.

3.4.2. Moderators

The choice of the moderator determines the spectrum provided by the beam-line. The moderators are placed above and below the target. As shown by Fig. 3.6, they have small dimensions with a volume of about 0.5 liters and are surrounded by a water-cooled beryllium reflector which scatters neutrons back into the moderators and doubles the useful flux of neutrons. The moderators contain a low molecular weight material, the choice of which is aimed to make the neutrons lose energy as fast as possible. Thus a material with high slowing down power and/or high moderation ratio is required. The moderators in use at ISIS are made of liquid H_2O, liquid CH_4, solid CH_4 or liquid H_2. In TS-1 there are four moderators in total:

- Two moderators above the target, 300 K liquid H_2O.

- Two moderators below the target, 110 K liquid CH_4 and 20 K liquid H_2.

In TS-2 there are two moderators with dimensions of 150 x 150 x 30 mm^3 combined with two ambient water pre-moderators:

- One at 40 K, containing solid methane.

- One at 17 K, containing liquid hydrogen.
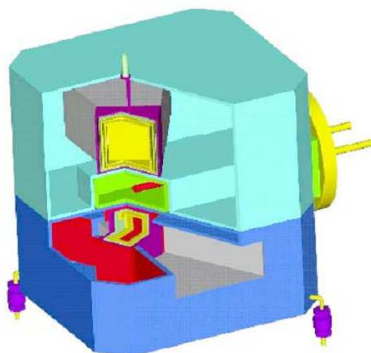
Figure 3.6. – TS-1 Neutron source assembly. Target (green), beryllium reflectors (blue and aquamarine), moderators (violet).

Each moderator provides neutrons with an energy distribution that resembles the Maxwell-Boltzmann distribution, at the temperature of the moderator. Ideally, the neutrons coming from the target pass through the moderator and they reach the thermal equilibrium with the material by collisions with the nuclei. Clearly, the high energies involved and the limited dimensions of the moderators leave a significant part of the neutrons under-moderated, so a high-energy tail (epithermal neutrons) is present in every spectrum collected at spallation neutron sources. As with reactor sources, the neutrons initially produced in the target are very energetic (average energy $\sim$ 2 MeV) and must be moderated to useful energies. A major difference between spallation and reactor sources is that the pulsed source moderators are very small and thermal equilibrium is not fully achieved, as explained above. The small

size of the moderators also means that all neutrons are created within a very short period of time, this period determines the pulse width. Short pulse widths, ~10 μs, are essential for good energy resolution. Moderators run at different temperatures to produce peak neutron flux at different energies. Water moderators (~300 K) produce peak fluxes at about 200 cm^{-1} (25 meV, 1.81 Å), liquid methane (~100 K) at about 70 cm^{-1} (12.5 meV, 2.56 Å) and dihydrogen (~20 K) at about 20 cm^{-1} (2.5 meV, 5.72 Å). The flux distribution, $J(E_i)$, of the ISIS moderators is shown in Fig. 3.7. In the Maxwellian region, the distribution is described by

$$J(E_i) = X_n \left(\frac{E_i}{(k_b T_{eff})^2} \right) exp \left(-\frac{E_i}{k_b T_{eff}} \right) \tag{3.1}$$

Where X_n is the integrated Maxwellian intensity, T_{eff} is the effective moderator temperature and k_b is the Boltzmann constant. The values of T_{eff} for the different moderators are H_2O, 390 K; CH_4, 128 K; H_2, 32 K. These are slightly higher than the measured moderator temperature showing that the neutrons are not fully moderated.
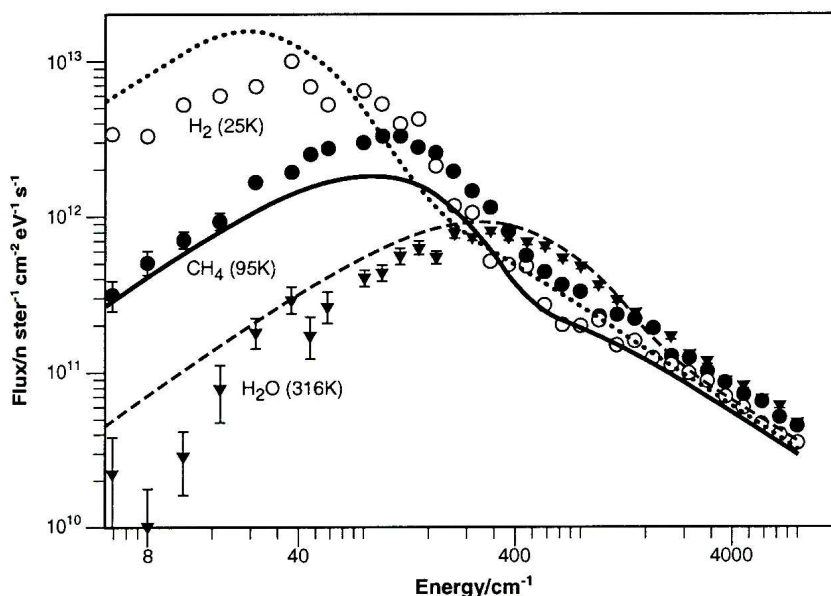
Figure 3.7. – Flux spectrum from the TS-1 moderators in the Maxwellian region [14]. The points are measured data, the lines are from Eq. 3.1.

3.5. Spallation vs reactor source

Research nuclear reactors use thermal neutrons to induce fission in a critical mass of ^{235}U to produce high-energy (fast) neutrons.

$$n +^{235}U \rightarrow 2.5\, n_{fast} + fission\, products + 180\, MeV$$
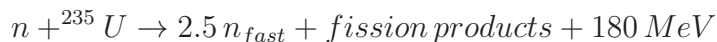
Of the 2.5 neutrons produced per fission event, one is required to maintain the nuclear reaction, 0.5 neutrons are lost to absorption and one is available to leave the core and be used experimentally. The most powerful research reactor is the Istitut Laue Langevin (ILL, Grenoble, France), which has a power of 57 MW. However, 20 MW research reactors are more common. The fast neutrons from fission have energies of 1 MeV and are brought to useful energies (i.e. moderated) by multiple inelastic collisions with the D_2O coolant contained within the relatively large swimming pool. Neutrons achieve approximate thermal equilibrium with the moderator temperature (300 K) with a mean energy of 25 meV. However, the distribution of thermal neutrons is not optimal for many experiments for which higher or lower energies are desirable. In fact, small and specialized moderators can be present within the ambient moderator pool. These moderators operate at different temperatures from the pool and produce their peak neutron fluxes at different neutron energies.

Reactor sources are much more common than spallation sources, there are around 20 reactors that produce core fluxes larger than $10^{14}\, \frac{n}{s\, cm^2}$. Nevertheless, the neutron energy spectra produced by the two types of source is distinctly different as shown in Fig. 3.8. This provides a degree of complementarity: whereas reactors produce large numbers of cold and thermal neutrons, spallation sources produce many more high-energy neutrons. In fact, vibrational spectra obtained over the whole range requires relatively high neutron energies in the epithermal region and spallation sources are leading in this field. However, where a limited energy range is acceptable reactor sources can be very powerful. Another advantage of a spallation source is the heat-load per spallation neutron which is much smaller compared to a reactor. There are also political and environmental reasons, fissile material is not required in spallation sources and less active waste is produced.
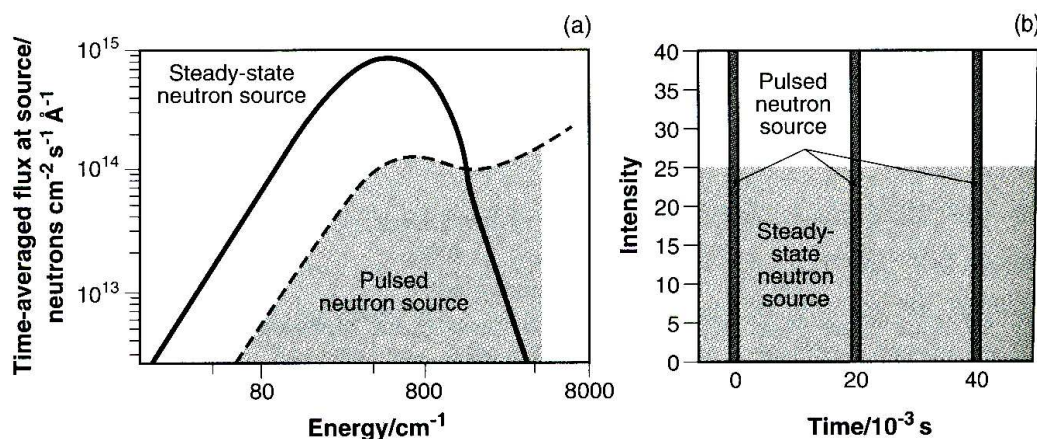
Figure 3.8. – a) Energy spectrum of reactor and spallation neutron sources. b) Time distribution of the neutrons from the two sources. [14]

3.6. ISIS future upgrade

ISIS has been continuously upgraded over the past 30 years in order to allow the facility to face the new challenges in research and to extend its lifetime.

Further upgrades include :

- The completion of the TS-2, in which some instruments are still under construction.

- The full re-design of target and moderator assembly in the TS-1 and upgrade of some instruments.

- The more challenging upgrade of the linac-synchrotron assembly. In fact, STFC is considering to raise the proton beam energy from 800 MeV to the GeV range and the power output from 160 kW to the MW range [31].

4. McStas - Monte Carlo simulations of neutron scattering instruments

4.1. Overview

This chapter contains a brief introduction to the Monte Carlo method and the basics of the neutronics simulation. In addition, we present the main features of the simulation suite McStas and the components used to build the model of the TOSCA instrument at ISIS. The simulations were performed with the help of the computing cluster SCARF, available to users of the Rutherford-Appleton Laboratory.

4.2. Monte Carlo method

Neutron scattering is a low signal technique due to its relatively low flux levels. Hence it is very important to optimize the neutron instrumentation through neutron ray-trace simulations such as McStas. Analytical methods are often used to simulate instruments with a small number of optical elements by the use of phase-space theory. This approach reaches its limit with a high number of optical elements, due to increased coupling between neutron parameters becoming ever stronger as discussed by P. Willendrup [32]. Monte Carlo methods have been recognised as a powerful tool in performing calculations that are normally too complicated for a classical approach and require great amount of effort to compute. The Monte Carlo technique is used in the determination of numerical solutions to problems that cannot be solved analytically, as such it is required in the design and optimization of complex geometrically shaped instruments. McStas works by the principle of probability (Monte Carlo sampling) where, for instance, neutron scattering events are integrated over all neutron trajectories resulting in estimates of measurable quantities. An example of the Monte Carlo method for the determination of an integral is shown below. The integrand function is solved at n random points (avoiding bias) and then the resulting values are summed. It gives a numerical approximation to the integral, Eq. 4.1.

$$\lim_{n \to \infty} \frac{1}{n} \sum_{i=1, a \leq u_i \leq b}^{n} f(u_i) = \int_a^b f(u)du \qquad (4.1)$$

Where u_i is a randomly chosen value according to Monte Carlo sampling in which $f(u)$ is a finite continuous integral function with limits between a and b.

Since 1950s and the appearance of high speed computers, Monte Carlo methods gained an ever increasing amount of attention as they allowed more precise predictions of physical experiments [32]. Presently, neutron scattering instrumentation consists of a series of optical elements that propagate neutrons from a source to a detector. This is where statistical sampling becomes important. Monte Carlo is the set of statistical methods utilized for computational modeling of such cases. It is based on a simple idea of probability sampling of the incoming neutron trajectories. Integrating over all neutron trajectories of a given system results in measurable quantities. The basic principle of Monte Carlo integration is to statistically integrate a given function over some domain D. Monte Carlo integration picks random points over a simple domain D', which contains D. Suppose D is a circle and we desire to evaluate its integral numerically with Monte Carlo. Now suppose D' is a rectangle of dimensions to perfectly fit the circle. Evaluating the integral of the rectangle is simple compared to the circle, it is simply equal to L^2. Now suppose we have a source of neutrons located some distance away from our square. Monte Carlo propagates neutrons by the use of random number generators. In our particular case we are interested in propagating neutrons randomly towards the square, see Fig. 4.1. Thus the total number of neutrons incident on the circle inside our square divided by the number of neutron incident on both the circle and the square gives us the ratio of the two integrals [10]. In the ideal case this ratio is equal to the area $\pi \left(\frac{L}{2}\right)^2$ of the circle divided by the area L^2 of the square. The more neutrons our source propagates, the more accurate the statistics of Monte Carlo integration. For complex neutron instruments it is usually necessary to simulate many millions or billions of neutrons to achieve good statistics at the final detectors.
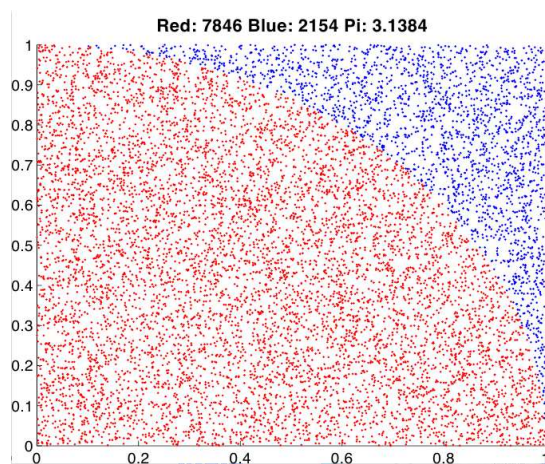
Figure 4.1. – Monte Carlo method to evaluate π using a random numbers generator.

4.3. Introduction to McStas

4.3.1. McStas neutron ray-trace package

McStas is a software package designed to perform Monte Carlo simulations of neutron scattering instruments of high complexity. McStas is available for Windows, Macintosh, and UNIX/Linux systems. MatLab was used in conjunction with McStas to visualize the instrument geometry in a 3D view. McStas is a versatile neutron ray-tracing simulation software that offers the ability to determine accurate estimates of flux, resolution, optimization of parameters and designs where analytical calculations cannot be used. The software package was originally developed in 1997 at Risø, Denmark, and was later adopted by other institutions such as ILL in France and ISIS in the UK. Based on a meta-language specifically designed for neutron scattering, it is translated efficiently into ANSI-C which is then translated into an executable, that performs the simulation. The meta-language allows the building of an instrument from individual components, where a library of standard components, maintained by its user community, is included as part of McStas. Each component is programmed in C++ and serves the purpose of emulating a corresponding physical component, all of which compose a neutron scattering instrument [32]. Well-known examples of this include components such as moderators, guides, choppers, samples, analyzer crystals and detectors. Such components can also be designed by the user with their own specifications and then used in their instrument. An obvious advantage of neutron ray-tracing simulations is the ability to place monitors at any desired location without influencing the beam. Version 2.0 (2012) of the software was used throughout this thesis, see Fig. 4.2.
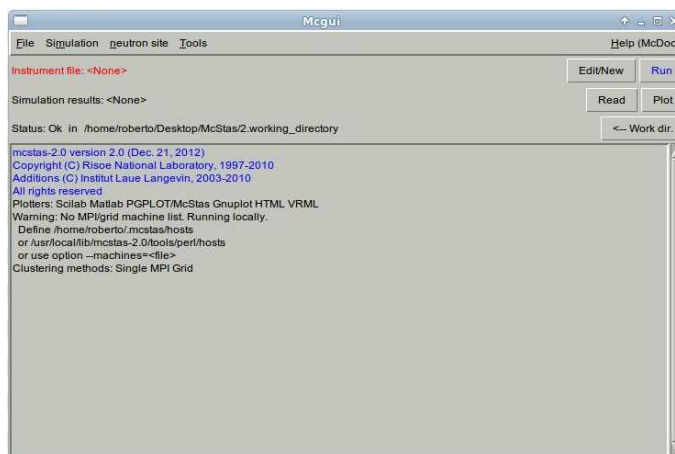
Figure 4.2. – McStas 2.0 main graphic user interface.

4.3.2. The neutron weight and statistical uncertainty

McStas uses the idea of neutron weighting in order to perform fast simulations of complex instruments with large statistics. Neutron rays are assigned with a weight, and these weightings are adjusted according to their path. This means for example, a number of rays entering a component of a certain reflectivity, results in all rays reflecting in the component only that their weighting is adjusted according to this reflectivity. By this method, all rays are kept and lower statistics may be used in Monte Carlo simulations. In a real experiment of such an instrument, only those neutrons that reflect would then be used, meaning that most neutrons up until that point are wasted. The Monte Carlo approach to simulation is that the neutron weight is adjusted to resemble the behavior of real physical properties. The weight representation can be made as follows

$$p_n = p_0 \sum_{j=1}^{n} \pi_j \qquad (4.2)$$

Where p_0 denotes the initial weight, p_n the final weight after traversing through the instrument and π the multiplication factor for the j-th component. The sum of these weights is an estimate of the mean number of neutrons hitting the monitor (or detector) per second in a real experiment [32].

This mean number of neutrons hitting the detector is the intensity I

$$I = \sum_i p_i = N \, \overline{p} \qquad (4.3)$$

Where p_i is the weight of the i-th neutron ray, N the number of neutron rays and $\overline{p}$ the averaged neutron weight. This leads to an approximate statistical uncertainty of

$$\sigma(I)^2 \approx \sum_i p_i^2 \qquad (4.4)$$

Moreover, the central limit theorem provides an estimate for the error in evaluating integrals for large enough statistics by $\frac{1}{N}$.

In McStas, the main detector/monitor parameters are:

- Spectrum: 2D or 3D plot of variables chosen by the user.
- Intensity: average number of neutron rays detected by a monitor per channel.
- I: total integrated neutron intensity.
- Err: error of the integral.
- N: total number of neutrons detected by a monitor.
- X_0: X-value at maximum intensity (peak value).

4.4. McStas components used for TOSCA

4.4.1. Moderator

For TOSCA the neutron beam emerges from a 300 K water moderator, as it will be discussed in more detail in Chapter 5. The spectrum was simulated using a moderator component file created in 2007 by S. Ansell (Neutronics Group, ISIS). The file was generated using MCNP-X and it provides a detailed model of the neutron beam emerging from the moderator of the beamline N8. The model resembles the flux intensity, the wavelength spectrum and the time structure of the real beam. The dimensions of the moderator aperture toward the beamline was set to 0.12 x 0.115 m^2. In the neutron guide simulations the moderator was set to focus the neutrons on a 0.12 x 0.115 m^2 rectangle at 1.625 m from the moderator's aperture. In the diffraction and INS simulations the moderator focus was set directly on the sample area to strongly improve the computational efficiency. A new version of this component file was generated in 2013 by the same group and a comparison between the two versions will be presented in Chapter 6.

4.4.2. Neutron guide

In the foreseen TOSCA upgrade, a neutron guide is intended to replace the current collimator on the N8 beamline. In order to simulate it, the component *guide channeled* was used. This component has been implemented by C. Nielsen in 1999. It models a rectangular guide centered on the Z-axis (direction of the beam) while the entrance lies on the X-Y plane. A neutron guide is characterized by two main aspects: its geometry and the internal coating. While the coating determines the reflectivity as a function of the momentum transfer, the geometry of the guide influences the angle at which a neutron impacts on the guide, and thus the momentum transfer. The guide component can be tapered and this geometry is rather suitable for the N8 beam line, which has a moderator face bigger than the typical sample dimensions of the instruments downstream. This component allows to specify the desired m factor for the internal coating, where m = 0 means completely absorbing wall, m = 1 simulates a standard nickel guide and m > 1 means supermirror coating [2]. The simulated neutron guide has been divided in different sections, also considering some gaps between them according to the engineering group upgrade design. This component does not take into account the effects on the neutron beam due to gravitation.

4.4.3. Disk chopper

This component describes an infinitely thin disk of radius R having a particular frequency of rotation. The disk can have slits of a chosen width and number through

which the neutrons can pass. This device is often used as a velocity selector by trimming the incoming neutron beam and also in stopping frame overlap between successive pulses from the source as already described. A double disk chopper can be constructed by the use of two counter-rotating single chopper components, this kind of chopper produces an output pulse with triangular shaped intensity over time. This phase allows the changing of dynamic range by changing the phase and frequency of the chopper (i.e. tuning the overlap timing of the of the slits). In the TOSCA model a single-disk chopper has been added for completeness at its present position along the beamline. However, its effect was not simulated because the N8 moderator component simulates only one pulse at a time, thus an overlap between successive pulses was not possible and the tail chop was not required.

4.4.4. Monochromators

Analyzer crystals, known in McStas as monochromators, provide an effective and simple way of selecting a monochromatic beam from a white beam. They work on the principle of the Bragg scattering presented in Chapter 2, neutrons in this physical frame are treated like waves. If a neutron is incident on a crystal surface at an angle θ, depending on its λ it undergoes destructive or constructive interference. Thus only specific wavelengths are diffracted from the crystal at the same angle θ. This technique is commonly used on neutron-based instruments to produce monochromatic beams. Different scattering angles and different plane spacings of the crystal select different neutron wavelengths.

The McStas component used for TOSCA is the *monochromator curved* [33], it simulates an infinitely thin mosaic crystal which can be bent specifying a radius of curvature. TOSCA has flat monochromators, consequently the radius of curvature is infinite. Nevertheless, *monochromator curved* was used because it allows a higher grade of customization and gives results as accurate as *monochromator flat* component [21]. The component uses a small-mosaicity approximation and takes into account higher order scattering if enabled. The mosaic of the lattice, defined as angular deviation of crystal lattice planes from a perfectly ordered crystal structure, is anisotropic Gaussian, with different FWHMs in the Y and Z directions. The scattering vector is perpendicular to the surface. Furthermore, *monochromator curved* allows the use of reflectivity and transmission tables of different materials, in the TOSCA model the HOPG reflectivity was used. In fact, the component works in reflection, but also transmits the non-diffracted beam. This latest feature was successfully exploited to simulate the lattice spacing spread $\frac{\Delta d}{d}$ which for research-grade HOPG is below 10^{-3} [15]. Since the $\frac{\Delta d}{d}$ parameter is not implemented natively in this components, it can be simulated following a procedure first tested by K. Pokhilchuk [21], which consist in an overlap of at least three different components set at different d-spacings. However, this method has limitations because the increase in the number of simulated monochromators increases dramatically the computational time.

4.4.5. Beryllium filter

The beryllium filter is installed on TOSCA to filter the higher harmonics coming from the HOPG analyzer, the filter is cooled to enhance the sharpness of the cut-off and to reduce the Debye-Waller factor which damps the neutron scattering. In TOSCA McStas model, this filter was initially simulated by placing in front of each detector a *PowderN* component of appropriate dimensions and set to the beryllium scattering table, the Debye-Waller factor was also adjusted to resemble the measured temperature of the real filter. Although this route has proved to be viable and accurate, a different approach was preferred to reduce the complexity of the simulated instrument. The action of the beryllium filter was simulated by limiting at the first order the diffraction harmonics propagated by the monochromator. This approach allows a more efficient simulation without the loss of physical accuracy.

4.4.6. Monitors

- PSD Monitor: the PSD Monitor is a position-sensitive monitor that detects incident neutron rays in an x-y plane split up into pixel columns (n_y) and rows (n_x). This monitor is not time dependent. It also indicates the total integrated intensity across the surface of the PSD together with the error associated with it.

- Divergence monitors: there are two different divergence monitors used, one monitor is the 1D divergence sensitive monitor which gives beam intensity as a function of horizontal divergence (deg). This allows the detailed analysis of homogeneity at its placement position to be investigated. By rotating such a monitor the vertical divergence can be monitored. The second type is a 2D divergence sensitive monitor in which intensity is measured as a function of both horizontal and vertical divergence in degrees.

- TOF monitor: the TOF monitor is a rectangular monitor that measures intensity as a function of TOF.

- TOF λ monitor: it is a 2D detector of intensity as a function of TOF and wavelength of neutron rays. Thus the wavelength-time distribution is readily extracted at the desired location.

- Wavelength and Energy monitor: These monitors are again rectangular monitors that measure the wavelength and energy of incoming neutrons respectively.

All the detailed technical specifications of these McStas components can be found in the McStas components manual [33].

4.5. SCARF

The computational science is the field of study that deals with developing mathematical models and numerical techniques which reproduce scientific or engineering problems. These models are run on conventional computers or computer clusters to analyze or solve them. Numerical simulations allow the study of complex phenomena that would be too expensive or dangerous to study by experiments. With the advancement of computer technology, scientists can solve large-scale problems that were previously considered not solvable. SCARF is a computer cluster operated by STFC e-Science at the Rutherford-Appleton Laboratory scientific data centre. It operates 2054 processing cores with access to 4.6 terabytes of memory with a overall computational power of 6 teraflop [29]. The SCARF computer cluster is mainly used by STFC researchers in the Central Laser Facility, ISIS neutron source and Computational Science and Engineering Department. Applications include the simulation of plasma physics to establish the correct experimental parameters before running more costly experiments on the Central Laser Facility, and for quantum chemistry ab initio calculations. SCARF is designed to provide a computing resource which can be used by a wide range of researchers. it will soon be available to even more users through the National Grid Service (NGS) which provides computing power to all UK university researchers. Over the years, the increasing data volumes and data rates of scientific experiments have constantly pushed computing and networking technologies to their limits. Whereas, supercomputers and large scientific computing clusters used to employ specialized technology, to bring costs down, the SCARF Cluster uses Intel Xeon processing chips which are also used in commodity computers.

SCARF has been used to perform most of the McStas simulations presented in this thesis. These simulations required a large number of neutrons to reach an accurate statistical model; TOSCA simulations required a statistic of 10^{10} neutrons for the neutron guide and 10^{12} neutrons for the diffraction and INS spectra. This high number of neutrons to be simulated requires high computational power or long processing time many days on a commercial computer. For this reason SCARF has been an indispensable aid in the progression of this project.

5. TOSCA – indirect geometry spectrometer

5.1. Overview

In this chapter we present the main features of TOSCA instrument, a neutron indirect geometry spectrometer located in TS-1 at ISIS spallation neutron source, Oxfordshire, UK. This instrument has unique features that make it one of the most important spectrometer of its kind in the world. Such an apparatus is very complex and consists of several modules that will be described in this chapter. The technical data relating to the instrument were collected from numerous sources throughout the thesis period here at ISIS, although with some difficulty since the original form of the spectrometer dates back to 1985 and it underwent several small and substantial upgrades over the years. Therefore, some technical information summarized in this chapter were disperse between different ISIS groups or the literature available was not updated.

5.2. Introduction to TOSCA

TOSCA is an indirect geometry spectrometer for INS experiments which is optimized for vibrational spectroscopy in the region between 0 and 4000 cm^{-1}; it has been part of the ISIS facility since the beginning of the research on the site, started in 1985 [25]. The first generation of the instrument, called TFXA, measured inelastic back-scattering with both time and energy focusing to achieve high resolution in the energy spectrum of interest [14]. During the period from April 1985 to February 1998, TFXA underwent several small upgrades that reduced the background and improved the resolution slightly. In 1998, it appeared necessary to design a new instrument with greater sensitivity and improved resolution and these goals were subsequently achieved with the design of TOSCA [16]. This project was jointly funded by CNR (Italy) and HFCE (UK). The spectrometer was installed in two distinct phases, the first phase was TOSCA-I which showed a slightly improved resolution compared to TFXA and a greater surface area of detection, which results in a greater count-rate and better quality spectra [4]. The second phase was TOSCA-II (the current TOSCA), installed in 2000 and it is presented in this chapter. This latest form has achieved improvements in resolution, due to the extension of the

primary flight path from 12 m to 17 m, the sensitivity has been also increased thanks to the installation of additional detector banks in forward scattering [6, 14].

In its current form, TOSCA is located along the N8 beamline in the TS-1 at ISIS. The spectrometer is located 17 m away from a room temperature water moderator and the sample is reached by a pulsed beam mainly composed of thermal and epithermal neutrons. The neutrons scattered from the sample are Bragg reflected by a pyrolytic graphite crystal which acts as a low-pass filter for the wavelengths. Neutrons reflected at a Bragg order higher than the first are removed by a beryllium-cadmium filter kept at cryogenic temperature, in fact it acts as a high-pass filter for the wavelengths. This filter configuration is intended to fix the final energy at 32 cm^{-1} ($\backsim$ 4 meV). This represents the working principle of an indirect geometry spectrometer, in this way there is a direct relationship between the energy transfer (E_T, cm^{-1}) and momentum transfer (Q, Å^{-1}) that occurs between the neutrons and the sample material, indeed TOSCA has $E_T \approx 16Q^2$. The INS assembly on TOSCA is composed of ten banks, while each bank has 13 ^3He tubes. Five banks are placed in the forward-scattering position (i.e. at a scattering angle of $\backsim$ 47.5°) and five in back-scattering (i.e. $\backsim$ 132.5°) [6]. As already mentioned in Chapter 4, a single disk chopper is placed along the N8 beamline to cut the slow neutrons tail of the first three pulses (out of four), in order to avoid overlap between subsequent pulses. The fourth pulse is followed by a void pulse hence is not chopped, this allows the exploitation of the slow neutrons tail for the study of the elastic line ($E_N \approx 4\,meV$, $E_T = 0$). The whole design of TOSCA was intended to achieve an unprecedented INS resolution ($\sim 1.25\% \cdot E_T$), see Fig. 5.1. This result was successfully achieved thanks to the combination of several factors:

- Small time-width of the neutron pulse emerging from the target ($\sim 400\,ns$).

- Good moderation performance of the water moderator in terms of time required to emit neutrons of a certain wavelength ($\sim 12\,\mu s/$Å).

- Longer primary flight path which allowed reduction of the statistical errors in the TOF.

- Small bandwidth of the HOPG analyzer + Be-Cd filter assembly.

- Geometry of the detectors optimized to operate in time and energy focusing [6].

5.3. Moderator

TOSCA receives a polychromatic beam *via* a water moderator kept at 300 K and poisoned by a thin gadolinium foil at a depth of 20 mm [6]. The water is contained in an aluminium box, placed above the tungsten target and embedded in the berillyum reflector assembly; the moderator face is 120 mm wide and 115 mm high [11]. This assembly sends mainly thermal and epithermal neutrons to the sample position with
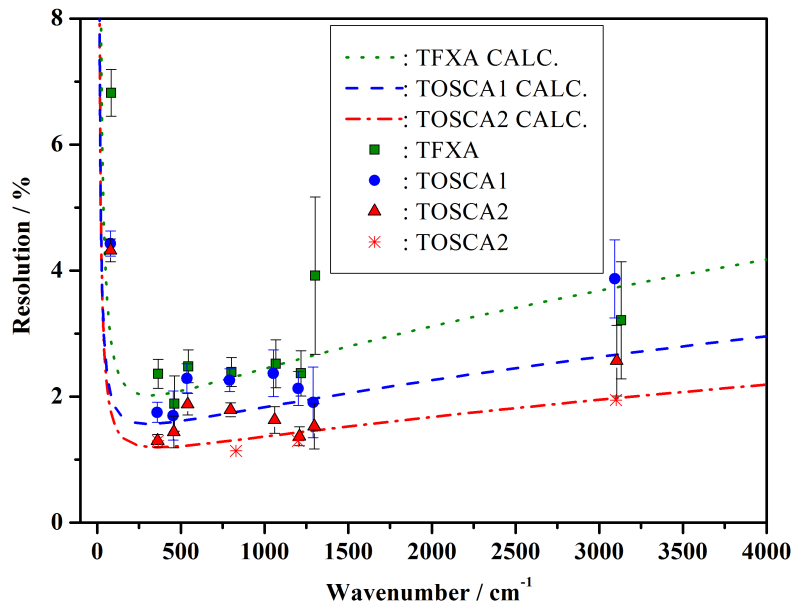
Figure 5.1. – Resolution spectra of TFXA, TOSCA-I and TOSCA-II. The lines represent the analytical calculations. Taken from [14].

a good time performance, its moderator term is $\sim 12\,\mu s/\text{Å}$ inferred during previous calibrations of the instrument [23]. The energy range of the incident beam is broad, from 2.5 meV to 1000 meV, thus TOSCA is able to study a wide range of vibrational transitions in materials. A comparison between the McStas N8 moderator model and the measured TOSCA incident beam is presented in Chapter 6.

However, it is worth noting that most of the incident neutrons have energy below 100 meV, while energies up until 200 meV are equally useful for the INS technique. Thus, the proposed installation of a neutron guide along the N8 beamline has the aim of increasing as much as possible the flux in the range between 10 meV and 200 meV, in order to extend the analytical capabilities of TOSCA.

5.4. Beam monitor

Tosca is equipped with a beam monitor (detector No. 141) placed upstream from the sample, at 15.794 m from the moderator, which analyzes the TOF spectra of the neutron flux and allows the normalization of the experimental data. The detector is composed of lithium dots embedded in scintillating glass. The detector has approximate dimensions of 5 mm width, 50 mm height and 0.13 mm thickness. The neutron detection takes place through products of nuclear reactions triggered by neutrons colliding with the lithium nuclei, as a result the charged particles emitted by the reactions cause the scintillation of the glass matrix. The bunch of photons is measured by a PMT optically coupled to the glass; the PMT then transmits an analog signal which triggers a TOF counter. Clearly, the aim of this detector is to

provide a measure of the incident spectrum without a significant attenuation of the beam, which is transmitted to the sample. For this reason, the detector No. 141 is designed with a low detection efficiency and lithium is organized into small dots of Li_2O uniformly dispersed within the glass, in order not to cause flux inhomogeneity on the sample.

The main physical specifications of the detector are:

- Ratio of scintillating material to total area: $R = 5.391011\ 10^{-5}$.

- Wavelength dependent attenuation coefficient: $A = 0.83\ mm^{-1}\text{Å}^{-1}$.

- Thickness: $L = 0.13\ mm$.

These parameters allow to calculate the calibration curve as a function of wavelength, which extrapolates from the detector data the actual wavelength spectrum incident on the sample. The number of neutrons detected N_{det}^{λ} at a certain wavelength is given by

$$N_{det}^{\lambda} = N_{tot}^{\lambda} E(\lambda) \tag{5.1}$$

Where N_{tot}^{λ} is the actual number of neutrons at wavelength λ that crossed the detector and $E(\lambda)$ is the detector efficiency function, Eq. 5.2, shown in Fig. 5.2.

$$E(\lambda) = R\left(1 - e^{-AL\lambda}\right) \tag{5.2}$$

Where R, A, L are the detector parameters mentioned earlier. Consequently, the actual number of neutrons with wavelength λ that reach the sample is given by

$$N_{tot}^{\lambda} = N_{det}^{\lambda}\left(\frac{1}{E(\lambda)}\right) \tag{5.3}$$

It is worth noting that the detector No. 141 measures the incident flux as a function of the arrival time (TOF), the wavelengths (Å) of the neutrons are directly obtained from the measured TOF and detector distance from the moderator.

5.5. Beamline structure

Neutrons emitted from the spallation target or reactor core pass through a moderator and subsequently are lead to the sample along beam-tubes. The beam tubes are arranged as close to the moderator as possible, to maximize the intercepted flux. These are usually arranged tangentially in order to avoid a direct view of the source's primary radiation (fast neutrons and gamma rays). The primary radiation dominates the safety requirements of the instruments (and thus the cost) and also contributes much to the instrumental background. Neutrons are neutral and it is
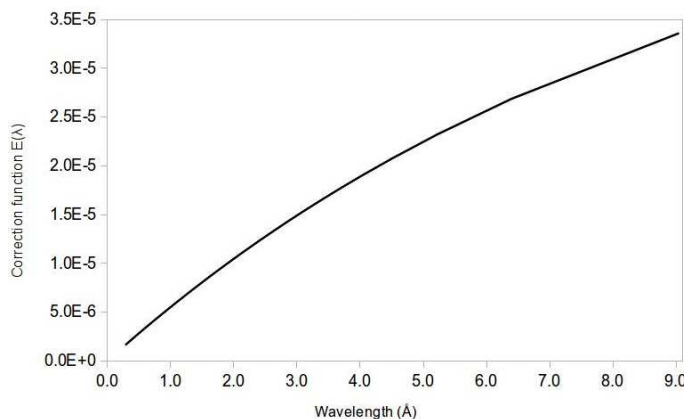
Figure 5.2. – Efficiency curve $E(\lambda)$ of the TOSCA beam monitor as a function of wavelength.

hard to influence their trajectories, in fact most of the neutrons hit the monochromators, or samples held in the main beam because their flight path naturally intersect those objects. The flux at an object in a naturally collimated neutron beam is proportional to the solid angle it subtends at the source. Thus for the moderator to sample distance d_i, the flux varies as $\frac{1}{d_i^2}$ and the incident flight-path must be kept short, from 10 to 20 m [14]. The natural collimation of a neutron beam is achieved, as in pin-hole optics, by a series of diaphragms. Each diaphragm is made of a neutron absorbing material and defines the beam size at that point, B_4C rings are in use along TOSCA beamline. An effective collimator maximizes the sharpness of the beam edge, thus minimizing the beam penumbra. There is no element of energy selection in a simple beam-tube and the exit beam energy distribution is said to be white. On TOSCA, beamtubes are evacuated to avoid the 0.2% beam attenuation by air scattering [14]. On spallation sources the evacuation is often applied to all instrumental flight-path but on reactors the secondary flight-paths of many instruments are in the air, helium (low absorption, some scattering), or argon (low scattering, some absorption) [14].

In summary, TOSCA beamline is 17 m from the moderator to the sample and it is composed of 1 shutter tube, 1 monolith tube and 5 secondary collimation tubes, see Fig. 5.3. Every section contains various collimation inserts. The entire flight path is buried into a shielding house made of concrete and steel. The beamline is sectioned in different parts separated by thin aluminium windows to keep the vacuum. According to the engineering drawings, the cross section of the beamtubes is tapered from the moderator to the sample, it starts with a section of $84\,x\,80\;mm^2$ and ends with a section of $43\,x\,43\;mm^2$, see Tab. 5.1. Detailed drawings TOSCA components and assembly can be found at this link http://isis2.sci.rl.ac.uk/hpgl/SI2541/index.htm.

Item of Equipment	Existing Instrument
Moderator Type H_2O 300K (above target)	Viewable face 100 x 100 mm^2. Umbra size 85 x 85 mm^2. Moderator vessel: 3 mm thick Aluminium.
Void Vessel Windows (#1, #2)	2 x 0.5 mm thick Aluminium.
Collimation Ray Layout	Ref. SI-2541-309.
Window #3	1 x window 0.5 mm thick.
Shutter Collimation	B_4C collimation. Ref. 0R2541-046. Input (mm): 1'605 from mod., 84.5~84.0 W x 80.6~80.0 H. Exit (mm): 3'565 from mod., 73.5~73.0 W x 74.5~74.0 H.
Window #4	1 x window 0.5 mm thick.
Insert Collimation Assembly	B_4C collimation. Ref. SI-2541-400. Input: 3'695 mm from mod., 75.1 x 74.1 mm^2. Exit: 5'977 mm from mod., 69x69 mm^2. End of tube: 6'040 mm from mod.
Window #4	1 x window 0.5 mm thick.
Secondary collimation Tube 1	B_4C collimation. Ref. OR-2541-067. Input: 6'098 mm from mod., 68.4 x 68.4 mm^2. Exit: 8'530 mm from mod.
Secondary collimation Tube 2	B_4C collimation. Ref. SI-2541-439. Input: 8'530 mm from mod. Exit: 8'995 mm from mod., 61.1 x 61.1 mm^2.
Gate Valve	VAT Valve DN100 Series 08.
Gate Valve Window #6	0.5 mm thick Aluminium. Ref. SI-2541-398.
Chopper Window #7	0.5 mm thick Aluminium Alloy.
T-Zero Chopper (Ref. 0-SI-2700-001)	Modified Internally with 4 bladed 15 mm thick cadmium disc. Designed for 60 x 60 mm^2 beam. Centre: 9'479 mm from mod.
Chopper Window #8	0.5 mm thick Aluminium alloy.
Window #9	0.5 mm thick Aluminium. Ref. SI-2541-440.
Secondary collimation Tube 3	1'720 mm long. Ref. SI-2541-438. Input: 9'879 mm from mod., 58.7 x 58.7 mm^2. Exit: 11'599 mm from mod.
Secondary collimation Tube 4	1'720 mm long. Ref. SI-2541-438. Input: 11'604 mm from mod. Exit: 13'324 mm from mod.
Secondary collimation Tube 5	2'432 mm long. Ref. OR-2541-067. Input: 13'329 mm from mod. Exit: 15'761 mm from mod., 43.4 x 43.4 mm^2.
Window #10	0.5 mm thick Aluminium. Ref. 3-SI-2541-440.
Monitor	Beam monitor (Detector #141). 15'794 mm from mod.
TFXA Detector Box Assembly	Ref. SI-2541-134.
Window #11	0.24 mm thick Aluminium. Ref. SI-2541-171.
Vacuum Vessel (Tube)	385 mm long. Ref. SI-2541-170.
Bellows Assembly	80 mm long, nominal. Ref. SI-2541-173.
Vacuum Vessel (Tube)	325 mm long. Ref. SI-2541-174.
Sample Position (Ref. SI-2541-490)	17'000 mm from mod. Size 40 x 40 mm^2.

Table 5.1. – Detailed description of the existing components along TOSCA beamline. Courtesy of ISIS Engineering Group.
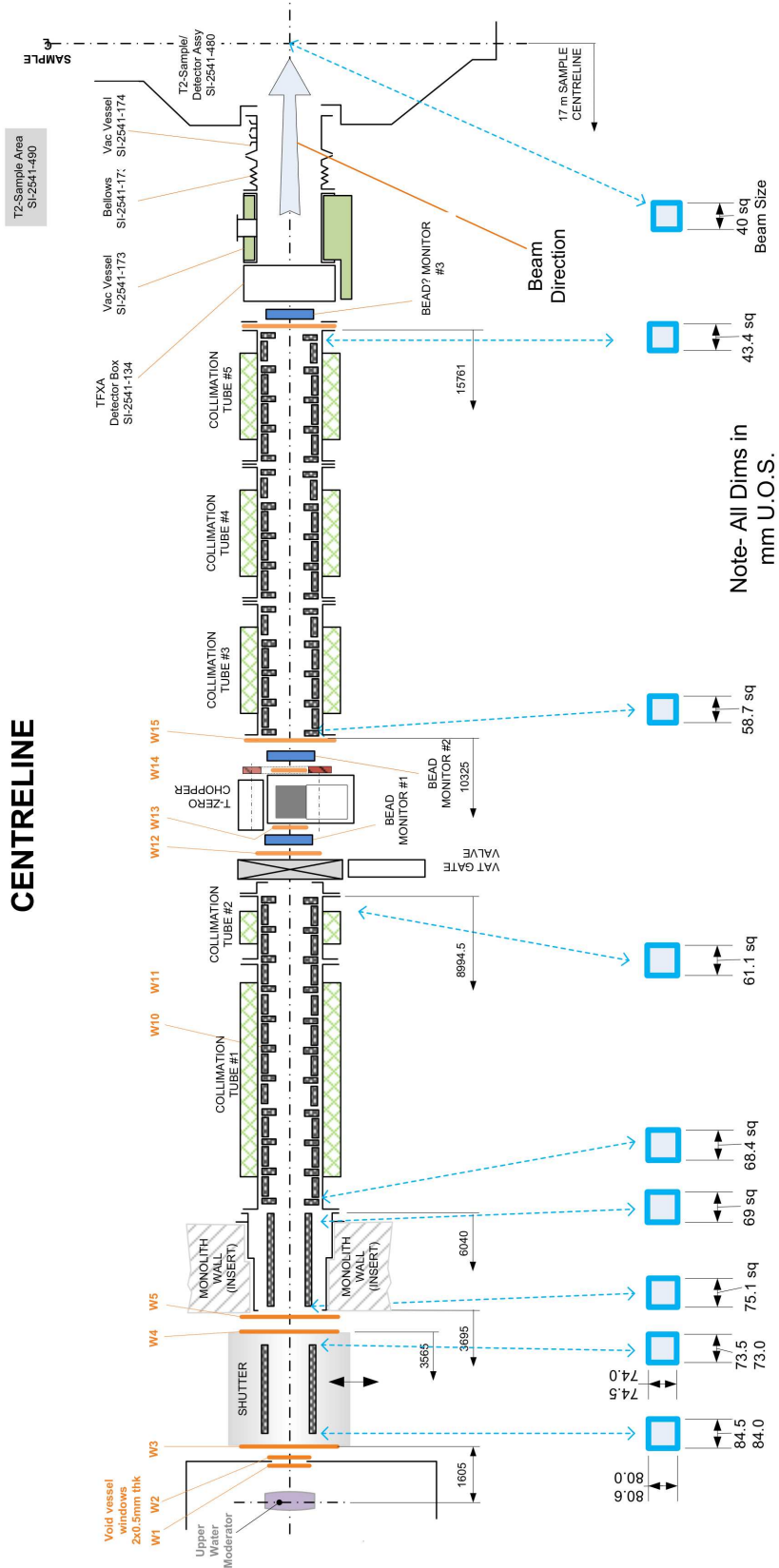
Figure 5.3. – Schematic view of TOSCA existing beamline. Courtesy of ISIS Engineering Group.

5.6. Chopper

The installation of TOSCA at 17 m greatly improved the spectral resolution but it restricted the energy transfer range to $> 25\,cm^{-1}$. This was because the elastic line occurs at ~23000 μs and since ISIS operates at 50 Hz, a neutron pulse occurs every 20000 μs (a frame), thus fast neutrons would overtake slow neutrons from the preceding pulse. This is problematic for TOF analysis since this method depends upon the time a neutron takes to go from the moderator to the sample, thus the overlap of different pulses makes the measure unreliable. In the original design of TOSCA the overlap was prevented by the Nimonic chopper with a sheet of neutron absorbing material on the blade. It was used for suppression of the unmoderated neutrons and γ-rays produced by the proton beam impacting the target, in fact there was a concern that this radiation would cause increased background. In 2008, ISIS began operating the second target station (TS-2), which takes one pulse in five from the accelerator, the resulting TS-1 input is constituted from four 20000 s frames followed by a 40000 μs frame, Fig. 5.4a. Thus TS-2 operation enables access to energy transfers below 25 cm^{-1} on TOSCA, including the elastic line, as shown in Fig. 5.4b. Moreover, the concerns about the background generated by prompt pulse proved to be unfounded, hence the Nimonic chopper was replaced by a custom designed disc chopper Fig. 5.5, to block the slow neutrons for four pulses and allow them to pass during the fifth (TS-2) pulse. As a result of this upgrade, the energy transfer range now extends down to -25 cm^{-1} and includes the elastic line. This extension of the spectral range is useful as it provides, for instance, a direct measure of the quantity of ortho-hydrogen present in a sample when di-hydrogen is being studied and potentially allows TOSCA to be used for quasi-elastic neutron scattering studies of very fast processes [17]. The current chopper then avoids the overlap of subsequent pulse and it extends the TOSCA inelastic capability, in fact the absence of the TS-2 pulse allows to leave the fourth pulse unchopped and thus to exploit lower incident energies.

Defining τ_{min} and τ_{max} the minimum and maximum flight time from moderator to detector selected by the chopper, the necessary condition to avoid overlap between subsequent pulses is $\tau_{max} - \tau_{min} \leq \tau$. Thus, the widest wavelength range accepted is given by Eq. 5.4.

$$\Delta\lambda \leq \tau\left(\frac{h}{m_n L}\right) \tag{5.4}$$

Where τ is the duration of a frame, h is the Planck constant, m_n is the neutron mass and L is the distance between the moderator and the sample.

The chopper mid-line is located at 9479 mm from the moderator and consists of 4 blades (plus one that is missing) that interrupt the beam by cutting the tails of the first 3 pulses while the fourth and last pulse is not chopped due to the missing blade. Each blade is composed of an aluminum casing that encloses a 15 mm thick sheet

of cadmium, this material has a high absorption cross section for neutrons having energy $< 0.5\,eV$ ($\sigma_{abs} = 10^4 - 10^6\,barns$), it is very effective in absorbing neutrons that constitute the pulse tail while it is almost transparent to fast neutrons. The chopper phase can be fine tuned depending on the experimental requirements, so one can select the energy range of the chopped pulses.

The McStas moderator model has been implemented to simulate a single pulse from the source, for this reason the addition of the chopper in the simulated TOSCA instrument is useless for practical purposes and just adds complexity to the calculations. Despite this, the chopper was added in the full version of the instrument model to evaluate how the pulse changes and how one can select the energy range by varying the phase arbitrarily. However, the chopper was removed in the calculations of diffraction spectra and INS spectra in order to speed up the simulations and to consider the entire range capability of TOSCA.

Distance from moderator	9479 mm
Rotational frequency	10 Hz
Radius	298 mm
Number of blades	4
Cadmium blade thickness	15 mm
Blade width	24° (6'666 μs)
Normal gaps width	48° (13'333 μs)
Large gap width	120° (33'333 μs)
Time jitter at 10 Hz	±9 μs

Table 5.2. – Technical specifications of the TOSCA chopper.
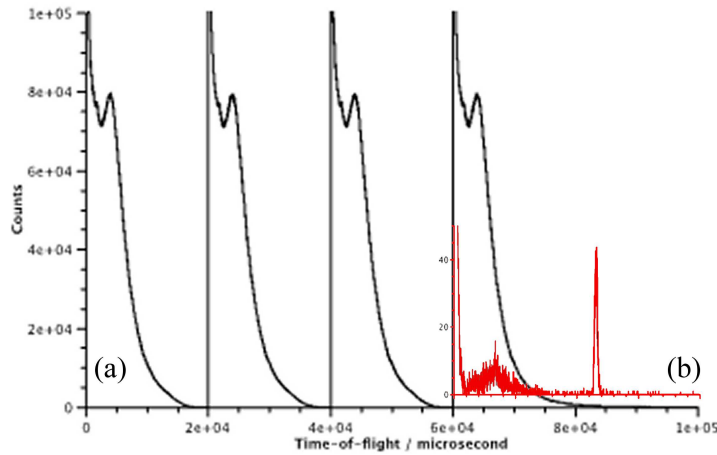
Figure 5.4. – (a) Incident monitor spectra (black trace) when TS-2 is operating showing the long 40'000 μs frame, (b) time-of-flight spectrum (red trace) in an inelastic detector, showing the elastic line at ~23'000 μs [17].
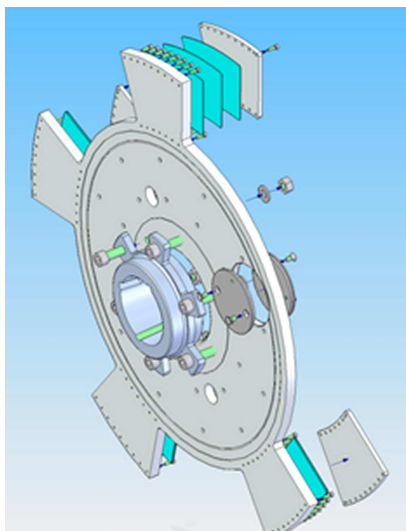
Figure 5.5. – Schematic of the custom disc chopper that enables the long (TS-2) frame to be exploited, in order to extend the energy transfer range of TOSCA [17].

5.7. Diffractometers

TOSCA has modest high-resolution diffraction capabilities since its installation, composed of four squashed ^3He tubes where each tube is ~ 10 mm wide, see Fig. 5.6. They are positioned in back-scattering geometry over the angular range $\pm$ 177-179° relative to the incoming beam, at the same height on the sample. The secondary flight path related to these detectors is 1.210 m. It is worth noting that this diffraction assembly on TOSCA is capable of providing a good coverage of the d-space, from 0.2 to 20 Å [16].
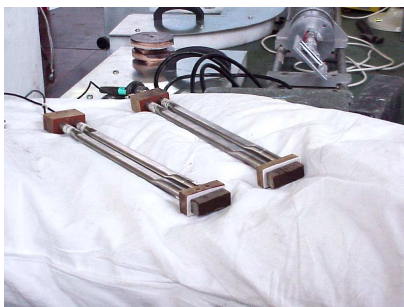
Figure 5.6. – Tosca ^3He tubes used for diffraction studies. Courtesy of ISIS Engineering Group.

Currently this capability is not used extensively because the detection area is small and this results in a very low count rates. Furthermore coherent scattering is typically swamped by incoherent backgrounds in hydrogenous systems. However, the interest in non-hydrogenous materials is currently increasing and the higher incident flux due to the proposed neutron guide would extend the use of diffraction

measurements on TOSCA. This upgrade will eventually prepare the instrument for much needed simultaneous structural and spectroscopic studies of complex materials under realistic conditions.

5.8. INS spectrometer assembly

TOSCA is an indirect geometry spectrometer used mainly for studies of the vibrational modes in materials *via* inelastic neutron scattering. The beam size at the sample position is 40 x 40 cm^2 and the neutrons scattered by the sample are eventually Bragg reflected by a pyrolytic graphite analyzer towards a beryllium filter which transmits certain wavelengths to the ^3He tubes bank. The whole instrument is buried in shielding composed of borated plastic, B_4C, steel and cadmium plates [6]. A closed cycle refrigerator is embedded in the spectrometer to regulate the temperature inside the cryostat, this allows measurements in the range between 10 K and room temperature [18]. The sample position marks the end of the primary flight path, 17.000 m away from the moderator, and the beginning of the secondary flight path toward the analyzers.
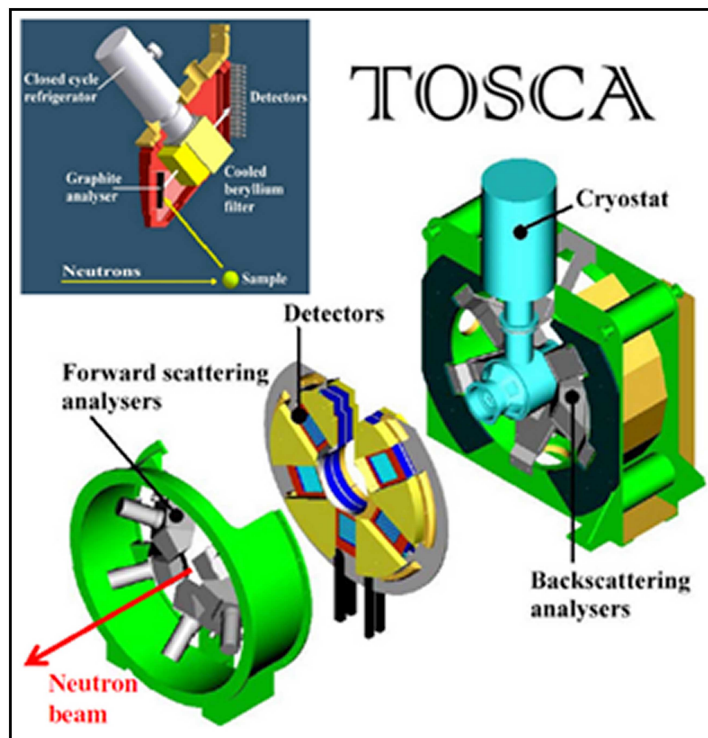
Figure 5.7. – Scheme of TOSCA spectrometer. The inset shows the analyzer and beryllium filter assembly, as well as the detector tubes. Courtesy of P.C.H. Mitchell *et al.* [14].

5.8.1. HOPG monochromators

Crystal monochromators (analyzers) provide an easy way of selecting monochromatic neutrons from a white beam. Considering the Bragg law, when a white neutron beam is incident up on the planes of a single crystal at a glancing angle, depending on the plane spacing, a set of wavelength will be diffracted from the crystal at the same angle. This assembly acts as a low pass filter for the wavelengths, the Bragg scattered neutrons have wavelength λ and its subsequent harmonics ($\lambda/2$, $\lambda/3$...). This energy selection technique is commonly used in optical and neutron instruments. TOSCA monochromators are kept at room temperature and placed in forward-scattering (glancing angle $\simeq 47.50°$) and back-scattering (glancing angle $\simeq 132.30°$) from the sample center, see inset in Fig. 5.7. There are 5 monochromators in the back-scattering position and other 5 in the forward-scattering position. They are placed in the vertical plane at 60°, 120°, 180°, 240° and 300° around the beam axis, see Fig. 5.7. The analyzers in use are slabs of pyrolytic graphite 2 mm thick which reflect on the 002 crystallographic plane, this plane corresponds to a d-spacing of 0.3354 nm with a mosaic spread of 2.5° [6]. Typical values for the d-spacing spread of the more ordered grade HOPG range between 0.03% and 0.07% [15]. In the simulations the d-spacing spread of the analyzers was assumed to be $\pm 0.03\%$, the mosaic spread of the crystal was equally taken into account. The dimensions of the monochromators are approximately 150 x 100 mm^2, see Fig. 5.8. The neutrons reflected at the aforementioned glancing angles are selected in energy, the first harmonic ranges between 3.5 and 4.1 meV ($\sim 30\,cm^{-1}$, $\sim 4.5\,\text{Å}$) and this interval defines the elastic line [6]. The undesirable higher harmonics (ca. 16, 36, ... meV) reflected by the analyzer are finally suppressed by the Be-Cd filter.

Figure 5.8. – Photo of the TOSCA HOPG crystal monochromators. Courtesy of ISIS Engineering Group.

5.8.2. Beryllium-cadmium filter

The beryllium-cadmium (Be-Cd) filter is a high-pass filter for the neutron wavelengths. Together with the HOPG analyzer, it constitutes a band-pass filter which fixes the energy at 3.5-4.1 meV by allowing only the first harmonic from the analyzer to reach the detectors. The Be-Cd filter is 120 mm thick, cooled to below 35 K by helium refrigerators to enhance the sharpness of the beryllium scattering cut-off [18]. Beryllium is transparent to neutrons that have energy below $\sim 40\,cm^{-1}$ while it is a strong neutron scatterer at higher energies. The beryllium cut-off is very discriminating, especially if cooled below 100 K. In fact at 100 K, a 15 cm thick filter has a transmission factor of 0.75 below the cut-off and 10^{-4} above the cut-off [14]. The beryllium filter is divided in 4 blocks along the direction of flight, the blocks are 3 cm wide and separated by 1 mm thick sheets of cadmium, see Fig. 5.9a. The beryllium scatters and thus remove the undesired neutrons from the flight path, while cadmium acts as an absorbing wall for the scattered neutrons. The presence of cadmium sheets helps to further reduce the instrumental background by a factor of 10 [17]. This material is an excellent neutron absorber up to epithermal energies. In Fig. 5.9b the performance of this filter is presented and compared to the previous solutions adopted for the instrument.
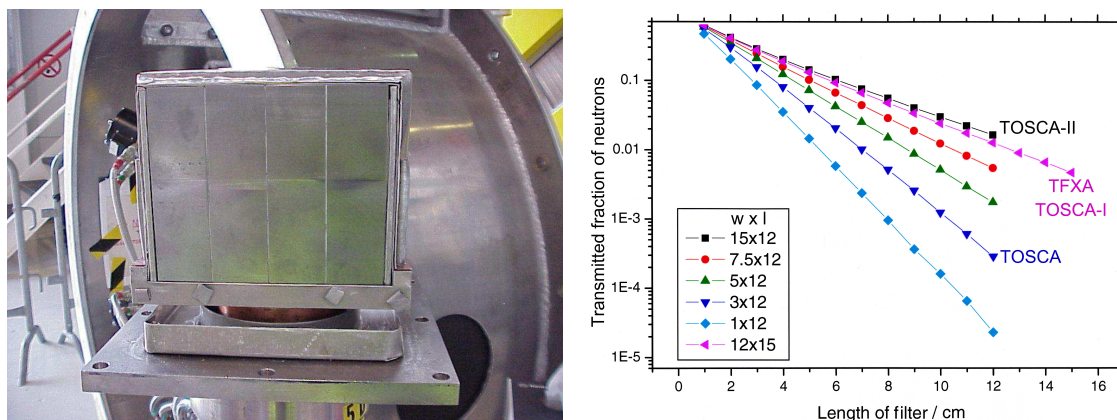
Figure 5.9. – a) TOSCA beryllium filter dismantled, b) Transmission of higher-order neutrons through the beryllium filter as a function of the width (w) and length (l) of the filter, in centimeters. The filter sizes used for TFXA, TOSCA-I and the initial (TOSCA-II) and final implementation (TOSCA) are indicated.

5.8.3. Detector banks

As explained in [6], the TOSCA inelastic spectrometer is sited 17 m from the water moderator and is composed of ten detector banks lying on the sample plane: five for back-scattered neutrons and five for forward-scattered neutrons, see Fig. 5.7. Each bank contains 13 ^3He squashed tubes with a thickness of 10 x 250 x 2.5 mm^3, the same as in TOSCA-I, but thinner compared to TFXA. High ^3He pressure is

used to compensate further the small thickness of the squashed tubes; the tubes are charged at 20 bar and kept at room temperature. These tubes are intended to detect neutrons in a relatively low and limited energy range, from 3.5 to 4.1 meV as explained earlier, due to this fact the detection efficiency is kept high and constant. The detector array is the last step of the secondary flight path, which has a total length that ranges between 550 and 770 mm, depending on the neutron flight path. The measurement of the incident neutron energy is made evaluating the total Time-of-Flight t through the kinematic relation $t = \frac{L_0}{v_0} + \frac{L_1}{v_1}$. Where L_0 and L_1 are respectively the primary and the secondary flight path, while v_0 and v_1 are respectively the incident and the scattered neutron velocity, where v_1 is fixed by the analyzer-filter assembly. As aforementioned, in TOSCA the typical values of the neutron flight paths are $L_0 = 17$ m and $L_1 = 0.55$–0.77 m. Over the time some changes were made along the beamline from TOSCA-I to the actual TOSCA in order to enhance the sensitivity and to reduce the instrumental background. Since the uncertainty of L_1 dominates the instrument energy resolution [34], a two-dimensional focusing of t was arranged for the detectors, in order to compensate for the errors in L_1 with the opposite errors in v_1 [34]. This configuration has been obtained in TOSCA by arranging the detector banks in a circular geometry around the beam axis and aligning the sample and each detector tube in two parallel planes, again parallel to the plane of the respective analyser, see Fig. 5.7. In addition, to further improve the energy resolution, the Marx principle [19] was also applied by positioning the ^3He tubes perpendicular to the scattering plane.
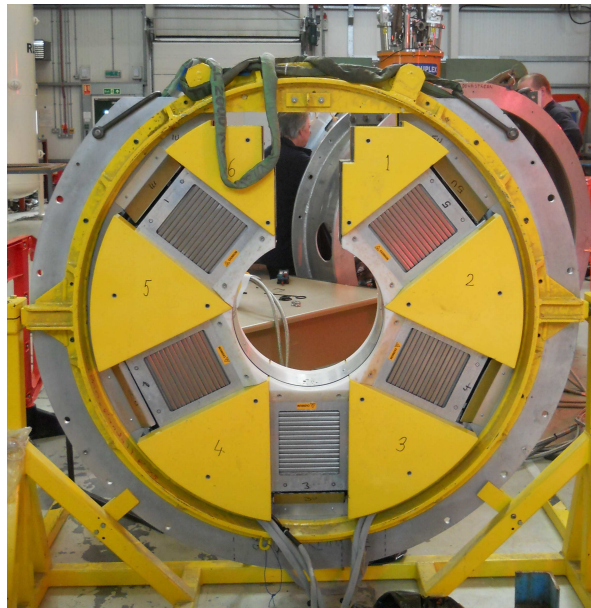
Figure 5.10. – Photo of the TOSCA ^3He detectors and shielding assembly. The cryostat which contains the sample is located at the center of the structure.

6. Benchmarking of TOSCA moderator

6.1. Overview

The current aim of the McStas model of TOSCA, entirely developed during the period of writing this thesis, is to calculate what is the effect of installing a neutron guide on TOSCA. Before accomplishing this task, it is of great importance to validate the McStas moderator model we are going to use. The validation, known as *benchmarking*, concerns different aspects of the physics of the moderator, such as the energy spectrum and the time performance in moderating neutrons of different wavelength. Clearly, the benchmarking is performed comparing the calculations and the experimental data about the moderator currently installed on TOSCA, these data were measured by means of the TOSCA beam monitor.

6.2. McStas models of the moderator

As explained in Chapter 5, the moderator used for both TOSCA and INES is a water moderator kept at 300 K and poisoned at a depth of 20 mm with a thin gadolinium foil, it produces a peak flux at *ca.* 30 *meV* (240 cm^{-1}) [14]. The aperture of the moderator is 115 *mm* high and 120 *mm* wide and it is enclosed inside the monolith. At 1.625 *m* from the moderator the shutter has its aperture, which is 84 *mm* wide and 80 *mm* high. The simulations of TOSCA, performed with McStas, rely on a moderator model that was developed in 2007 by the ISIS Neutronics Group using the Monte-Carlo N-Particle Transport code, MCNP-X. That model was considered quite accurate compared with the experimental results and was not modified until 2013. Nevertheless, as part of the improvement of TS-1 the ISIS Neutronics Group is reassessing the McStas model for every moderator in the station in order to enhance its accuracy. The first new set of models was released in March 2013 and was based on the previous models of TS-1. TOSCA McStas new moderator file contained a number of improvements about the geometry and the spectrum. Furthermore, it was announced that new models with major modifications are forthcoming. In order to assess the two models, the outputs generated for the actual TOSCA instrument were compared by using the two different moderator files. In particular the energy, wavelength and TOF spectra were compared, as well as the spacial beam profile

and the divergence of the beam. The simulations were performed at 1 μm, 1.625 m (shutter aperture) and 17 m (sample position) from the moderator's face. The neutron flux analyzed by the monitor was lower as its position moved further from the moderator. For this reason less neutrons were simulated for calculations closer to the moderator, in order to save computational time while keeping the statistics accurate enough.

6.2.1. Spectrum analysis at the focus position

The energy and wavelength spectra from the 2007 and 2013 moderator models were collected at the focus position (1.625 m from the moderator) and 10^9 neutrons were simulated for each run, see Fig. 6.1 and Fig. 6.2 respectively. The peak energy is at around 30 meV for both models and the differences between the spectra are visible only below 60 meV. For every energy step, the difference of intensity between the two curves lies below 8%. There are no relevant differences in the overall shape of the curves. The data were normalized in order to reduce the spectrum areas to unity.

Figure 6.1. – Energy spectra at the focus position, linear x-scale (left) and logarithmic x-scale (right).
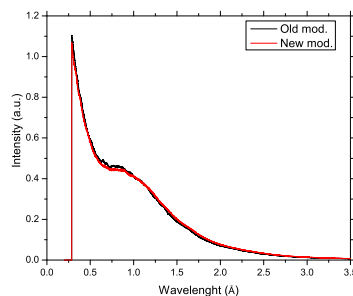
Figure 6.2. – Wavelength spectra at the focus position.

6.2.2. Spectrum analysis at the sample position

Here we present the simulations of the 2007 and the 2013 moderator file where energy and TOF spectra were collected at the sample position (17 m from the moderator) and 10^9 neutrons were simulated for each run, see Fig. 6.3 and Fig. 6.4 respectively. At the sample position it is useful to consider the TOF spectrum of the neutrons, since it establishes the TOF fingerprint of the moderator at the end of the primary flight path and it has a particular relevance because TOSCA is a TOF spectrometer. One can notice that the TOF spectrum in Fig. 6.4 is similar to the wavelength spectrum in Fig. 6.2, this is due to the linear dependence between TOF and wavelength. Furthermore, the current TOSCA collimation beamline does not alter the beam spectrum along the path, like the neutron guide does, as explained in Chapter 7. The data were normalized in order to reduce the spectrum area to unity.
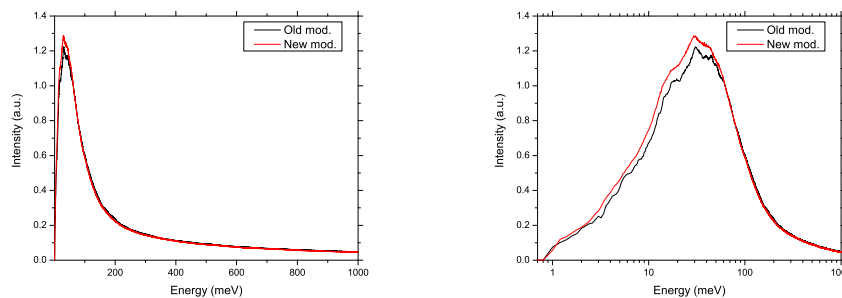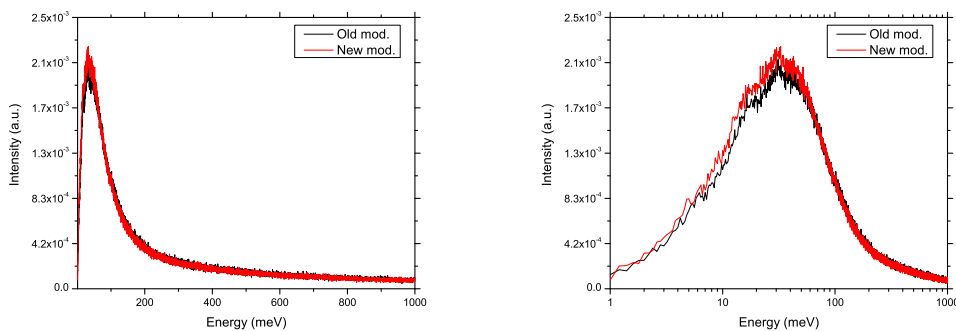

Figure 6.3. – Energy spectra at the sample position, linear x-scale (left) and logarithmic x-scale (right).
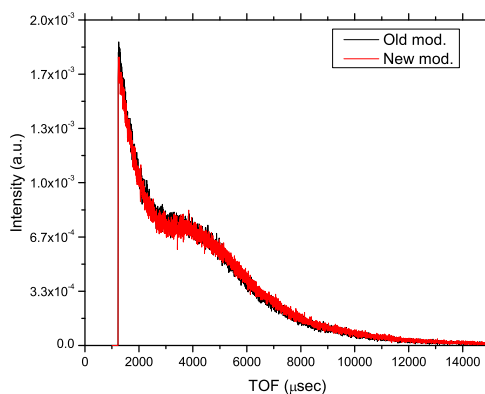
Figure 6.4. – TOF spectra at the sample position.

51

6.2.3. Beam shape

The following data concern the spacial beam profile in the XY plane at the sample position; the profile consider all the incident without discrimination in energy. There are no noticeable differences in the beam shape between the two moderator models, see Fig. 6.5.

PSD monitor specifics: X-range [-7.5, 7.5] cm, Y-range [-7.5, 7.5] cm, number of pixels 500 x 500, positioned at 17 m from the moderator.
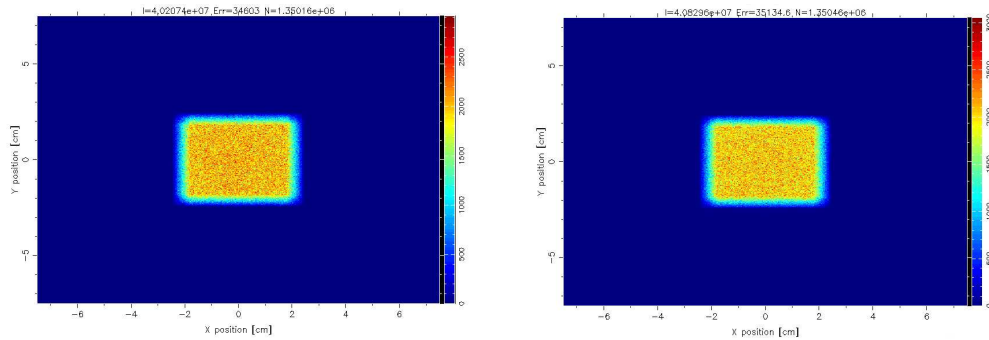
Figure 6.5. – PSD monitor at the sample position which detects all the neutrons intersecting the sample position, regarding the old moderator (left) and the new one (right).

6.2.4. Beam divergence

In this section, the simulations in relation to the beam divergence are presented, we used the specific divergence monitor put at the sample position. There are no noticeable differences in the neutron beam divergence between the two moderator models, see Fig. 6.6, for both the models the divergence lies within ±0.2º.

Divergence monitor specifics: X-range [-1, 1] deg, Y-range [-1, 1] deg, width = 4 cm, height = 4 cm, number of pixels 500 x 500, positioned at 17 m from the moderator.
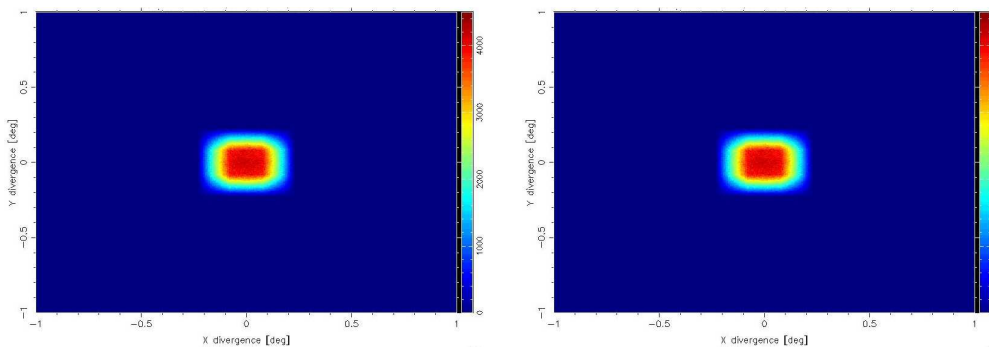
Figure 6.6. – Divergence monitor at the focus position, which detects all the neutrons intersecting the sample position, regarding the old moderator (left) and the new one (right).

6.3. Full TOF profile

A meaningful analysis of a neutron beam from a pulsed source consists in the study of the TOF properties of the moderator for a single energy/wavelength and not only for the whole spectrum. To perform an analysis in an approximate single wavelength range, the wavelength of the simulated beam was set as a very narrow interval.

6.3.1. Preparatory TOF analysis

In order to perform initial analysis of TOF profiles, we assumed that the energy monitor analyzes a range from 0.1 to 1000 meV and utilizes 5000 channels, i.e. the width of a single energy step was about 0.2 meV. To ensure that the slices of energy were narrow enough, they were set ten times narrower than a monitor channel. In this way, an energy peak was made sharp enough to be collected in a single energy step and statistical oscillations between near channels may be avoided. Therefore the selected energy ranges are $E_i \pm 10 \, \mu eV$. Considering that TOSCA is a TOF spectrometer, the analysis was performed for the TOF spectrum at the sample position. The peaks in most of the energy ranges have similar intensities for the old and the new moderator model, Fig. 6.7. Albeit some differences in the TOF FWHM can be observed for long wavelengths, see Tab. 6.1.
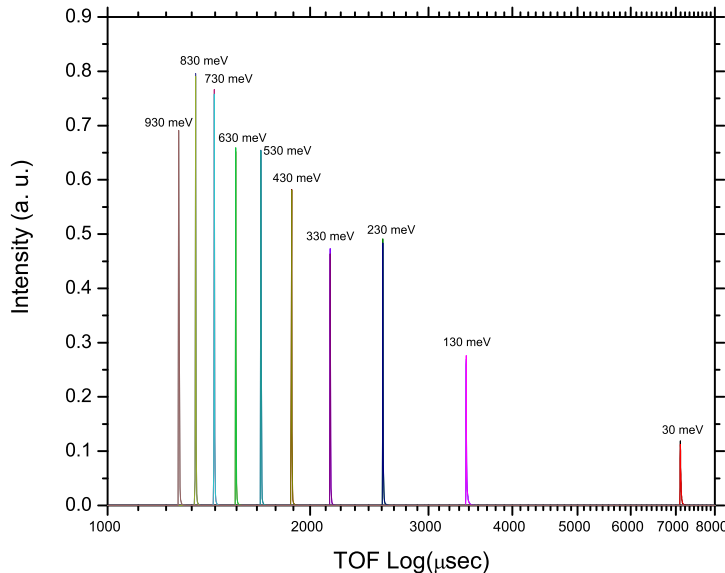
Figure 6.7. – TOF spectra at the sample position for a single energy ranges.

Wavelength ($\mathring{A}$)	Energy (meV)	FWHM old mod. (μsec)	FWHM new mod. (μsec)
1.651	30	18.591	18.592
0.793	130	7.623	7.624
0.596	230	4.629	4.629
0.498	330	5.224	5.224
0.436	430	4.272	4.272
0.393	530	3.753	3.753
0.360	630	3.819	3.819
0.335	730	3.279	3.279
0.314	830	3.368	3.368
0.297	930	3.596	3.596

Table 6.1. – FWHM of the TOF peaks at the sample position for single wavelengths.

6.3.2. Full TOF analysis

A second and more extensive analysis of the time features was performed, in which more wavelength ranges were analyzed. The monochromatic neutrons were detected in front of the moderator as well as at the sample position. The aim of these simulations was to provide a detailed description of the time profile for both models, as this feature can affect the resolution that TOSCA simulations can achieve. For every simulation that follows, a range with a span of $10^{-6}\,\mathring{A}$ around the selected wavelength was used.

To evaluate the FWHM of the TOF peaks, we exploited a fitting function that resembles the shape of the peak. One of the suitable expressions that can be used in order to fit such a shape is presented in eq. 6.1. One can see from Fig. 6.8 that the fit resembles the TOF curve and the FWHM can be estimated with adequate accuracy. In fact, the TOF peaks have generally a sharp rise and a slower exponential-like decay, see Fig. 6.11 and Fig. 6.12.
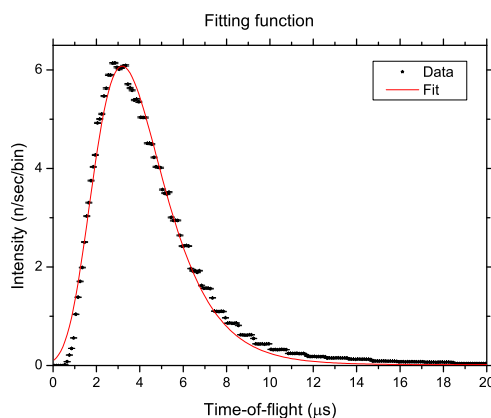
Figure 6.8. – Fit performed for a TOF peak by simulating a narrow λ interval.

$$y(x) \;=\; y_0 + A \cdot exp\left[-exp\left(-\frac{x - x_c}{w}\right) - \frac{x - x_c}{w} + 1\right] \tag{6.1}$$

Analysis at the moderator outlet

The neutrons were detected at just 1 μm away from the moderator's face, in order to avoid noticeable modifications in the TOF profile due to the traveling time of the neutrons from the moderator to the monitor. For each run, 10^7 neutrons were simulated. The difference between the FWHMs calculated by using the two different models lies within 6 % for $\lambda < 5\,\text{Å}$, and becomes larger for higher wavelength, see Tab. 6.2. Nevertheless, wavelengths higher than $\sim 4.5\,\text{Å}$ are not selected by the TOSCA analyzers, as explained in Chapter 5, so they are of no practical significance for INS experiments on this instrument. They could be of some importance only for diffraction measures, which are not frequently exploited on TOSCA presently.

Analysis at the sample position

The following data were collected at 17 m from the moderator to study how the monochromatic profiles spread in time along the beam-line. The FWHM of the profiles in this position is an indication of the theoretical TOF resolution that TOSCA can achieve. 10^7 neutrons were simulated for each run. For both the outlet and the sample position, one can observe that the FWHM values along the wavelength spectrum are nearly similar between the two models, although the new moderator seems to have more accurate modeling and a smoother trend, see Fig. 6.9 and Fig. 6.10. Also the statistical errors of the fitting related to the old model are generally bigger. This is due to the irregular profile shape that the old model shows once the spectrum reach long wavelengths, as shown in Fig. 6.12, which affects the accuracy of the fit function. Conversely, the new moderator model shows to have an appropriate shape of the profiles even at long wavelengths. Also in this comparison, the difference between the FWHMs lies within 6 % for $\lambda < 5\,\text{Å}$, while at longer wavelengths the new model shows more coherent results and a better modeling performance, see on page 57. For these reasons it may be preferable to use the new model when performing simulations regarding diffraction spectra on TOSCA, in which good modeling of the pulses at long wavelength might be significant.

Wavelength (Å)	Energy (meV)	FWHM old mod. (μsec)	FWHM new mod. (μsec)	Difference (%)
0.286	1000.11	1.88	1.84	2.13
0.375	580.95	2.52	2.60	3.17
0.465	379.15	3.19	3.14	1.57
0.554	266.78	3.81	3.90	2.36
0.643	197.86	4.66	4.58	1.72
0.732	152.57	5.60	5.49	1.96
0.822	121.22	6.70	6.71	0.15
0.911	98.62	8.28	8.45	2.05
1.000	81.81	9.75	9.40	3.59
1.500	36.36	16.31	15.96	2.15
2.000	20.45	18.44	19.51	5.80
3.000	9.09	22.08	22.18	0.45
4.000	5.11	21.96	23.04	4.92
4.885	3.43	22.47	23.29	3.65
5.000	3.27	24.87	23.26	6.47
6.000	2.27	26.41	24.31	7.95
7.000	1.67	23.89	24.29	1.67
8.000	1.28	27.16	24.77	8.80
9.000	1.01	21.22	23.91	12.68
10.000	0.82	31.09	25.90	16.69

Table 6.2. – TOF FWHM in a single wavelength ranges at a distance of 1 μm from the moderator's face.
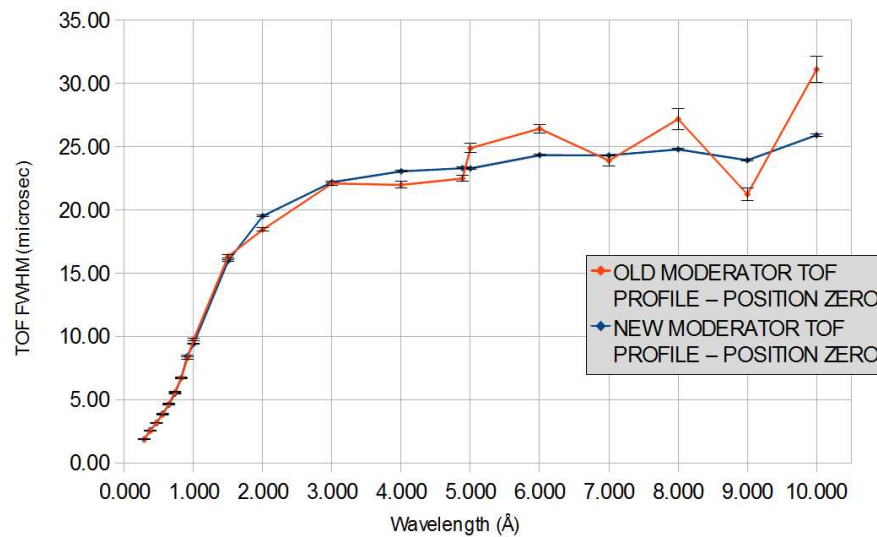
Figure 6.9. – TOF FWHM profile at a distance of 1 μm for both moderator models as a function of wavelengths.

Wavelength (Å)	Energy (meV)	FWHM old mod. (μsec)	FWHM new mod. (μsec)	Difference %
0.286	1000.11	1.88	1.84	2.13
0.375	580.95	2.52	2.60	3.17
0.465	379.15	3.20	3.15	1.56
0.554	266.78	3.82	3.92	2.62
0.643	197.86	4.70	4.62	1.70
0.732	152.57	5.71	5.58	2.28
0.822	121.22	6.91	6.95	0.58
0.911	98.62	8.71	8.93	2.53
1.000	81.81	10.41	10.01	3.84
1.500	36.36	17.54	17.44	0.57
2.000	20.45	20.02	21.19	5.84
3.000	9.09	23.55	24.11	2.38
4.000	5.11	23.75	24.97	5.14
4.885	3.43	24.48	25.31	3.39
5.000	3.27	27.09	25.28	6.68
6.000	2.27	26.96	26.08	3.26
7.000	1.67	24.46	26.30	7.52
8.000	1.28	27.68	26.72	3.47
9.000	1.01	22.14	26.21	18.38
10.000	0.82	30.63	27.83	9.14

Table 6.3. – TOF FWHM in a single wavelength ranges at a distance of 17 m from the moderator's face.

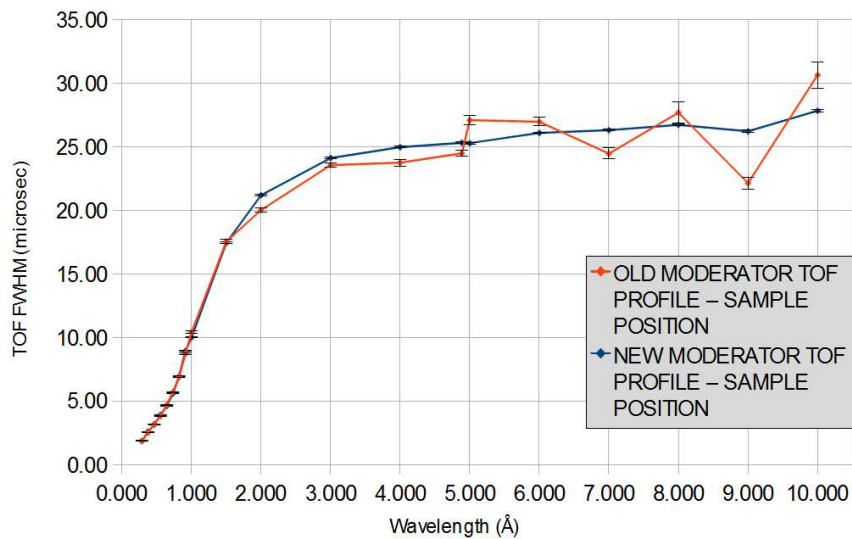**Figure 6.10.** – TOF FWHM profile at a distance of 17 m for both moderator models as a function of wavelength.

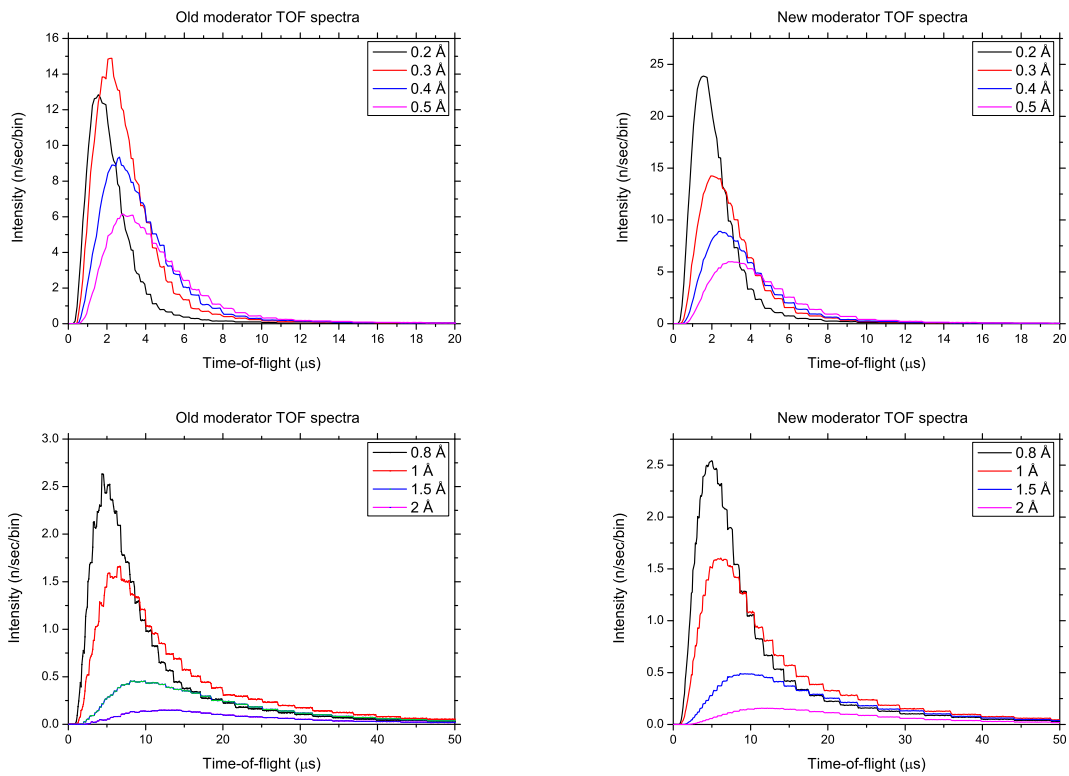## TOF profiles for a particular wavelengths

Figure 6.11. – TOF profiles for a single wavelength for the old moderator (left) and the new moderator (right).
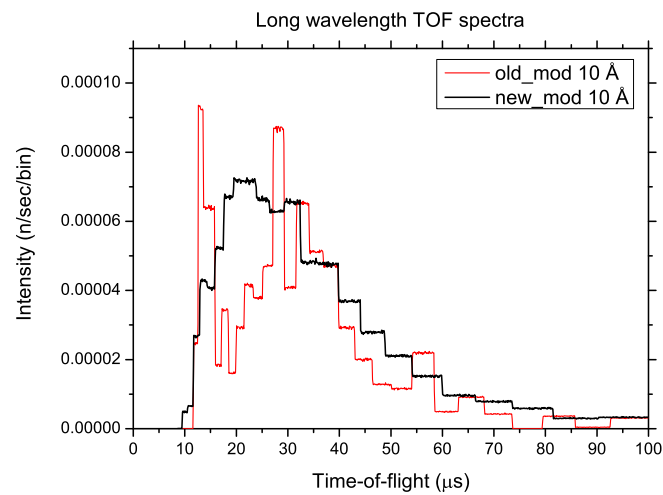

Figure 6.12. – TOF profiles for the long wavelengths.

6.4. Validation of the McStas model

This section presents an analysis of the neutron beam generated by McStas simulations using the TOSCA 2007 moderator model. Previously, we have shown that the spectra given by the 2007 moderator model and the 2013 model do not differ substantially in spectrum shape and normalized intensity, although the latter model has better performance in TOF modeling for $\lambda \geq 5$ Å. However, we continued to use the 2007 model in benchmarking with the experimental results, since the differences were not significant for the wavelengths of interest. The experimental spectrum was collected by the detector No. 141 (TOSCA beam monitor) placed between the moderator and the sample at 15.794 m from the moderator. This detector is a scintillating glass in which lithium oxide spheres are dispersed, the dimension and position of the spheres are studied to have a low and uniform attenuation of the beam. In fact, since the detector is placed before the sample, it has deliberately low absorption efficiency and the experimental raw data must be corrected by the calibration function. The detector No. 141 and its efficiency correction function are described in section 5.4 of this thesis. In the simulations instead, a wavelength monitor with dimensions of 40 x 40 mm^2 and ideal efficiency collected the incoming spectrum. The intensity value, measured in units of $\frac{n}{s\,\text{\AA}}$, is not the same as the experimental one because the ratio between the scintillating area and the beam area is different. Nevertheless, the curve shape and the normalized intensity correspond to each other. Indeed, the raw data collected during the experiment were corrected by the detector calibration function and subsequently normalized by the integral of the resulting curve. The data calculated during the simulation instead do not require efficiency calibration and were thus directly normalized by the integral of the curve itself.

The comparison between the experimental and simulated results is shown in Fig. 6.13, which points at that the two curves have similar intensity and shape. Differences can be seen at small wavelengths and long wavelengths, while in correspondence of the fingerprint region, around 0.75 Å, the two curves intersect each other. Particularly, the experimental curve has higher intensity for $\lambda < 0.75$ Å and lower intensity for $\lambda > 0.75$ Å than the simulated curve; this higher intensity at lower wavelength (i.e. higher energy) may be explained by a slight misalignment of the shutter relatively to the moderator outlet during the experiment. This eventuality can cause the collection of under-moderated neutrons scattered from the beryllium reflector which surrounds the moderator. Equally, the presence of aluminium windows along the beamline, with a typical thickness of 0.5 mm may cause differences between the experimental and simulated spectrum. These windows are useful to separate different sections of the beamline kept under vacuum, as explained in section 5.5 of this thesis. They were not included in the simulations since they add complexity to the simulated instrument while their influence on the final values is not prevailing. Indeed, neutrons can travel large distances through most materials without being scattered or absorbed. The linear attenuation of a neutron beam by aluminium is

about 0.01 mm^{-1} compared with the 0.99 mm^{-1} for x-rays. Aluminium has a neutron scattering cross section for thermal neutrons of 1.5 barns, and its scattering is mostly coherent, thus its signal can be isolated and subtracted in the spectrum [24]. In summary, the simulated spectrum shows a decent agreement with the experimental one within the main wavelength range of TOSCA, which spans approximately between 0.5 and 3 Å. In this range, the relative difference between the two curves lies approximately within 20%, see Fig. 6.14.
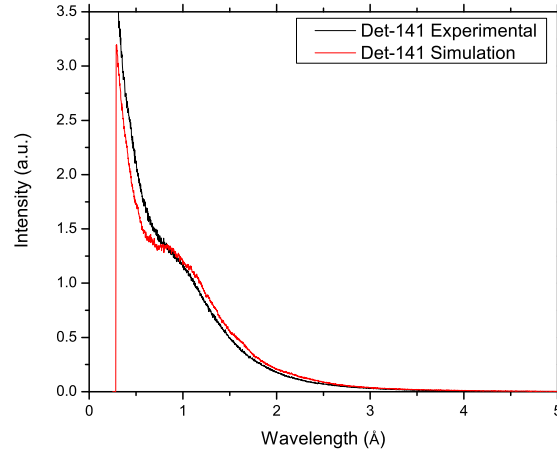
Figure 6.13. – Comparison between the experimental and the simulated wavelength spectra of TOSCA.
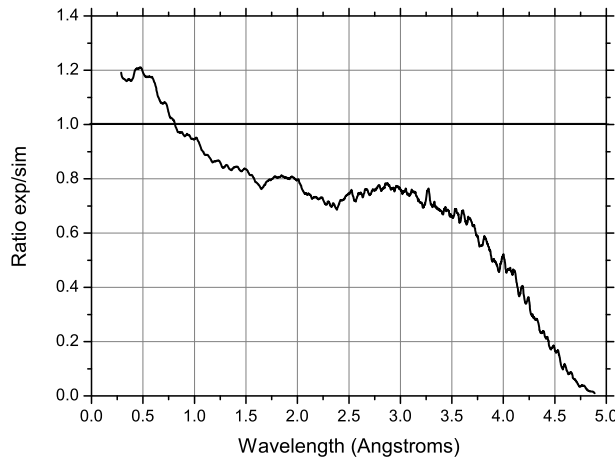
Figure 6.14. – Ratio between the experimental and the simulated wavelength spectra.

7. Benchmarking of the spectrometer diffraction capabilities

7.1. Overview

We performed experiments with Highly Oriented Pyrolythic Graphite (HOPG) samples on the real instrument, as a term of comparison to assess the performances and accuracy of the McStas model of TOSCA. The simulated and measured data were collected in the same conditions. The sample reproduced in the simulation was set up considering its state of aggregation, type of the material, dimensions and orientation relatively to the beam. To this extent, the position and FWHM of the simulated and measured Bragg peaks can be compared.

7.2. Experimental setup

In this experiment, we measured the diffraction signal coming from a crystal of HOPG. This crystal shows a strong long-range order, therefore the peaks measured correspond to the neutron wavelength diffracted by the crystal following the Bragg Law, see Fig. 7.1a. The peaks are presented in d-spacing (Å) and TOF (μs). Considering the angle of incidence of the beam on the sample plane and the angular position of the detector, one can evaluate the spacing between two successive planes of the crystal from the diffracted wavelengths. In fact, the d-spacing position of each peak is related to the lattice distance d between the diffraction planes, the peak center can be the value d or its diffraction harmonics. Theoretically, there are n peaks, each one centred on the d-spacing value $\frac{d}{n}$. Another aim of this experiment is to compare the FWHM of each simulated peak with the related experimental peak. In this way, it is possible to ascertain the validity and accuracy of the McStas model regarding the primary spectrometer and the diffraction assembly. Furthermore, the FWHMs in TOF of the Bragg peaks reflect the time performance of the moderator, since the resolution of TOSCA diffraction assembly is generally determined by the pulse width of the moderator.

The measurements were performed on a 30 x 40 x 2 mm^3 HOPG standard (see Fig. 7.1b) kept at 10 K. The sample was aligned with the $a - b$ plane perpendicular

to the incident beam to perform diffraction on the 001 plane, which has a lattice spacing of 3.329 Å. The sample $c-axis$ was rotated by 0.86° and thus the neutron beam impinged at an angle of 89.14° on the crystal surface. This rotation was performed to maximize the Bragg signal from the 001 plane on the detector No. 147, which is placed at 178.28° relative to the beam direction, thus the correspondent signal is in back-scattering. The detector is 1.210 m away from the sample position, hence it fixes the total neutron fligth path at 18.210 m.

The mosaicity of the measured sample is 0.8°±0.2° along the $c-axis$. The crystal mosaic spread is defined as the angular deviation of crystal lattice planes from a perfectly ordered crystal structure, the diffracted spectrum changes with different values of crystal mosaic spread. A beam incident on a crystal with a null divergence satisfies the desired Bragg condition only if the mosaic spread of the crystal is zero. However, a real neutron flux incident on the crystal can never be of perfectly null divergence. The different orientation of the planes hence allows diffraction of neutrons impinging at slightly different angles, this increase the detected signal at detriment of the resolution. The divergence of the incident beam on TOSCA is not experimentally assessed yet, it depends on the geometry of the beamline, which is known, and on the divergence of the neutrons coming out of the moderator, which is not available in the literature. From the simulation results presented in Chapter 6, we can assume for the divergence to be reasonably small ($< |0.2|°$) thanks to the collimation beamline. The measured data are collected by ^3He tube diffractometers in the TOF mode with logarithmic binning and subsequently the data can be converted in d-spacing, since the angle of Bragg diffraction is fixed (89.14°).
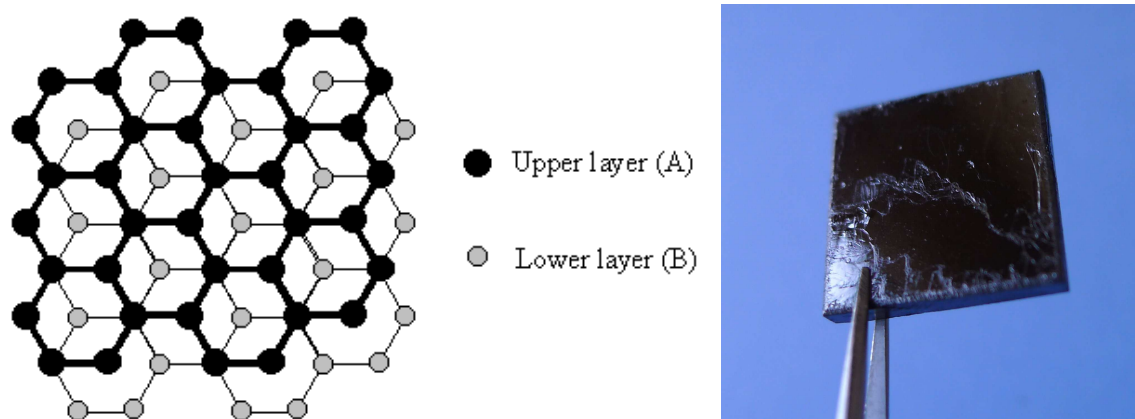
Figure 7.1. – a) Structure of the HOPG lattice is shown on the left and b) appearance of the sample, on the right.

7.3. Simulation setup

The simulation has reproduced an HOPG plate with d-spacing of 3.329 Å between the planes normal to the neutron beam. The first order of diffraction was not measured in the experiment because of the low intensity of the related signal. The physical properties and dimensions of the simulated sample resemble those of the real one, while the mosaicity has been set to 0.8°. A model of the detector No. 147 that measures in TOF mode with logarithmic binning was used to detect the diffracted neutrons. The divergence of the experimental beam on the sample position was set deliberately small to minimize the resolution of the calculated peaks. In fact, this divergence in relation with the mosaicity of the sample can affect the resolution of the system. The aim of the simulation was to calculate the lower limit in the resolution with this sample, thus some choices needed to be made:

- The simulated beam is strongly collimated and focused directly on the sample, with a divergence $<|0.1|°$ at the sample position.

- The d-spacing spread, $\Delta d/d$, of the sample is set to zero.

- The Debye-Waller factor is not considered so as to raise the time efficiency of the simulation, since this factor dampens the coherent scattering within the sample.

7.4. Benchmarking

The performance of an inverted-geometry instrument like TOSCA critically depends on the time structure of neutron pulses reaching the sample position. On TOSCA, experimental access to this information is facilitated by the availability of a high-resolution diffraction bank in backscattering geometry. In this configuration, the observed time widths of well-defined Bragg reflections become most sensitive to the temporal spread of neutron pulses arriving at the sample position, as detailed in recent Monte Carlo simulations of the OSIRIS spectrometer [21]. The following comparisons between experimental and simulated performance are primarily concerned with a characterization of the primary spectrometer. The data were analyzed by least-squares fits of the experimental and simulated data using the function presented in section 6.3.2. All widths reported in this work correspond to full-width-at-half-maxima (FWHM).

7.4.1. D-spacing

The positions of the experimental and simulated peaks overlap with good approximation, the relative differences are all within 0.3 %, see Tab. 7.1. This value of deviation is within the statistical error. As expected, the simulated FWHMs are

lower than the measured ones, thus defining the ideal resolution. The data about the widths are also listed in Tab. 7.1 and shown in Fig. 7.2. The calculated results show excellent agreement with the measurements in the range between 1 Å and 2 Å. These results also highlight the high d-spacing resolution of the instrument, $\Delta d/d \simeq 5 \cdot 10^{-3}$ over its operating wavelength range. This unique feature of inverted-geometry instrumentation at a short-pulse spallation neutron source could be further exploited via a significant increase in detector area relative to the current (and quite modest) capabilities on TOSCA, as it has been already demonstrated on the low-energy spectrometer OSIRIS [28].

7.4.2. Time-of-Flight

The results of this benchmarking are also presented in TOF which is the technique of measurement on TOSCA, as explained in Chapter 5. As expected, the resolution of the simulated peaks is better than the experimental ones because the McStas model reproduces the ideal experimental condition, see Tab. 7.2 and Fig. 7.3a. Nevertheless, the resolutions are in excellent agreement, within the statistical error, for $\lambda > 1$ Å. From the results, one can see that the simulated resolution for thermal and cold neutrons is close to the real one, while the values diverge for epithermal neutrons. The ideal conditions of the simulation make the difference in the high-energy range, because the epithermal neutrons are more difficult to detect and they have a lower scattering cross section. Thus in the experiments, the resolution at low wavelength (high energy) is worse than in the sub-thermal region and the correspondent peaks show lower intensity and lower signal to noise ratio. Furthermore, in both cases the widths are dominated by the temporal response of the primary spectrometer and, in particular, the time structure emerging from the moderator face, see Fig. 7.3b. Other contributions associated with the time uncertainties between the moderator and the sample are relative minor in comparison. At the longest wavelength investigated (3.33 Å), simulations are within 10% of experimental values, and consistently provide a safe lower bound to observation. These results are also in agreement with a moderator performance of $\sim 12\,\mu s/$Å inferred from previous calibrations of the instrument [6, 23]. On the basis of the present comparison, this moderator term provides a good description of time structure below ca. 3.0 Å. At the higher wavelength investigated, the time width shows signs of saturation, as one would expect for the moderation of cold neutrons at a short-pulse spallation source [8].

Diffraction order	Experiment peak position (Å)	Simulation peak position (Å)	Experiment FWHM (Å)	Simulation FWHM (Å)
$\lambda/2$	1.6646	1.6668	0.0040	0.0034
$\lambda/3$	1.1095	1.1116	0.0028	0.0027
$\lambda/4$	0.8323	0.8338	0.0024	0.0024
$\lambda/5$	0.6660	0.6672	0.0020	0.0019
$\lambda/6$	0.5550	0.5559	0.0017	0.0015
$\lambda/7$	0.4757	0.4764	0.0015	0.0011
$\lambda/8$	0.4163	0.4168	0.0013	0.0009
$\lambda/9$	0.3700	0.3705	0.0012	0.0007
$\lambda/10$	0.3331	0.3334	0.0011	0.0006
$\lambda/11$	0.3028	0.3031	0.0010	0.0005
$\lambda/12$	0.2776	0.2778	0.0011	0.0005
$\lambda/13$	0.2564	0.2565	0.0015	0.0005
$\lambda/14$	0.2378	0.2381	0.0034	0.0004
$\lambda/15$	0.2218	0.2223	0.0009	0.0004

Table 7.1. – Measured and calculated values for the neutron diffraction peaks due to HOPG. Peak positions are in d-spacing and the correspondent FWHMs are listed as well.
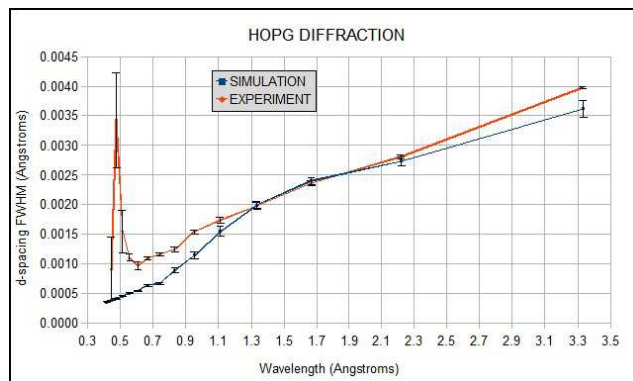
Figure 7.2. – Comparison of the peak FWHMs in d-spacing, for measured and calculated results.

Diffraction order (Å)	Experiment peak position (μs)	Simulation peak position (μs)	Experiment FWHM (μs)	Simulation FWHM (μs)	Experiment relative resolution %	Simulation relative resolution %
λ/2 (3.329)	15324	15344	36.60	31.56	0.239	0.206
λ/3 (2.219)	10214	10233	25.86	24.77	0.253	0.242
λ/4 (1.664)	7662	7676	21.72	22.14	0.284	0.288
λ/5 (1.332)	6131	6142	18.22	17.94	0.297	0.292
λ/6 (1.110)	5109	5117	15.94	14.24	0.312	0.278
λ/7 (0.951)	4379	4385	14.11	10.42	0.322	0.238
λ/8 (0.832)	3832	3837	11.52	8.35	0.300	0.218
λ/9 (0.740)	3406	3410	10.71	6.35	0.315	0.186
λ/10 (0.666)	3066	3069	10.11	5.87	0.330	0.191
λ/11 (0.605)	2787	2790	8.93	4.92	0.321	0.176
λ/12 (0.555)	2555	2558	10.22	4.58	0.400	0.179
λ/13 (0.513)	2360	2361	14.25	4.17	0.604	0.177
λ/14 (0.476)	2189	2192	31.56	3.75	1.442	0.171
λ/15 (0.444)	2042	2046	8.40	3.41	0.411	0.166

Table 7.2. – Measured and calculated values for the neutron diffraction peaks due to HOPG. Peak positions are in TOF and the correspondent FWHMs are listed as well.
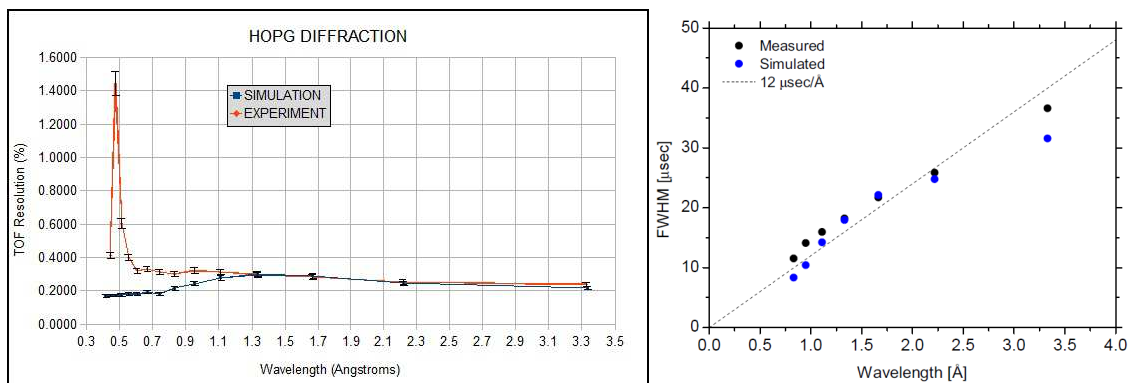
Figure 7.3. – a) The comparison between the measured and calculated resolution for different d-spacing values is shown on the left. b) Measured and calculated FWHM time widths as a function of incident neutron wavelength are shown on the right. The line represents the time performance of the moderator.

7.4.3. Diffraction spectra

For completeness, we present the measured and calculated diffraction spectra as they appear after the normalization by the incident monitor spectrum. As discussed earlier the peaks overlap in the two cases, although the intensities of the peaks in the two plots do not match because the simulated sample has been set with ideal reflectivity, thus every neutron that satisfied the Bragg condition was diffracted. This choice was made to collect every profitable neutron and thus to save computational time. In fact, the main purpose of this benchmark was not the comparison of peak intensity but rather the study of their position in d-spacing and their FWHM. In the experiment, the neutrons tend to scatter less as the wavelength decreases, this causes a decreasing intensity of the peaks towards small d-spacing values, see Fig. 7.4.
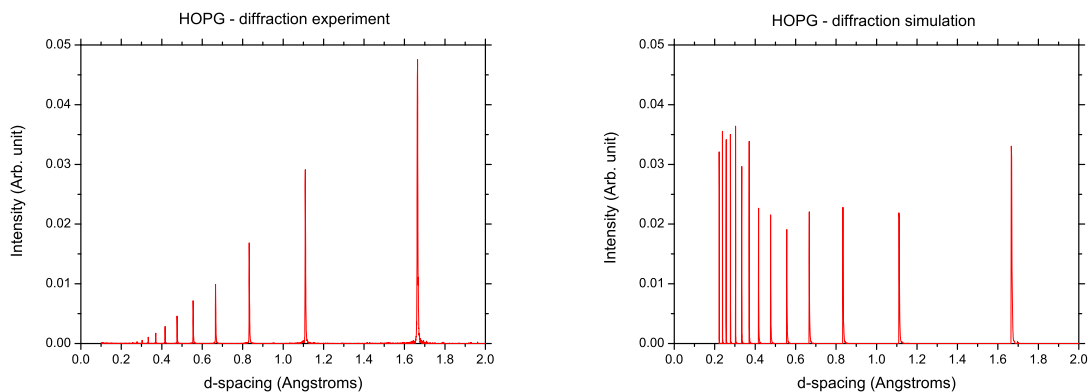
Figure 7.4. – Spectra collected from the HOPG sample in the experiment (left) and the simulation (right); both spectra are normalized by the corresponding incident monitor spectrum, which collects the TOF spectrum of the neutrons falling on the sample.

8. Benchmarking of the INS spectrometer

8.1. Overview

The comparisons between experimental and simulated performance presented in Chapter 6 and 7 were primarily concerned with a characterization of the primary spectrometer. To assess the validity of our current description of the instrument, we have also compared experimental and simulated spectra around the elastic line for water ice at 10 K. For the purposes of benchmarking the McStas simulations, this case represents a convenient scenario characterized by high scattering levels (potentially leading to an increase in instrumental backgrounds), as well as comparable contributions to the resolution function from both primary (moderator) and secondary spectrometers (inelastic banks).

8.2. Experimental setup

In this experiment, the sample loaded on TOSCA was contained in a squared aluminium container with dimensions of 40 x 40 x 2 mm^3 that was attached to an aluminium centrestick so that its centre is at a distance of 1165 mm from the top of the cryostat and is well overlapped with the neutron beam, see Fig. 8.1. The TOSCA pit is a cryostat which provides an experimental environment of low pressure (5 mbar) and low temperature ($<$10 K). Before loading the sample, the cryostat had to be filled with helium at a pressure slightly higher than 1 bar to be able to access the chamber and at the same time to have an outward flow of He gas, this procedure is needed in order to avoid contamination of the cryostat by air during the sample changes. Once the sample was set in place, we were able to seal the cryostat and to start creating the vacuum down to a pressure of 20 mbar of He. We kept the pressure above the minimum at this stage to speed up the cooling process of the sample, in fact the cryo-system surrounds the vessel wall and the heat exchange between the sample and the vessel is mediated by the remaining He. By the time the sample reached a temperature of 10 K the pressure has fallen down to the final threshold of 5 mbar because of the decrease in temperature. The experiment was run until we accumulated 500 mAh of the beam. As sample material, we chose pure H_2O ice of the type $1h$.

Figure 8.1. – The aluminium centrestick for use on TOSCA. On the right hand side, one can see the attached squared sample cell.

8.3. Simulation setup

This simulation has reproduced a H_2O ice sample of type $1h$, with dimensions of 40 x 40 x 2 mm^3. The McStas models of TOSCA back-scattering and forward-scattering banks were used as well as the actual model of the primary spectrometer. The components used in the simulations are presented in Chapter 4 and the implemented INS banks are explained in Chapter 5. The spectroscopic file exploited to resemble the real sample in McStas was $H_2O - ice - 1h.laz$.

8.4. Benchmarking

In the simulations, the elastic line is set to 3.8 meV as first harmonic of the monochromators, determined by the experimental setup of the instrument [6]. All the curves were fitted using the Gaussian function to assess the parameters. As mentioned earlier, the sample used in this experiment is 1h-water ice kept at 10 K. As shown in Fig. 8.2 and Fig. 8.3, the agreement between the experiment (FWHM = 2.41 cm^{-1}) and simulation (2.35 cm^{-1}) is excellent, further confirming the adequacy of our computational model for a quantitative description of the spectroscopic response of the instrument.

8.4.1. Back-scattering elastic line results

Back-scattering signal	Peak center (meV)	FWHM (meV)	TOF FWHM (μs)	Fit reduced χ^2	Resolution %
Experiment	-0.094 ± 0.002	0.300 ± 0.004	817	0.0011	7.89
Simulation	-0.098 ± 0.001	0.292 ± 0.002	795	0.0004	7.68

Table 8.1. – Experimental and calculated results for the back-scattering elastic line of TOSCA spectrometer with pure water ice sample. The energies are intended as energy transfer from the 3.8 meV elastic line, the resolution is calculated in reference to this value.
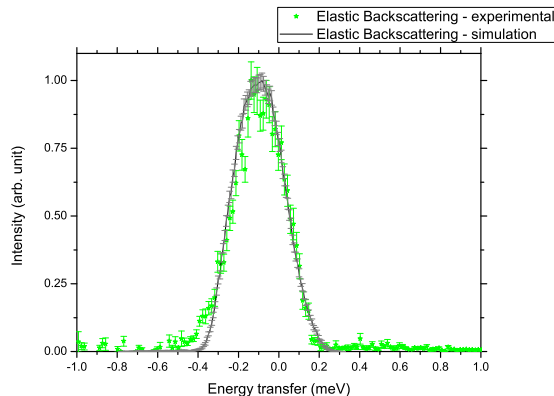
Figure 8.2. – Benchmarking between the experimental and the calculated elastic line of the back-scattering spectrometer with pure water ice-1h sample.

8.4.2. Forward-scattering elastic line results

Fwd-scattering signal	Peak center (meV)	FWHM (meV)	TOF FWHM (μs)	Fit reduced χ^2	Resolution %
Experiment	-0.075 ± 0.003	0.291 ± 0.004	792	0.0074	7.66
Simulation	-0.102 ± 0.001	0.291 ± 0.001	792	0.0003	7.66

Table 8.2. – Experimental and calculated results for the forward-scattering elastic line of TOSCA spectrometer with pure water ice sample. The energies are intended as energy transfer from the 3.8 meV elastic line, the resolution is calculated in reference to this value.
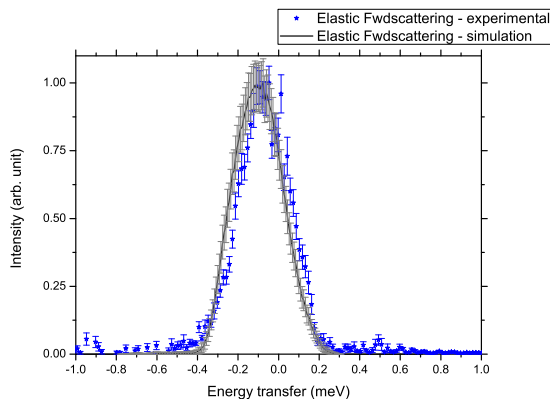
Figure 8.3. – Benchmarking between the experimental and the calculated elastic line of the forward-scattering spectrometer with pure water ice-1h sample.

The water ice $1h$ is a strong incoherent scatterer due to its high content of the hydrogen isotope ^1H. This isotope has $\sigma_{coh} = 1.7583\,b$, $\sigma_{incoh} = 80.27\,b$ and $\sigma_{abs} = 0.3326\,b$ [1]. Hence, this material is a good candidate for the study of the TOSCA elastic line.

9. Effects of the neutron guide on TOSCA

9.1. Overview

In view of current developments in chemical spectroscopy with neutrons around the globe, the current sensitivity of TOSCA could be greatly enhanced via the provision of a neutron guide in the primary spectrometer. To assess possible gain factors relative to current capabilities, extensive McStas simulations have been performed for a range of guide configurations. This exercise must necessarily take into account the cost effectiveness of any proposed guide geometry, as well as other spatial and operational constraints.

9.2. Proposed upgrade on TOSCA

At the moment there is increased competition in the area of molecular spectroscopy with neutrons. There are two new instruments that can study similar part of the vibrational spectrum as TOSCA: VISION at SNS (USA) and LAGRANGE at ILL (France). The instrument VISION is currently under construction and it is plausible that VISION total flux at the sample position will be 50 or 100 times the flux of TOSCA. This is due to the higher power of SNS source and the fact that VISION has a neutron guide, which directs the neutrons to the sample more effectively than the simple TOSCA collimation tube. These facts, in conjunction with the larger VISION's effective detector area and higher resolution crystal analyzers can make TOSCA lose competitiveness in the spectroscopy research field. To keep TOSCA in a competitive position, the installation of neutron guide has been taken into account. This upgrade will substitute the current collimator with a supermirror guide and it will lead to an increase in the neutron flux at the sample position. The improved neutron flux will allow measurements with a better signal-to-noise ratio, i.e. it will be possible to record the same spectrum quality as before within shorter period of time. Furthermore, the upgrade will allow experiments with samples of smaller mass. However, it is worth to specify that TOSCA has a unique advantages over other instruments of this kind. In fact, thanks to its 10 Hz chopper, TOSCA has the access to the elastic line at $3.5 \sim 4$ meV. It can also measure the quasi-elastic and inelastic region with a resolution of $\Delta\omega/\omega \approx 1.25\,\%$ that is reasonably constant

in the 3.5 - 1000 meV region and $\Delta\omega \approx 300\,\mu$eV at the elastic line. VISION in the present configuration instead cannot access the elastic line but can only access the 5 - 1000 meV region. Prior to the commissioning of TOSCA upgrade, it is necessary to perform extensive simulations by Monte-Carlo codes to study how this upgrade will affect the incident spectrum. The simulations will also allow to evaluate the most suitable geometrical configurations and to optimize the choice of m factors that will characterize every section of the supermirror guide. The needed TOSCA computational model and calculations were fully developed and performed within the framework of this thesis. Fig. 9.1 shows the project made by ISIS Engineering Group of the neutron guide along the TOSCA beamline. The validity of this geometry was confirmed by the McStas simulations, thus the proposed guide was kept as adherent as possible to this conceptual design in order to facilitate the subsequent development and realization of the guide.

9.2.1. Guide geometry

Initially, the current configuration of TOSCA (described in Chapter 5) was simulated in order to have the baseline of the instrument as a term of comparison for the subsequent simulations regarding the gain due to the neutron guide on the beamline. The final configuration of the neutron guide is presented in Tab. 9.1. A neutron guide can be straight, tapered or elliptical. According to the simulations performed by J. F. Castanon [5], the flux gain on TOSCA is superior if a tapering neutron guide is installed rather than a straight one. Furthermore, the performance of an elliptic guide resulted comparable to that of a tapering guide for the TOSCA case, thus there is not a valid reason to choose a more complex geometry like the elliptical. In fact, as known from VISION and confirmed in [5], a tapered guide appears to be the most efficient geometry for a TOSCA type instrument. We performed additional simulations to identify the optimal geometry, finally the choice fell upon a mixed straight and tapered neutron guide. Depending on the energy range of interest, the slope of the tapering guide can be calibrated. More tapered mirrors placed at the end of the guide give greater gain at low energies. A constant slope through all the guide balances the gain and compensate decreasing the gain for thermal neutrons and increasing the gain for epithermal neutrons [5]. Since the INS experiments performed on TOSCA benefit from higher flux of epithermal neutrons, a constant angle of tapering is the best option. Thus, the angle is kept equal in each tapered section and it has been set to $\sim$0.138151°; the sections $g1$ and $g6$ are instead kept straight because those section are peculiar in the real beamline. The section $g1$ is inserted in the shutter and its optimum geometry results to be straight and with an aperture of 100 x 100 mm^2 [5]. In most of the following calculations, the configuration in which the guide $g1$ is not installed was also considered. In fact, due to the complexity of installing a guide inside the shutter, it is useful to evaluate its single effect within the guide assembly to justify its installation. The $g6$ section of guide has been considered with m = 0 as it is foreseen to be the point of insertion of a vacuum

pump, hence it is likely that the $g6$ section of the guide will not be installed. There are also gaps along the guide as indicated, which are intended as empty spaces between different sections. This geometry provides a total guide length of 14.414 m. The McStas model of TOSCA is shown in Fig. 9.2 and visualized through the MatLab 3D engine.

In summary, a tapered guide represents the most sensible geometry to transmit neutrons over a wide wavelength range. Such a guide can be placed at a minimum distance from the moderator of 1.625 m with a cross sectional area of 100 x 100 mm^2, followed by thirteen independent sections ending at a distance of 0.75 m from the sample position and 40 x 40 mm^2 cross section [20].

ELEMENT	Start at (m)	w_{in}, h_{in} (m)	w_{out}, h_{out} (m)	Length (m)	Input (m^2)	Output (m^2)	Coating (m^2)
Moderator	0	–	–	–	–	–	–
g1 straight (shutter)	1.625	0.1000	0.1000	1.938	0.01000	0.01000	0.77520
Gap 1	3.563	0.1000	0.1000	0.110	–	–	–
g2	3.673	0.1000	0.0928	1.500	0.01000	0.00861	0.57831
g3	5.173	0.0928	0.0889	0.800	0.00861	0.00791	0.29070
Gap 2	5.973	0.0889	0.0889	0.003	–	–	–
g4	5.976	0.0889	0.0817	1.500	0.00791	0.00667	0.51181
g5	7.476	0.0817	0.0744	1.500	0.00667	0.00554	0.46843
g6 straight (valve)	8.976	0.0744	0.0744	0.034	0.00554	0.00554	0.01013
g7	9.010	0.0745	0.0725	0.400	0.00554	0.00526	0.11759
Chopper gap	9.410	–	–	0.087	–	–	–
g8	9.497	0.0725	0.0708	0.360	0.00526	0.00501	0.10319
Gap 3	9.857	0.0708	0.0708	0.003	–	–	–
g9	9.860	0.0708	0.0634	1.538	0.00501	0.00402	0.41273
g10	11.398	0.0634	0.0559	1.538	0.00402	0.00313	0.36713
g11	12.936	0.0559	0.0485	1.538	0.00313	0.00236	0.32153
g12	14.474	0.0485	0.0411	1.538	0.00236	0.00169	0.27594
Gap 4	16.012	0.0411	0.0411	0.008	–	–	–
g13	16.020	0.0411	0.0400	0.230	0.00169	0.00160	0.03735
GUIDE END	16.250						

Table 9.1. – Geometry of the simulated neutron guide along the N8 beamline of ISIS. For further details see the text.

SIDE VIEW OF TOSCA PROPOSED NEUTRON
GLASS GUIDE UP TO 17m SAMPLE CENTRELINE
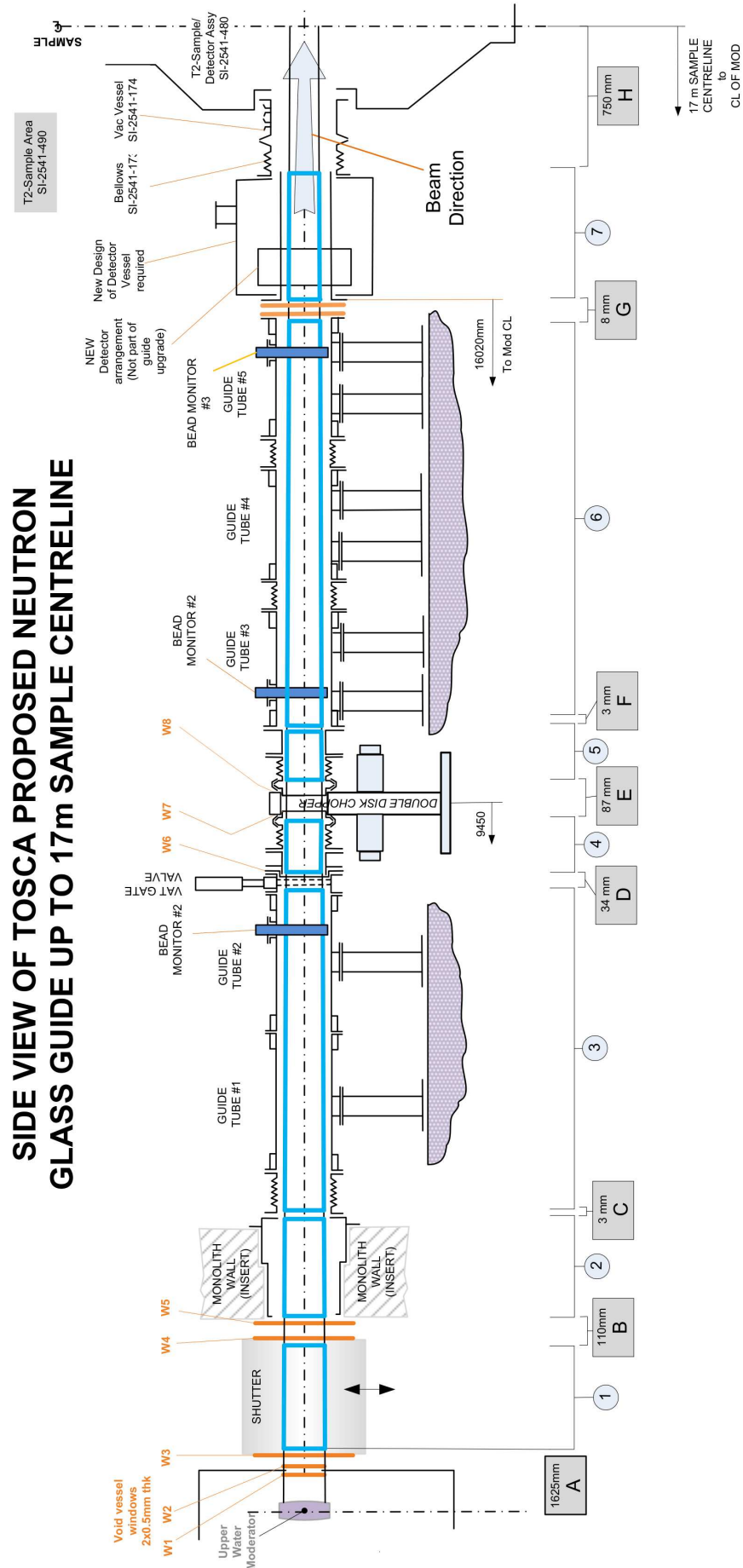
Figure 9.1. – TOSCA early proposal of the N8 beamline upgrade. Courtesy of ISIS Engineering Group.
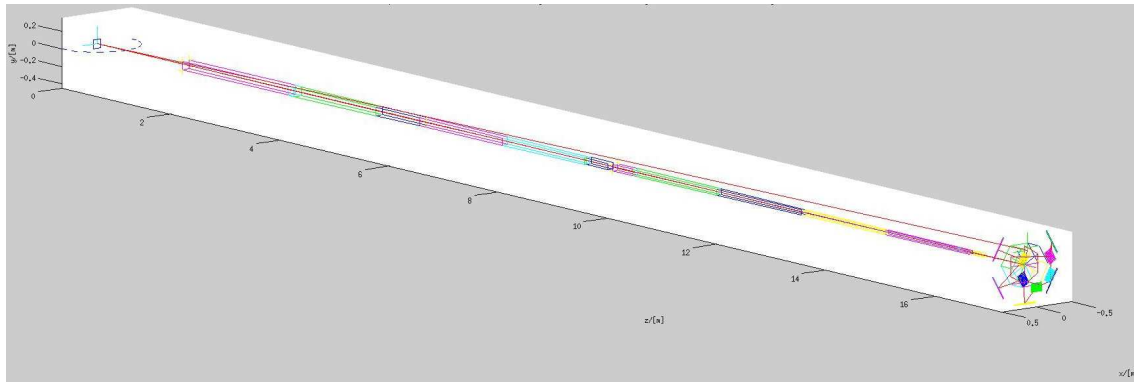
Figure 9.2. – TOSCA neutron guide assembly built with the help of McStas software package. The moderator (left) and the INS forward scattering assembly at the end of the guide (right) is shown.

9.3. Effect of the guide on TOSCA: results and discussion

TOSCA beamline has been built piece by piece to learn how to use McStas properly and to get used to its functions, and a new simulation was performed as soon as a new piece was set up. The first step was to configure TOSCA moderator. In the McStas user manual one can find a specific set of components which reproduce the moderators operating in ISIS target station 1. Since the specific moderator file was missing in the native libraries of the program, for the early tests used simple water at 300 K was used as the moderator. Though, this configuration was not properly correct because it did not reproduce the precise spectrum of neutrons used in TOSCA and INES. However, in these simulations about the neutron guide effects, the moderator file *h.tosca* has been added to simulate correctly the beam. This model was created by the neutronic group at ISIS in 2007, using MCNP-X calculations, and was used throughout the simulations performed here. The moderator was developed together with the contributed component ISIS_moderator.comp, which allows the inclusion of ISIS custom moderator models in a McStas instrument. In February 2013, ISIS neutronic group developed new McStas moderator models for Target Station 1. The comparison between the new moderator model of TOSCA and the 2007 version was discussed in Chapter 6. To calculate the performance of the supermirror neutron guide we used real reflectivity profiles for each different m-number, as explained in [33].

9.3.1. Spatial profile

In this section, the Position Sensitive Detector (PSD) plots are shown. This kind of monitor reveals every neutron that passes through the detector plane and show

in which position of the plane they have passed. Thanks to these monitors one can understand how guides affect the spatial distribution of the beam, see Fig. 9.3. In these simulations we assume the beam directed towards the Z axis and incoming on the monitor, the monitor width is parallel with the X axis and the height is parallel with the Y axis. The data regarding the actual TOSCA spatial profile are shown in Section 6.2.3 of this thesis. Due to the symmetrical geometry of the guide in form of a squared cross section, there are not privileged directions of reflections and as a consequence all the results show a perfect spatial symmetry about the central position. The presence or not of the guide $g1$ in the configuration does not have noticeable effects on the spatial distribution of the beam.

PSD monitor specifics: range X [-5, 5] cm, range Y [-5, 5] cm, number of pixels 500 x 500, at 17 m from the moderator.
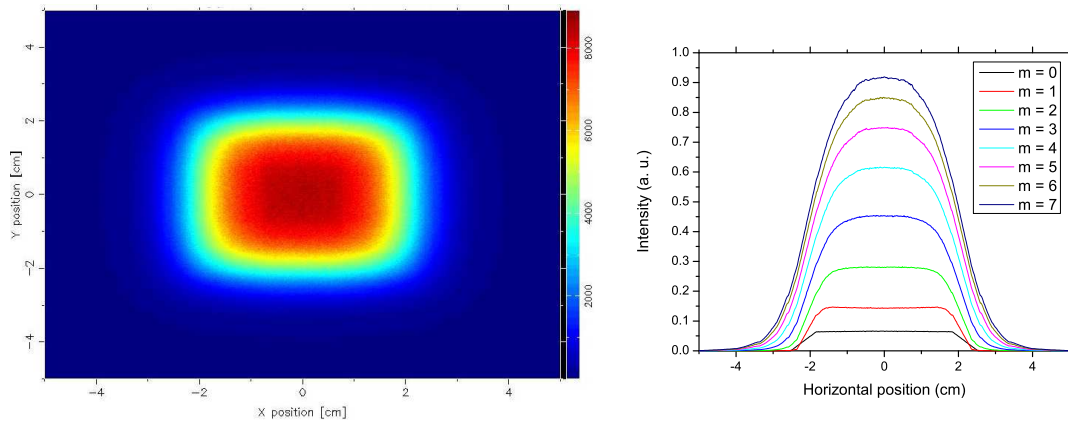
Figure 9.3. – Beam spatial profile at TOSCA sample position with a neutron guide along the N8 beamline. XY profile with the [5555505566667] configuration (left) and linear PSD profile with different guide configurations (right). The section $g1$ is simulated in all cases.

9.3.2. Divergence profile

The beam divergence is related to the direction of the neutrons that pass through the XY plane. It is expressed as degrees of divergence from the normal direction to that plane, along both the X and Y axis. This factor affects the average direction in which neutrons hit the sample area. In the actual configuration of a beamline entirely composed of collimators, the divergence would reach a minimum. In fact they absorb every neutron that emerges from the moderator with a direction that cannot intercept the sample plane. This reduces the overall divergence of the incoming beam. Installing guides on the beamline instead causes collection of more neutrons thanks to the particles reflection upon the guide walls, which allows neutrons that have unsuitable native direction to be guided towards the sample area. The increased flux comes at a cost of having a larger divergence of the incoming beam, due to the scattering that happens along the guide. The divergence of the beam increases as the length and reflectivity factor of the guide increase. Moreover, the divergence may

be higher for tapered guides compared to straight guides. The data regarding the actual TOSCA divergence profile are shown in Section 6.2.4 of this thesis. From the calculation results it emerges that the divergence raises up to $|0.4|°$ due to the guide, see Fig. 9.4. One can also notice a squared pattern in the calculations which do not include the shutter guide insert, which leads to inhomogeneities in the divergence profile, see Fig. 9.5. This issue is strongly reduced when the guide inside the shutter is simulated, see Fig. 9.4. In fact a guide within the very first section of the beamline seems to keep the divergence uniform across the sample.

Divergence monitor specifics: range along X [-1, 1] deg, range along Y [-1, 1] deg, number of pixels 500 x 500, dimensions 4 x 4 cm^2, placed at 17 m from the moderator.
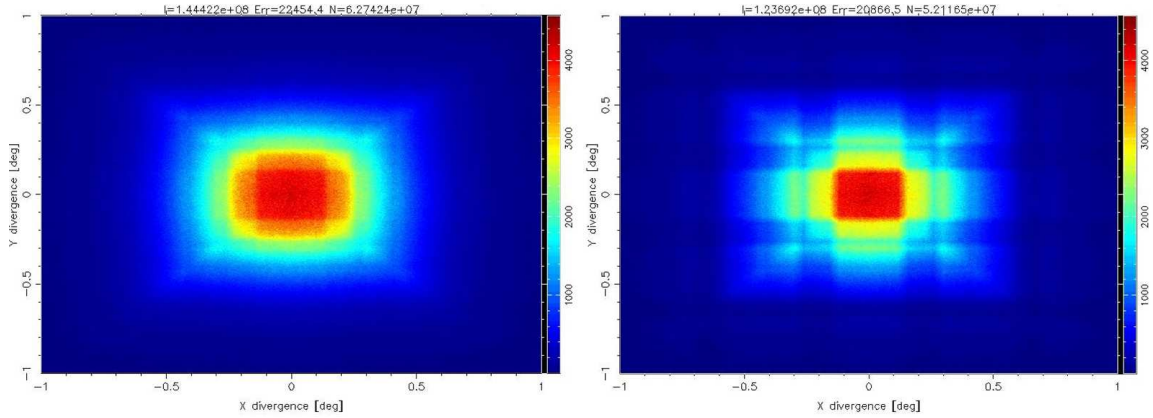
Figure 9.4. – TOSCA divergence profile at the sample position with the m = 3 guide configuration. The guide $g1$ was simulated (left) and excluded (right).
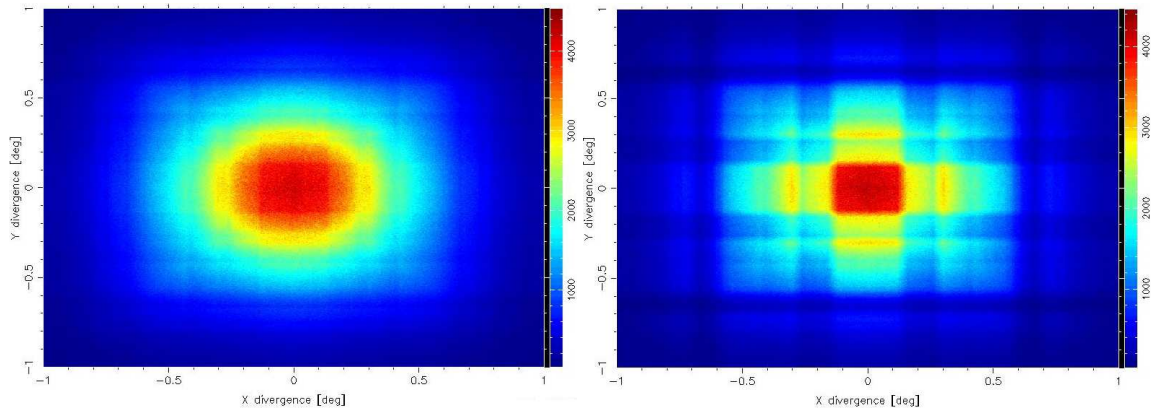
Figure 9.5. – TOSCA divergence profile at the sample position for the [555550556667] optimal guide configuration (left) and the [055550556667] configuration (right).

9.3.3. Wavelength spectrum

After the spatial and divergence analysis of the beam, we proceeded to study the wavelength spectrum of the neutrons crossing the sample position Fig. 9.6. It is

interesting to evaluate how the spectrum changes and the flux increases as the collimators within the TOSCA beamline are replaced with a neutron guide. It is worth to notice that the wavelength spectrum is equivalent to the TOF spectrum because the two units are linearly proportional.
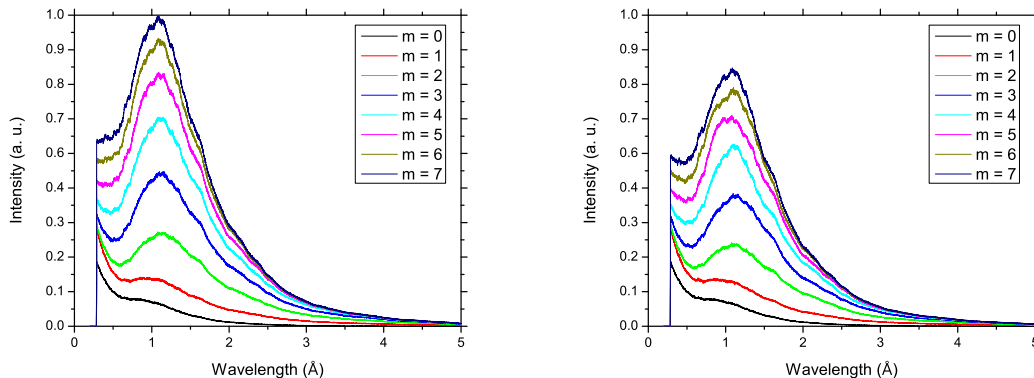
Figure 9.6. – TOSCA wavelength spectra at the sample position for different m factors of the guide, each configuration has the same m factor all along the guide. The guide inside the shutter is simulated for the curves on the left while on the right it is not.

9.3.4. Time-of-Flight calculations

The installation of a neutron guide along the beamline has not only the effect of selecting lower wavelengths, in fact it introduces a delay in the Time-of-Flight of the neutrons along the path between the moderator and the sample. This delay is due to the reflections some neutrons undergo on the guide's internal walls. Thus part of the neutrons inside the guide follow the path which is not straight, i.e. the TOF increases. The delay can be complex to evaluate because it is necessary to know the velocity vector of each neutron in the starting position and to consider every reflection, which is exactly why Monte Carlo simulations are suitable for this analysis. The Time-of-Flight delay introduced by the neutron guide is not analyzed in detail in this thesis but it might be done as a further development. McStas simulations could define an average delay in different energy ranges. It is plausible to expect the delay to be negligible for high energy neutrons (short TOF) which are much less likely to undergo reflections, and to be important for low energy neutrons (long TOF).

9.3.5. Neutron flux gain

The most intensive analysis was performed in simulating the flux gain at the sample position as a function of different configurations of the neutron guide. In fact, in each simulation the neutron flux was simulated using a different combination of m factors

along the beamline. The ultimate aim was to find an optimum configuration which maximizes the gain while keeping the cost acceptable. Furthermore, the gain analysis was performed in different energy ranges. The gain was calculated by evaluating the ratios between the neutron flux in the particular energy range by an energy monitor for both the model with and without a guide installed. The highest absolute gains are observed around 1 Å, approaching an order-of-magnitude enhancement in flux for the highest m-numbers investigated. We also note a monotonic (and quite significant) increase in flux up to $m \simeq 5-6$, values which are well within reach owing to advances in neutron-guide technology over the past decade. In relative terms, the largest gains are observed at the longest wavelengths, with factors exceeding 50 around the elastic line of the instrument at ca. 5 Å. The energy transfers accessible in this neutron-wavelength range correspond to the hard-to-access THz range in optical spectroscopy (1 $THz = 33.3\ cm^{-1}$), as well as provide much-needed overlap with the higher-resolution instruments IRIS [27] and OSIRIS [28] at ISIS. These two instruments have demonstrated an unrivalled energy resolution up to energy transfers of ca. 20 meV [7, 13], and could very well complement the broadband capabilities afforded by TOSCA at shorter wavelengths. The above flux gains in the THz window drop relatively quickly with decreasing wavelength to values of 2 - 3 at 0.5 Å. We also find that a progressive increase in m-number across the primary spectrometer tends to provide a more balanced gain across the spectral range of the instrument. Likewise, the net transport of high incident wavelengths (4 - 5 Å) can be maximised by having a guide insert inside the shutter assembly, as close as possible to the moderator face as present space constraints on ISIS TS-1 can allow. A high m-number closer to the sample can also increase the flux gain at the sample by factors of 2 - 3 for the shorter wavelengths ca. 1 Å.

Energy monitor specifics: dimensions 4 x 4 cm^2 at 17 m from the moderator, energy sampling step $\sim 200\ \mu eV$.

			GAIN IN DIFFERENT SPECTRAL RANGES							
					TOSCA MAIN RANGE					
			8 – 16	10 – 60	80 – 400	400 – 810	810 – 1610	1610 – 4030	4030 – 8070	[cm⁻¹]
			9.85 – 6.40	0.40 – 2.00	2.86 – 1.28	1.28 – 0.91	0.91 – 0.64	0.64 – 0.41	0.41 – 0.29	[Å]
Configuration	Mean gain	Max gain	1 – 2	2 – 10	10 – 50	60 –100	100 – 200	200 – 500	500 - 1000	[meV]
033 3303 333333	2.90	42.6	35.9	22.3	10.21	5.50	3.58	2.64	1.81	
333 3303 333333	3.23	58.7	48.3	28.3	12.27	8.46	4.07	2.90	1.86	
044 4404 444444	3.60	43.2	37.3	26.0	12.98	7.57	4.81	3.44	2.09	
444 4404 444444	4.11	59.3	51.0	33.7	15.99	8.79	5.63	3.89	2.20	
055 5505 555555	4.26	43.0	37.4	27.5	15.14	8.97	6.05	4.23	2.42	
555 5505 555555	4.93	59.9	51.5	35.9	18.69	10.71	7.00	4.85	2.61	
066 6606 666666	4.81	43.3	37.5	28.1	16.46	10.03	7.03	4.93	2.76	
666 6606 666666	5.61	59.6	51.5	36.8	20.40	12.14	8.15	5.69	3.03	
077 7707 777777	5.25	43.2	37.5	28.2	17.14	10.92	7.64	5.47	3.05	
777 7707 777777	6.15	60.3	51.6	37.0	21.36	13.13	8.98	6.34	3.40	
033 3303 344446	3.50	43.1	37.4	26.6	13.38	7.71	4.73	3.24	1.97	
333 3303 344446	3.91	60.1	51.5	34.6	16.47	8.93	5.30	3.52	2.03	
033 3303 355556	3.98	43.1	37.5	27.8	15.25	9.04	5.88	3.86	2.14	
333 3303 355556	4.44	60.0	51.5	36.5	18.78	10.41	6.52	4.17	2.19	
033 3303 066666	4.37	42.8	37.5	28.0	15.98	9.62	6.81	4.46	2.32	
333 3303 066666	4.84	59.7	51.5	36.7	19.66	11.04	7.49	4.79	2.38	
033 3306 666666	4.42	43.2	37.5	28.1	16.12	9.65	6.90	4.53	2.35	
333 3306 666666	4.90	59.4	51.4	36.8	19.83	11.07	7.57	4.86	2.41	
044 4404 444445	3.64	43.0	37.4	26.6	13.26	7.65	4.86	3.46	2.09	
444 4404 444445	4.15	59.7	51.3	34.6	16.33	8.90	5.68	3.92	2.21	
044 4404 444446	3.66	43.6	37.5	26.6	13.38	7.74	4.89	3.49	2.10	
444 4404 444446	4.18	60.0	51.4	34.6	16.49	8.99	5.73	3.94	2.21	
044 4404 455556	4.16	42.7	37.5	27.9	15.36	9.06	6.07	4.13	2.27	
444 4404 455556	4.75	59.7	51.5	36.5	19.00	10.82	7.00	4.63	2.39	
044 4405 555555	4.15	43.2	37.5	27.5	15.14	8.97	6.05	4.13	2.28	
444 4405 555555	4.73	60.0	51.4	35.9	18.69	10.71	6.96	4.62	2.40	
044 4405 555556	4.17	42.9	37.5	27.9	15.36	9.07	6.09	4.16	2.28	
444 4405 555556	4.76	59.9	51.5	36.5	18.99	10.81	7.01	4.65	2.40	
055 5505 566666	4.73	43.1	37.5	28.1	16.46	10.03	7.03	4.88	2.62	
555 5505 566666	5.46	59.8	51.4	36.8	20.39	12.14	8.15	5.57	2.82	
055 5505 566667	4.75	43.4	37.5	28.2	16.61	10.12	7.07	4.90	2.63	
555 5505 566667	5.50	60.4	51.5	37.0	20.61	12.24	8.20	5.60	2.83	
055 5506 666666	4.74	43.0	37.5	28.1	16.45	10.03	7.03	4.90	2.64	
555 5506 666666	5.48	59.6	51.5	36.8	20.40	12.14	8.15	5.59	2.83	
055 5506 666667	4.77	43.1	37.5	28.2	16.60	10.12	7.07	4.92	2.65	
555 5506 666667	5.51	59.7	51.6	37.0	20.62	12.24	8.20	5.62	2.84	
066 6606 677777	5.24	42.8	37.5	28.3	17.14	10.92	7.64	5.47	3.04	
666 6606 677777	6.06	59.7	51.4	37.0	21.36	13.14	8.98	6.31	3.25	
066 6607 777777	5.25	43.1	37.5	28.2	17.14	10.92	7.64	5.47	3.05	
666 6607 777777	6.07	59.7	51.5	37.1	21.36	13.14	8.98	6.32	3.26	

Table 9.2. – Calculated gain for the neutron guide simulated on the N8 beamline. The gain is presented over all energy as well as across particular energy ranges. The main range of interest for TOSCA is 10 - 200 meV. Notice that the guide g6 (vacuum valve insertion) has m = 0.
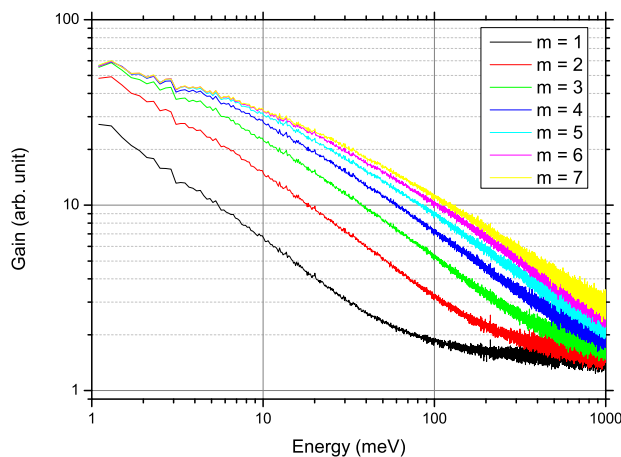
Figure 9.7. – Calculated gain for the neutron guide simulated on the TOSCA beamline. The gain is presented as a function of energy for different m factors of the guide. Notice that the guide section g6 (vacuum valve insertion) has $m = 0$ in each configuration. Energy monitor specifics: dimensions 4 x 4 cm^2 at 17 m from the moderator, energy sampling step $\sim 200 \, \mu eV$.

9.3.6. Effect on the resolution

As evidenced by the experiments presented in Chapter 8, the actual configuration of TOSCA inelastic neutron scattering spectrometer has an average experimental resolution of $\sim 7.78\,\%$ at the elastic line. In the following simulations, the effect of the neutron guide on the TOSCA INS resolution was calculated. Four interesting configurations of the guide were considered to study the variations in the elastic back-scattering and forward-scattering signals from water ice kept at 10 K. It is important to evaluate any variations in the energy transfer position and the FWHM of the elastic peak with a neutron guide along the primary spectrometer, in order to foresee the impact that the guide has on the instrument resolution and on the overall INS measurements. In Fig. 9.8 and Tab. 9.3 one can see the calculations about the elastic line for the back-scattering spectrometer. In Tab. 9.4 the calculations about the forward-scattering spectrometer are shown. All the curves were fitted using the Gaussian function to assess the parameters. From these results is evinced that the spectral resolution of the instrument around the elastic line is largely insensitive to a rather substantial increase in the m-number of the guide in the primary spectrometer. These results are to be taken as the worst-case scenario (long wavelength and high m), given the linear dependence of beam divergence on both incident wavelength and m-number. We therefore conclude that the predicted gains reported in Tab. 9.2 and Fig. 9.7 are not accompanied by a concomitant degradation of the spectroscopic capabilities presently afforded by TOSCA.
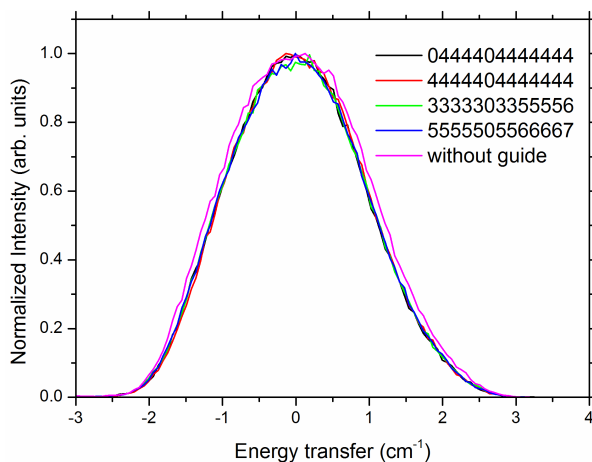
Figure 9.8. – Calculated back-scattering elastic line. The curves refer to different configurations of the guide and the current configuration without a guide. The numbers in the legend denote the m-value for each independent section along the primary spectrometer, starting closest to the moderator face.

Configuration	Peak center (meV)	FWHM (meV)	TOF FWHM (μs)	Fit: reduced χ^2	Resolution %
0444404444444	-0.100 ± 0.001	0.275 ± 0.001	749	10^{-7}	7.24
4444404444444	-0.098 ± 0.0005	0.275 ± 0.001	749	10^{-7}	7.24
3333303355556	-0.099 ± 0.001	0.279 ± 0.001	760	10^{-7}	7.34
5555505566667	-0.099 ± 0.0005	0.279 ± 0.001	760	10^{-7}	7.34

Table 9.3. – Back-scattering calculations of the TOSCA INS spectrometer at the elastic line, considering different configuration of the neutron guide along the beamline. The numbers in the first column denote the m-value for each independent section along the primary spectrometer, starting closest to the moderator face. The energies are intended as energy transfer from the 3.8 meV elastic line, the resolution is calculated in reference to this value.

Configuration	Peak center (meV)	FWHM (meV)	TOF FWHM (μs)	Fit: reduced χ^2	Resolution %
0444404444444	-0.105 ± 0.001	0.278 ± 0.001	757	10^{-7}	7.32
4444404444444	-0.104 ± 0.001	0.277 ± 0.001	754	10^{-7}	7.30
3333303355556	-0.104 ± 0.001	0.279 ± 0.001	760	10^{-7}	7.34
5555505566667	-0.104 ± 0.0005	0.279 ± 0.001	760	10^{-7}	7.34

Table 9.4. – Forward-scattering calculations of the TOSCA INS spectrometer at the elastic line, considering different configuration of the neutron guide along the beamline. The numbers in the first column denote the m-value for each independent section along the primary spectrometer, starting closest to the moderator face. The energies are intended as energy transfer from the 3.8 meV elastic line, the resolution is calculated in reference to this value.

9.3.7. Optimal configuration

Section	g1	g2	g3	g4	g5	g6	g7	g8	g9	g10	g11	g12	g13
coating m value	5	5	5	5	5	0	5	5	6	6	6	6	7

Table 9.5. – m-factor configuration of the optimal neutron guide proposed by the Molecular Spectroscopy Group at ISIS.

The extensive simulations presented earlier were performed to assess the relative performance of a total of forty different guide configurations and the m-factor configuration considered by the ISIS Molecular Spectroscopy Group as the most promising in terms of cost and benefits is presented in Tab. 9.5. Apart from the gain and cost, some other guide performances which lead to the choice of this particular geometry are presented in Section 9.4. The spatial profile related to this optimal configuration was presented in Fig. 9.3 and in Fig. 9.5 its divergence profile was shown. The gain curve associated with this configuration is shown in Fig. 9.9, while for completeness the curve regarding the configuration without the shutter guide is plotted. The associated gain values are reported in Tab. 9.2, this configuration achieves a good gain in the energy range of interest for TOSCA. The average m-factor of this configuration is 5.45, thus considering that state-of-the-art guides can reach $m = 7$, the proposed configuration may represent an optimum balance between the gain and cost. The predicted gains for this configuration are 52 for the lowest incident wavelength and 3 for the highest available on the instrument. Use of a high-m guide ($m > 4$) close to the source ensures reasonable gain factors even at moderately high energy transfers above 100 cm^{-1}.
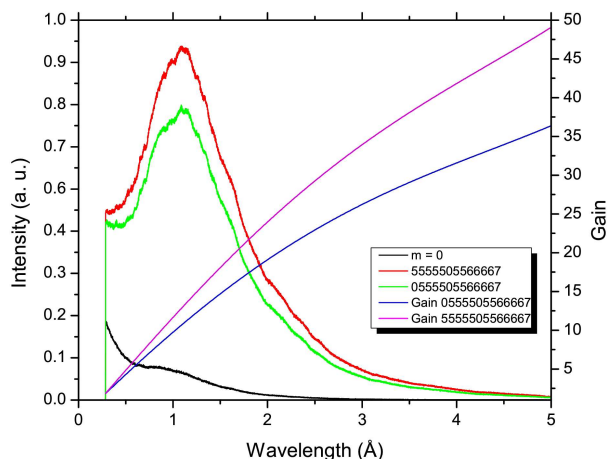

Figure 9.9. – Wavelength spectrum and related gain at TOSCA sample position for the optimal guide configuration (shown in legend), the configuration without $g1$ is included as well. The actual beamline configuration ($m = 0$) is plotted as a term of comparison.

9.4. Complementary analysis

In addition to the analysis of the gain obtained ny varying the configuration of m factors, further aspects that could influence the final gain were investigated. Some of these aspects are the overall geometry of the guide, the position of the sections with higher m factor and potential misalignment between the sections.

9.4.1. Test of the geometry

As explained by J. Castañon in his report [5], the simulated neutron guide on TOSCA gives a greater gain in the tapered geometry rather than rectilinear geometry. The configuration of the TOSCA guide presented in [5] was used in this thesis for the initial test simulations. Subsequently, thanks to the kind collaboration of the ISIS Engineering Group a new geometric configuration was conceived. The choice remained on a tapering guide but with different values of the apertures and a slight extension of the overall length. This latest geometry has been presented in Tab. 9.1 and it was assumed as definitive for the flux gain simulations. Tab. 9.6 shows the comparison between the gain obtained by simulating the geometry discussed in [5] and the geometry agreed with the Engineering Group. For the m factors of interest, the utilization of the latest geometry defines a substantial increase in the gain in nearly the whole of the spectrum.

Energy range (meV)	$1-2$	$2-10$	$10-50$	50 - 100	$100-200$	$200-500$
M = 3 test	50.4	24.9	8.7	4.3	2.7	1.6
M = 3 final	48.3	28.3	12.3	6.5	4.1	2.9
Ratio %	-4.3	11.9	29.1	33.4	33.7	44.8
M = 4 test	55.0	30.9	11.6	6.0	3.8	2.2
M = 4 final	51.0	33.7	16.0	8.8	5.6	3.9
Ratio %	-7.8	8.4	27.2	31.4	33.0	44.4
M = 5 test	55.7	33.8	14.0	7.4	4.8	2.7
M = 5 final	51.5	35.9	18.7	10.7	7.0	4.8
Ratio %	-8.2	5.7	25.1	31.3	32.1	43.5
M = 6 test	55.7	35.2	15.6	8.4	5.6	3.3
M = 6 final	51.5	36.8	20.4	12.1	8.2	5.7
Ratio %	-8.1	4.5	23.4	30.8	31.8	42.7
M = 7 test	55.6	35.6	16.6	9.3	6.1	3.7
M = 7 final	51.6	37.0	21.4	13.1	9.0	6.3
Ratio %	-7.8	3.9	22.4	29.5	31.7	41.7

Table 9.6. – Comparison between the gain achieved using the *test* guide presented in [5] and the *final* guide geometry in different configurations.

9.4.2. M factors disposition along the beamline

Simulations were performed with particular configurations of m factors in order to assess whether it was more effective to have increasing or decreasing m factors along the guide, from the moderator to the sample. At low energy (1 - 4 meV) the contribution due to the presence of the guide inside the shutter dominates, while for higher energy (4 - 300 meV) the contribution due to the presence of higher m factors close to the sample appears to be important. Overall, in the TOSCA energy range the gain is higher in the configurations that have an increasing disposition of m factors towards the sample. Furthermore, the use of an increasing disposition gives a better performance across the TOSCA energy range also compared to a configuration with a unique m value for every section, as presented in Tab. 9.2.

9.4.3. Extending the guide

Simulations were performed considering an ideal (thus difficult to build) guide which starts 1 cm far from the aperture of the moderator up to 1 cm before the sample position to evaluate potential improvements for the gain. It was decided to simulate a guide with the maximum practicable m factor ($m = 7$) and to consider the guide extension alternatively at the beginning of the guide or at the end, and a guide with both extensions. The extensions are pieces of rectilinear guide with $m = 7$. The results shown in Fig. 9.10 explain that the gain in this ideal geometry is considerable until 100 meV compared to the unextended geometry and it seems possible to obtain G > 100 at low energies. As presented in Tab. 9.7, the configurations that reach higher gain have the final extension that comes close to the sample. Instead, the presence of an initial extension that begins near the aperture of the moderator introduces only small improvements with respect to the unextended geometry.

Energy range (meV)	$1-2$	$2-10$	$10-50$	50 - 100	$100-200$	$200-500$
Unextended guide	51.6	37.0	21.4	13.13	8.980	6.343
Extended to moderator	53.2	37.7	21.5	13.14	8.982	6.343
Extended to sample	116	61.7	27.7	15.22	9.891	6.839
Both extensions	125	63.9	28.0	15.23	9.899	6.840

Table 9.7. – Gain values in different energy ranges, taking into account extensions of the neutron guide.

9.4.4. Simulation of a misalignment of the shutter

This simulation is intended to evaluate the effect of a guide inside the shutter ($g1$) in the case where the shutter undergoes a horizontal misalignment with respect to the following section. Such event is likely because the mechanism of insertion and
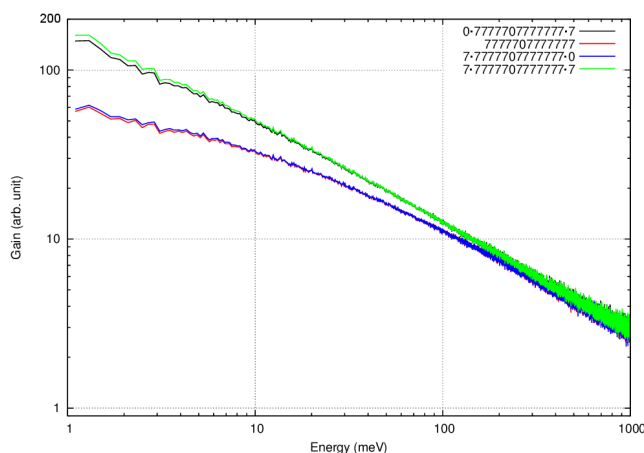
Figure 9.10. – Gain as a function of neutron energy for simulation of the configuration m = 7 and simulation of its extensions by supplementary sections of guide at the beginning and/or at its end.

removal of the shutter from the beamline is a screw mechanism which acts along the vertical axis. This may cause a slight deviation around the vertical axis of the neutron tube inside the shutter when it is in the open position. According to the evaluation of ISIS Engineering Group, the horizontal misalignment of the opened shutter due to the screw mechanism stays within ± 1 cm relative to the following neutron tube. Any misalignment of the remaining sections of the guide is considered unlikely. First consider the current configuration of TOSCA (i.e. without guides) in which the shutter is misaligned, simulations showed there is a reduction of the solid angle subtended from the moderator to the sample position and this causes a slight decrease of the neutron flux on the sample. The gain in this case is equal to 0.88 and is evenly spread across the spectrum. This corresponds to a variation of -12 % in the neutron flux for the entire energy range of interest.

The configuration with a $m = 7$ guide without $g1$ was also considered. Simulations show an overall decrease of the neutron flux due to shutter misalignment compared to the same configuration with a shutter properly aligned. The variation ranges between -5.9 % and -6.4 % over all energies. Consider at last the configurations that have a guide inside the shutter, Fig. 9.11 shows the gain curves regarding m = 3 and $m = 7$ guide in the case where the shutter is misaligned. In this plot, the curves relating to the shutter properly aligned are also shown for comparison. The spatial distribution of the neutron beam was also simulated; it appears that the misalignment of the guide section $g1$ does not cause appreciable inhomogeneity of the beam profile on TOSCA sample, while the distribution of the neutron flux on the INES sample position appears inhomogeneous, see Fig. 9.12. This may be due to the greater distance from the moderator to INES with respect to TOSCA, which makes INES more prone to anomalies in the distribution of the beam.
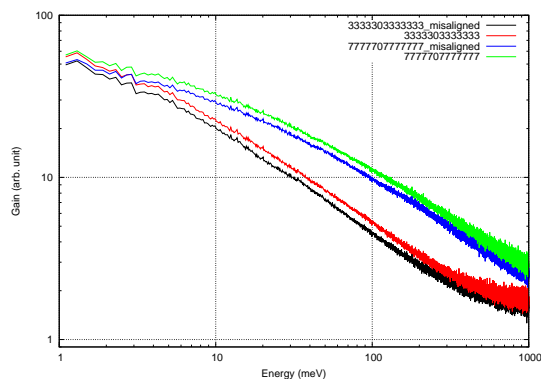
Figure 9.11. – Gain as a function of neutron energy for simulation of m = 3 and m = 7 guide. Each configuration is presented in both the case with the shutter aligned and misaligned.
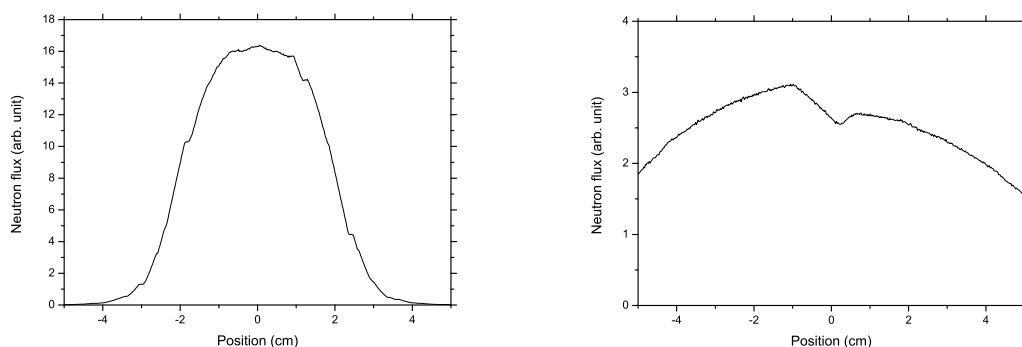

Figure 9.12. – Simulated beam profiles for the m = 7 guide with section $g1$ misplaced. At TOSCA (left) and INES (right) sample position.

9.4.5. Effects of the neutron guide on INES

INES [26] is a general purpose diffractometer, mainly devoted to material characterization (structure refinement and phase analysis), cultural heritage studies and equipment tests. The instrument takes the transmitted beam from TOSCA spectrometer sample position and thus one has to consider how possible modifications on the TOSCA beamline affect the neutron signal received on INES sample position. For this reason, we present the McStas simulation results which show the effects of a neutron guide on the incident neutron beam at INES sample position, placed at 22.8 m from the moderator. The data are presented in both configurations, with and without the $g1$ guide section inside the shutter. In Fig. 9.13 one can see the calculations for the optimal configuration and the related gain. As expected, the flux gain due to the guide is higher over all spectrum if the shutter guide is installed. It appears also that a neutron guide inside the shutter varies the spatial characteristics of the beam in a non-negligible way. The INES beam profile results well centered and focused on a size of 40 x 40 mm^2, while the penumbra extends up to an area of 80 x 80 mm^2, see Fig. 9.14. On the other hand, one can notice that

in the simulations where the guide $g1$ is in place the beam profile on INES appears homogeneous, while when $g1$ is not installed the spatial spread of the beam does not change but a peculiar pattern appears, see Fig. 9.15. The spatial neutron intensity at INES sample position is measured by 2-D detector along the XY plane and by a linear position sensitive detector (linear PSD) at the sample plane which averages the neutron intensities along the vertical axis. The latter detector is suitable in this case because the beam profile shows a central symmetry.
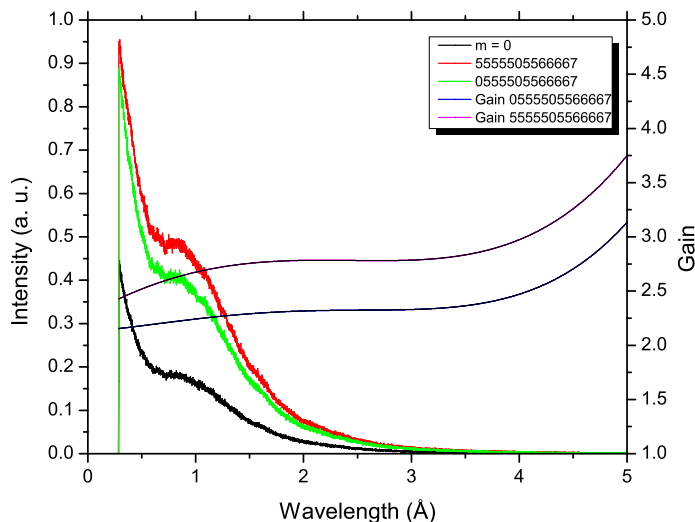
Figure 9.13. – Wavelength spectrum and related gain at INES sample position for the optimal guide configuration (shown in legend); the configuration without $g1$ is included as well. The actual beamline configuration (m = 0) is plotted for comparison.

After the installation of the neutron guide, the beam divergence is still relatively low on INES, i.e. the maximum deviation of the beam for these configurations remains below $|0.3|°$ including the penumbra. However, if the guide inside the shutter has not been included in simulation, a pattern appears as can be seen from the spatial profile. The pattern has central symmetry and points at that some angle values are less probable. This may be correlated with the squared geometry of the neutron guide. On the other hand, if the guide $g1$ is included in the simulation the divergence appears evenly distributed as shown in Fig. 9.16. At last, we calculated the wavelength spectrum at INES sample position with a neutron guide installed along the TOSCA beamline, see Fig. 9.17, different guide configurations were considered.
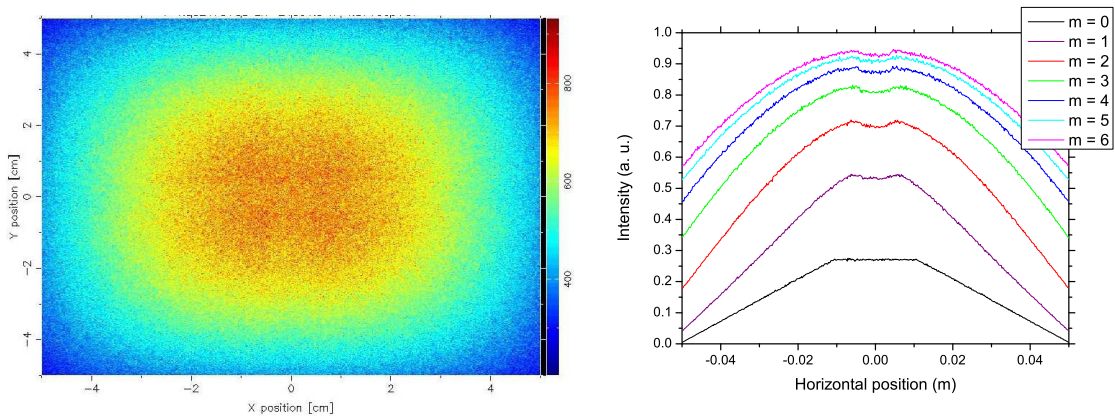
Figure 9.14. – Beam spatial profile at INES sample position with a neutron guide along the TOSCA beamline. XY profile with 5555505566667 configuration (left) and linear PSD in different guide configurations (right). In all cases the section $g1$ has been included in simulations, as well.
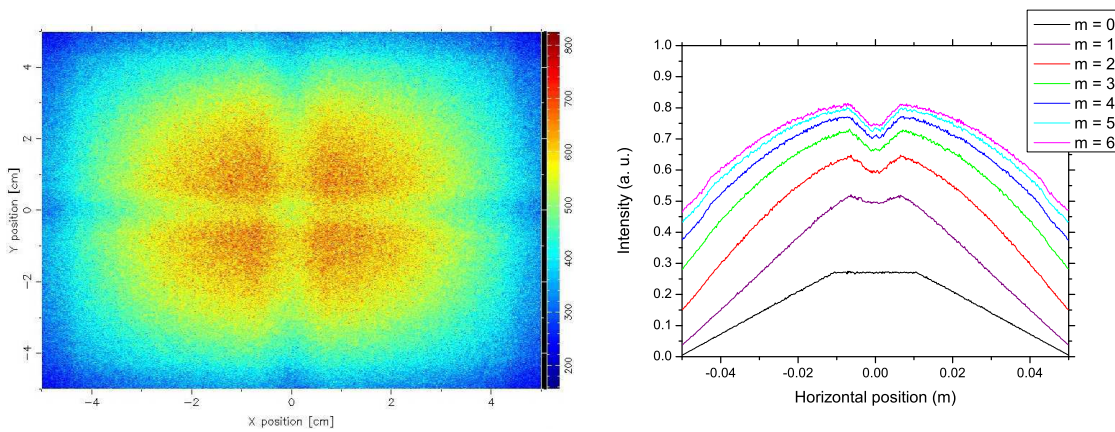
Figure 9.15. – Beam spatial profile at INES sample position with a neutron guide along the TOSCA beamline. XY profile with 0555505566667 configuration (left) and linear PSD in different guide configurations (right). In all cases the section $g1$ has not been included in simulations.
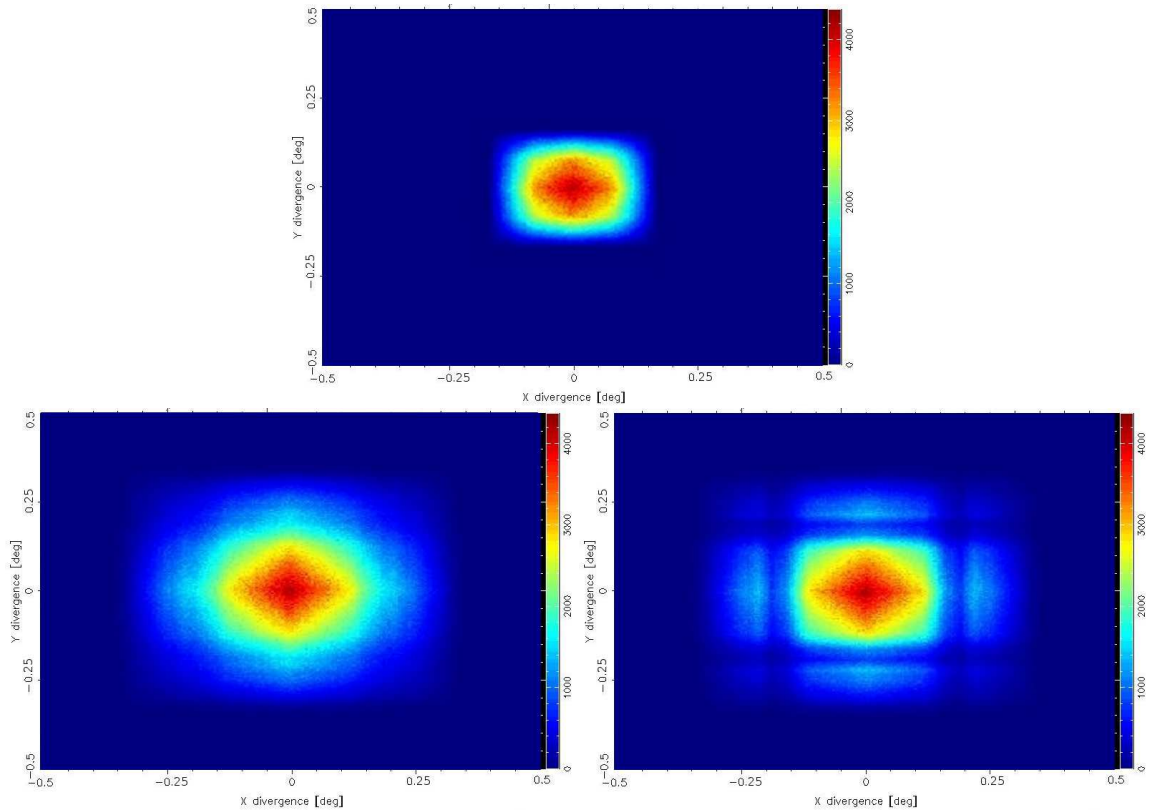
Figure 9.16. – Calculations of the divergence profile of the beam at INES sample position. The simulated configurations of the TOSCA beamline are: without the guide (top), with 5555505566667 guide (bottom left) and 0555505566667 (bottom right).
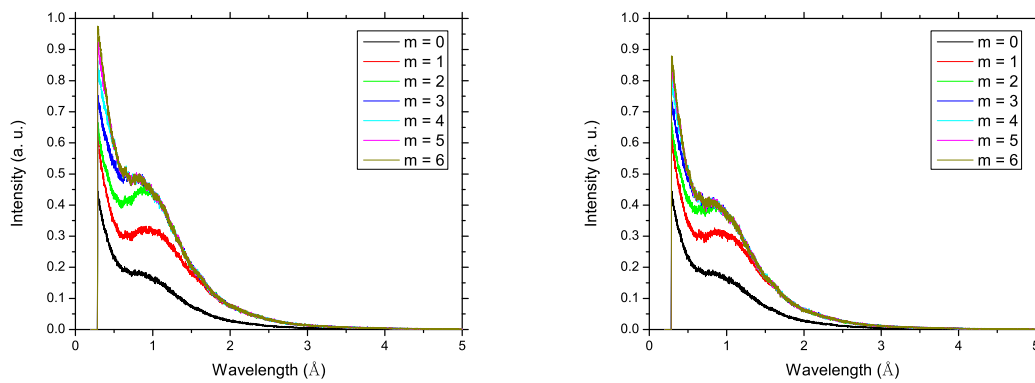
Figure 9.17. – Wavelength spectrum at INES sample position. Different configurations of the guide are presented. The guide section $g1$ is simulated (left) and excluded (right). The actual beamline configuration (m = 0) is plotted as a term of comparison.

10. Conclusions and outlook

Given the results achieved in this thesis we can confirm that Monte Carlo simulations of the TOSCA spectrometer using the McStas software package provide a satisfactory description of the current performance of the instrument in terms of incident-flux spectra, associated time structure and spectroscopic response. Encouraged by these success, we have also assessed potential flux gains associated with the installation of a neutron guide in the primary spectrometer. Unlike a decade ago when the instrument became operational, judicious use of state-of-the-art guide technology to upgrade the primary spectrometer offers the exciting prospects of providing order-of-magnitude gains in sensitivity whilst preserving the outstanding spectroscopic capabilities of the instrument. In this section, we considered important to briefly outline the achievements of the present work and its future applications.

The first analysis performed in this project regards a comparison between experimental and simulated incident neutron spectra at the position of the primary monitor. This monitor is located upstream from the sample position at 15.795 m from the room-temperature water moderator. Experimental raw data have been corrected by the measured wavelength-dependent efficiency of this lithium-glass scintillator detector over the incident-wavelength range of the instrument (0.3-5.0 Å). Simulated spectra were calculated using the ISIS Target Station I water-moderator module released in 2007. Overall, the Monte Carlo calculations provide a satisfactory description of the experimental incident spectrum, although some differences are to be noted in terms of the extent of the moderation peak, which appears to be more pronounced in the simulated dataset. These differences are of the order of 20-25% around the fingerprint region of vibrational spectra (10-125 meV; i.e. 0.8-2.9 Å). Notwithstanding the above differences, both experimental and simulated data evince an epithermal-looking incident spectrum. These discrepancies have a minor effect on reduced inelastic neutron spectra, as these are always normalised to the incident neutron-flux distribution prior to subsequent analysis.

In addition to incident neutron spectra, the performance of an inverted-geometry instrument like TOSCA critically depends on the time structure of neutron pulses reaching the sample position. Experimental access to this information is facilitated by the availability of a high-resolution diffraction bank in backscattering geometry. In this configuration, the observed time widths of well-defined Bragg reflections become most sensitive to the temporal spread of neutron pulses arriving at the sample position. For this thesis, measurements at a temperature of 10 K were performed on a 30×40×2 mm3 highly oriented pyrolytic graphite (HOPG) standard with a mosaicity of 0.8±0.2° along the c-axis. This standard was aligned with the a-b plane

perpendicular to the incident beam and its c-axis rotated so as to maximise (00l) Bragg intensities on detector 147, located at a distance of 1.21 m from the sample position at a scattering angle of 178.28°. For comparison, an identical experimental setup was implemented in McStas. The wavelength dependence of time widths associated with (00l) HOPG Bragg reflections are obtained from least-squares fits of both experimental and simulated data. In both cases, the widths are dominated by the temporal response of the primary spectrometer and the time structure emerging from the moderator face. Other contributions associated with time uncertainties between the moderator and the sample are relatively minor in comparison. The agreement between experiment and simulation is quite satisfactory, particularly in terms of an overall increase in FWHM with neutron wavelength in the thermal and cold regimes. At the longest wavelength investigated (3.33 Å), simulations are within 10-15% of experimental values, and consistently provide a safe lower bound to observation. These results are also in agreement with a moderator term of ~12 μs/Å inferred from previous calibrations of TOSCA. On the basis of the present comparison, this moderator term provides a good description of time structure below ca. 3 Å. At the higher wavelength investigated, the time width shows signs of saturation, as expected for the moderation of cold neutrons at a short-pulse spallation source. These results also highlight the good diffraction capabilities with excellent resolution ($\Delta d/d \sim 5 \times 10^{-3}$ over its operating wavelength range).

The above comparisons between experimental and simulated performance were primarily concerned with a characterisation of the primary spectrometer. To assess the validity of our current description of the entire instrument, we have also compared experimental and simulated spectra around the elastic line for ice at a temperature of 10 K. For the purposes of benchmarking the McStas simulations, this case represents a convenient scenario characterised by high scattering levels (potentially leading to an increase in instrumental backgrounds), as well as comparable contributions to the resolution function from both primary (moderator) and secondary spectrometers (inelastic banks). The agreement between experiment (FWHM = 0.3 meV) and simulation (0.29 meV) is excellent aside from a slight excess in scattered intensity for neutron-energy gain processes. Elucidating the precise origin of this second-order feature in the observed spectrum is beyond the scope of the present work. Overall, these results further confirm the adequacy of our computational model for a quantitative description of the spectroscopic response of the instrument in its present incarnation.

To assess possible gain factors relative to current capabilities, extensive McStas simulations have been performed for a range of guide configurations using realistic reflectivity profiles. A tapered guide represents the most sensible geometry to transmit neutrons over a wide wavelength range. Such a guide can be placed at a minimum distance from the moderator of 1.625 m with a cross sectional area of 10×10 cm^2 followed by thirteen independent sections ending at a distance of 0.75 m from the sample position (4×4 cm^2). It is expected that the flux at the sample position would increase as a function of guide m-number. The highest absolute gains are observed around 1 Å, approaching an order-of-magnitude enhancement in

flux for the highest m-numbers investigated. We also note a monotonic (and quite significant) increase in flux up to $m\sim$5-6, values which are well within reach owing to advances in neutron-guide technology over the past decade. In relative terms, the largest gains are observed at the longest wavelengths, with factors exceeding 50 around the elastic line of the instrument at ca. 5 Å. The energy transfers accessible in this neutron-wavelength range correspond to the hard-to-access THz range in optical spectroscopy, as well as provide much-needed overlap with the higher-resolution instruments IRIS and OSIRIS at ISIS. The above flux gains in the THz window drop relatively quickly with decreasing wavelength to values of 2-3 below 1 Å. We also find that a progressive increase in m-number across the primary spectrometer tends to provide a more balanced gain across the spectral range of the instrument. Likewise, the net transport of high incident wavelengths (4-5 Å) can be maximised by having a guide insert inside the shutter assembly, as close to the moderator face as present space constraints on ISIS Target Station I may allow. A high m-number closer to the sample can also increase the flux at the sample by factors of 2-3 for the shorter wavelengths. The performed simulations assessed the relative performance of a total of 40 different guide geometries and the configuration of choice corresponds to [5555505566667], where each single digit within square brackets denotes the m-value for each independent section along the primary spectrometer, starting closest to the moderator face. Predicted gains for this configuration are 52 and 3 for the highest and lowest incident wavelengths available on the instrument, respectively. Use of a high-m guide ($m>$4) close to the source ensures reasonable gain factors above 20 meV. As an additional test, we calculated that the spectral resolution of the instrument around the elastic line is insensitive to a rather substantial increase in the m-number of the guide in the primary spectrometer. These results are to be taken as a worst-case scenario (long λ, high m), given the linear dependence of beam divergence on both incident wavelength and m-number. We therefore conclude that the predicted gains are not accompanied by a degradation of the spectroscopic capabilities presently afforded by TOSCA.

On the scientific front, the much-needed upgrade of TOSCA beamline implies a concomitant reduction in counting times, a transformational development as it would enable detailed studies of industrially relevant systems exhibiting low scattering cross sections. To name a few, these include studies of molecular adsorbates such as CO, NO, or SO_2 on catalysts, where inelastic neutron scattering can uniquely provide information on the low-energy modes underpinning adsorbate-surface interactions; or of proton-conducting pathways in charge-storage materials containing minute amounts of hydrogen. Detailed parametric studies would become routine as well, particularly for hydrogen-containing systems such as polymers and nanostructured materials. Moreover, the (very popular) TOSCA Xpress service could also be expanded and automated beyond its current remit to provide an efficient outreach tool. In conjunction with ongoing efforts at ISIS to improve neutronic performance, the upgrade possibilities described herein will certainly keep TOSCA at the forefront of chemical spectroscopy with neutrons in the foreseeable future.

Acknowledgments

I would like to express my gratitude to my supervisor, Prof. Giuseppe Gorini, for the patient guidance he provided to me, all the way from when I was first considering applying to a thesis period abroad, through to completion of this degree. Sincere thanks to my ISIS supervisors, Svemir Rudic, Felix Fernandez-Alonso and Stewart Parker for the support, mentorship and training they provided throughout the project. They always made me feel appreciated and integrated with the research group, this gave me the strength to do my work at the best of my possibilities.

GRAZIE!!!

Ringrazio in primis la mia famiglia e i miei padrini per aver fatto numerosi sacrifici per farmi arrivare fino a questo punto, vi sono grato anche per il semplice fatto di esserci stati e avermi supportato in ogni momento della vita. Ringrazio anche me stesso per averci creduto sempre caparbiamente, nonostante il percorso fino a qui sia stato spesso in salita.
Un grazie e un abbraccio a Jacopo per essere da anni un'amicizia fraterna su cui posso contare e a Caterina per essermi stata vicina pazientemente in questo anno particolarmente difficile.

Infine voglio ricordare mio fratello, Cristian Pinna, che ha lasciato questo mondo un pomeriggio di agosto mentre io ero lontano da casa a scrivere questa tesi. A te dedico tutto questo mio lavoro, non dimenticherò mai quello che sei stato per me.
Io ti rincontrerò un giorno...ma non ancora.

A. McStas instrument models of TOSCA

A.1. Model of the actual TOSCA beamline

/* Created by: Roberto Simone Pinna, ISIS, RAL, 2014. */

DEFINE INSTRUMENT tosca(m_shutter = 0, m_monolith = 0, m_bef_vac = 0, m_lfp = 0, nu_chop = 0, phase_chop = 28, E_min = 1, E_max = 1000)

DECLARE %{ double v_foc, c_h1, c_h2, slit_curv, num_slits; double E_min, E_max; double m_shutter, m_monolith, m_bef_vac, m_lfp; double lam, deg_phase, phase_time; double phase; double monitor_dimx = 0.10; double monitor_dimy = 0.10; int resx = 500; int resy = 500; double Emon_min = 1; double Emon_max = 1000; double L_min = 0.2; double L_max = 5; double t_min = 1000; double t_max = 40000; double d_spacing = 3.354; double M_Mosaic = 150; minutes double reflect = 0.866; double DWidth = 0.250; double DHeight = 0.250; double tmin_back = 5000; double tmin_fwd = 5000; double tmax_back = 40000; double tmax_fwd = 40000; double emin_back = 0.1; double emin_fwd = 0.1; double emax_back = 50; double emax_fwd = 50; %}

TRACE

COMPONENT arm1 = Arm() AT (0,0,0) ABSOLUTE

//————————————MODERATOR

COMPONENT isis_moderator = ISIS_moderator(Face = "tosca", Emin = E_min, Emax = E_max, dist = 1.625, focus_xw = 0.12, focus_yh = 0.115, xwidth = 0.12, yheight = 0.115, CAngle = 0, SAC = 1) AT (0, 0, 0) RELATIVE arm1

//————————————SHUTTER

COMPONENT slit_tosca1 = Slit(xmin = -0.042, xmax = 0.042, ymin = -0.040, ymax = 0.040) AT (0, 0, 1.625) RELATIVE arm1

COMPONENT guide1 = Guide_channeled(w1 = 0.084, h1 = 0.080, w2 = 0.073, h2 = 0.074, l = 1.940, alphax = 4.38, alphay = 4.38 , W=3e-3, mx = m_shutter, my = m_shutter) AT (0, 0, 1.625) RELATIVE arm1

//————————————MONOLITH

COMPONENT gap1 = Guide_channeled(w1 = 0.073, h1 = 0.074, w2 = 0.0751, h2 = 0.0751, l = 0.130, alphax = 4.38, alphay = 4.38 , W=3e-3, mx = 0, my = 0) AT (0, 0, 3.565) RELATIVE arm1

COMPONENT guide2_1 = Guide_channeled(w1 = 0.0751, h1 = 0.0751, w2 = 0.069, h2 = 0.069, l = 2.345, alphax = 4.38, alphay = 4.38 , W=3e-3, mx = m_monolith, my = m_monolith) AT (0, 0, 3.695) RELATIVE arm1

//————————————UNTIL VACUUM VALVE

COMPONENT slit_tosca2 = Slit(xmin = -0.0342, xmax = 0.0342, ymin = -0.0342, ymax = 0.0342) AT (0, 0, 6.040) RELATIVE arm1

COMPONENT guide3_1 = Guide_channeled(w1 = 0.0684, h1 = 0.0684, w2 = 0.0611, h2 = 0.0611, l = 2.9545, alphax = 4.38, alphay = 4.38, W=3e-3, mx = m_bef_vac, my = m_bef_vac) AT (0, 0, 6.040) RELATIVE arm1

COMPONENT gap2 = Guide_channeled(w1 = 0.0611, h1 = 0.0611, w2 = 0.0611, h2 = 0.0611, l = 0.071, alphax = 4.38, alphay = 4.38 , W=3e-3, mx = 0, my = 0) AT (0, 0, 8.9945) RELATIVE arm1
//——————————CHOPPER
COMPONENT chop1 = DiskChopper(theta_0 = 336, radius = 0.298, yheight = 0.086, nu = nu_chop, nslit = 1, jitter = 0.000009, phase = 200.4+phase_chop, isfirst = 0, n_pulse = 1, abs_out = 1) AT (0, 0, 9.455) RELATIVE arm1
//——————————LONG FLIGHT PATH
COMPONENT slit_tosca3 = Slit(xmin = -0.02935, xmax = 0.02935, ymin = -0.02935, ymax = 0.02935) AT (0, 0, 10.324) RELATIVE arm1
COMPONENT guide5_1 = Guide_channeled(w1 = 0.0587, h1 = 0.0587, w2 = 0.0434, h2 = 0.0434, l = 5.436, alphax = 4.38, alphay = 4.38, W=3e-3, mx = m_lfp, my = m_lfp) AT (0, 0, 10.325) RELATIVE arm1
COMPONENT guide_end = Guide_channeled(w1 = 0.0434, h1 = 0.0434, w2 = 0.040, h2 = 0.040, l = 0.033, alphax = 4.38, alphay = 4.38, W=3e-3, mx = 0, my = 0) AT (0, 0, 15.761) RELATIVE arm1
//——————————BEAM MONITOR: DET-141
COMPONENT TOFlog_141 = TOFlog_monitor(tmin = t_min, tmax = t_max, ndec = 4000, yheight = 0.05, xwidth = 0.05, restore_neutron = 1) AT (0, 0, 15.794) RELATIVE arm1
//——————————SAMPLE MONITOR
COMPONENT sample_PSD = PSD_monitor(nx = 500, ny = 500, restore_neutron = 1, xwidth = monitor_dimx, yheight = monitor_dimy) AT (0, 0, 16.997) RELATIVE arm1
COMPONENT PSD_lin_mon = PSDlin_monitor(nx = 500, xwidth = monitor_dimx, yheight = monitor_dimy, restore_neutron = 1) AT (0, 0, 16.997) RELATIVE arm1
COMPONENT sample_div_small = Divergence_monitor(nh = 500, nv = 500, xwidth = 0.04, yheight = 0.04, maxdiv_h = 1, maxdiv_v = 1, restore_neutron = 1) AT (0, 0, 16.997) RELATIVE arm1
COMPONENT sample_Emon = E_monitor(nE = 5000, xwidth = 0.04, yheight = 0.04, Emin = Emon_min, Emax = Emon_max, restore_neutron = 1) AT (0, 0, 16.997) RELATIVE arm1
COMPONENT sample_Lmon = L_monitor(nL = 5000, xwidth = 0.04, yheight = 0.04, Lmin = L_min, Lmax = L_max, restore_neutron = 1) AT (0, 0, 16.997) RELATIVE arm1
//——————————INES BEAMLINE
COMPONENT slit_ines1 = Slit(xmin = -0.05, xmax = 0.05, ymin = -0.05, ymax = 0.05) AT (0, 0, 17.69) RELATIVE arm1
COMPONENT ines_tubePSD = PSD_monitor(nx = 500, ny = 500, restore_neutron = 1, xwidth = 0.1, yheight = 0.1) AT (0, 0, 17.691) RELATIVE arm1 ROTATED (0, 0, 0) ABSOLUTE
COMPONENT coll1 = Guide_channeled(w1 = 0.1, h1 = 0.1, w2 = 0.1, h2 = 0.1, l = 1.308, alphax = 4.38, alphay = 4.38 , W=3e-3, mx = 0, my = 0) AT (0, 0, 17.692) RELATIVE arm1
COMPONENT gap_ines1 = Guide_channeled(w1 = 0.1, h1 = 0.1, w2 = 0.1, h2 = 0.1, l = 0.100, alphax = 4.38, alphay = 4.38 , W=3e-3, mx = 0, my = 0) AT (0, 0, 19.000) RELATIVE arm1
COMPONENT coll2 = Guide_channeled(w1 = 0.1, h1 = 0.1, w2 = 0.1, h2 = 0.1, l = 2.715, alphax = 4.38, alphay = 4.38 , W=3e-3, mx = 0, my = 0) AT (0, 0, 19.100) RELATIVE arm1
//——————————INES SAMPLE POSITION
COMPONENT arm_sample_ines = Arm() AT (0,0, 22.804) ABSOLUTE
COMPONENT ines_sample_PSD = PSD_monitor(nx = 500, ny = 500, restore_neutron = 1, xwidth = monitor_dimx, yheight = monitor_dimy) AT (0, 0, 22.804) RELATIVE arm1
COMPONENT ines_PSD_lin_PSD = PSDlin_monitor(nx = 500, xwidth = monitor_dimx, yheight = monitor_dimy, restore_neutron = 1) AT (0, 0, 22.804) RELATIVE arm1
COMPONENT ines_sample_div = Divergence_monitor(nh = 500, nv = 500, xwidth = 0.04, yheight = 0.04, maxdiv_h = 1, maxdiv_v = 1, restore_neutron = 1) AT (0, 0, 22.804) RELATIVE arm1
COMPONENT ines_sample_Emon = E_monitor(nE = 5000, xwidth = 0.04, yheight = 0.04,

Emin = Emon_min, Emax = Emon_max, restore_neutron = 1) AT (0, 0, 22.804) RELATIVE arm1
COMPONENT ines_sample_Lmon = L_monitor(nL = 5000, xwidth = 0.04, yheight = 0.04, Lmin = L_min, Lmax = L_max, restore_neutron = 1) AT (0, 0, 22.804) RELATIVE arm1
END

A.2. Model of TOSCA diffraction spectrometer

/* Created by: Roberto Simone Pinna, ISIS, RAL, 2014. */

DEFINE INSTRUMENT tosca(m_shutter = 0, m_monolith = 0, m_bef_vac = 0, m_lfp = 0, l_min = 0.286, l_max = 6.4, focus_d = 1000, nu_chop = 0, phase_chop = 28, string sample="HOPG.rfl", s_x = 0.04, s_y = 0.03, s_z = 0.002, d_spacing = 3.354, M_Mosaic = 150, debye_sample = 0, deltad_sample = 0, alpha = -0.86)
DECLARE %{ double v_foc, c_h1, c_h2, slit_curv, num_slits; double E_min, E_max, t1, t2; double m_shutter, m_monolith, m_bef_vac, m_lfp, debye_sample, deltad_sample, alpha; double lam, deg_phase, phase_time; double phase; double monitor_dimx = 0.10; double monitor_dimy = 0.10; double Emon_min = 1; double Emon_max = 1000; double Lmon_min = 0.2; double Lmon_max = 5; double t_min = 1000; double t_max = 40000; double nu_chop; double phase_chop; double dfr_wdt = 0.01; double dfr_hgt = 0.06; double l_flight = 18.21; double theta_146 = 2.72; double theta_147 = 1.72; }
INITIALIZE %{ E_min=81.799/l_max/l_max; E_max=81.799/l_min/l_min; %}
TRACE
COMPONENT Origin = Progress_bar() AT (0,0,0) ABSOLUTE
COMPONENT arm1 = Arm() AT (0,0,0) ABSOLUTE
COMPONENT arm_146 = Arm() AT (0,0,17) ABSOLUTE ROTATED (0, (180-theta_146), 0) ABSOLUTE
COMPONENT arm_147 = Arm() AT (0,0,17) ABSOLUTE ROTATED (0, (180-theta_147), 0) ABSOLUTE
COMPONENT arm_148 = Arm() AT (0,0,17) ABSOLUTE ROTATED (0, (180+theta_147), 0) ABSOLUTE
COMPONENT arm_149 = Arm() AT (0,0,17) ABSOLUTE ROTATED (0, (180+theta_146), 0) ABSOLUTE
//—————————MODERATOR
COMPONENT isis_moderator = ISIS_moderator(Face = "tosca", Emin = E_min, Emax = E_max, dist = 1.625, focus_xw = s_x, focus_yh = s_y, xwidth = s_x, yheight = s_y, CAngle = 0, SAC = 1) AT (0, 0, 0) RELATIVE arm1
//—————————BEAM MONITOR: DET-141
COMPONENT TOFlog_141 = TOFlog_monitor(tmin = t_min, tmax = t_max, ndec = 4000, yheight = 0.05, xwidth = 0.05, restore_neutron = 1) AT (0, 0, 15.794) RELATIVE arm1
//—————————SAMPLE
SPLIT COMPONENT arm_sample = Arm() AT (0,0,17.000) RELATIVE arm1 ROTATED (0,alpha,0) RELATIVE arm1
COMPONENT monocr_sample = Monochromator_curved(order=0, mosaich = M_Mosaic, mosaicv = M_Mosaic, width = s_x, height = s_y, DM = d_spacing, reflect=sample, NH = 1, NV = 1, RH = 0, gap = 0) AT (0, 0, 0) RELATIVE arm_sample ROTATED (0, 90, 0) RELATIVE arm_sample EXTEND %{ if (!SCATTERED) ABSORB; %}
//——————-DIFFRACTOMETER #146
COMPONENT TOFlog_He3_146 = Monitor_nD(options = "box, log time limits=[-3,-1] bins = 4000 parallel 3He_pressure=20", yheight = 0.06, xwidth = 0.01, zdepth=0.01, restore_neutron = 1) AT (0,0,(l_flight-17)) RELATIVE arm_146

//——————-DIFFRACTOMETER #147
COMPONENT TOFlog_He3_147 = Monitor_nD(options = "box, log time, limits=[-3,-1], bins = 4000, parallel, 3He_pressure=20", yheight = 0.06, xwidth = 0.01, zdepth=0.01, restore_neutron = 1) AT (0,0,(l_flight-17)) RELATIVE arm__147
//——————-DIFFRACTOMETER #148
COMPONENT TOFlog_He3_148 = Monitor_nD(options = "box, log time, limits=[-3,-1], bins = 4000, parallel, 3He_pressure=20", yheight = 0.06, xwidth = 0.01, zdepth=0.01, restore_neutron = 1) AT (0,0,(l_flight-17)) RELATIVE arm__148
//——————-DIFFRACTOMETER #149
COMPONENT TOFlog_He3_149 = Monitor_nD(options = "box, log time, limits=[-3,-1], bins = 4000, parallel, 3He_pressure=20", yheight = 0.06, xwidth = 0.01, zdepth=0.01, restore_neutron = 1) AT (0,0,(l_flight-17)) RELATIVE arm__149
END

A.3. Model of TOSCA INS spectrometer

/* Created by: Roberto Simone Pinna, ISIS, RAL, 2014. */

DEFINE INSTRUMENT tosca(m_shutter = 0, m_monolith = 0, m_bef_vac = 0, m_lfp = 0, l_min = 4.26, l_max = 5.22, focus_d = 17, nu_chop = 0, phase_chop = 28, string sample = "H2O_ice_1h.laz", s_radius = 0.02, s_y = 0.04, s_thick = 0.002, monochr_wdt = 0.15, monochr_hgt = 0.04, M_Mosaic = 150, order_mono = 1, deltad_mono = 0.00025, debye_filter = 0.5, DWidth = 0.30, DHeight = 0.01)
DECLARE %{int flag_env,flag_sample; double v_foc, c_h1, c_h2, slit_curv, num_slits; double E_min, E_max; double m_shutter, m_monolith, m_bef_vac, m_lfp; double lam, deg_phase, phase_time; double phase; double monitor_dimx = 0.10; double monitor_dimy = 0.10; double Emon_min = 1; double Emon_max = 1000; double Lmon_min = 0.2; double Lmon_max = 5; double t_min = 1000; double t_max = 40000; double nu_chop; double phase_chop; double Xmb, Ymb, Zmb; double Xmf, Ymf, Zmf; double d_spacing = 3.354; double deltad_mono; double M_Mosaic; double reflect = 0.866; double monochr_wdt ; double monochr_hgt; double trm_filter; double Xdb, Ydb, Zdb; double Xdf, Ydf, Zdf; double DWidth; double DHeight; double tmin_back = 5000; double tmin_fwd = 5000; double tmax_back = 40000; double tmax_fwd = 40000; double emin_back = 1; double emin_fwd = 1; double emax_back = 1000; double emax_fwd = 1000; double lmin_back = 0.286; double lmin_fwd = 0.286; double lmax_back = 5; double lmax_fwd = 5; double dz_shield = 0.2; double dx_shield; double l_flight_back = 17.6244; double l_flight_fwd = 17.6242; double dtheta = 60; double phi_back = 135; double phi_fwd = 45; double dtheta_rad, phi_back_rad, phi_fwd_rad; %}
INITIALIZE %{E_min = 81.799/l_max/l_max; E_max = 81.799/l_min/l_min; dtheta_rad = (PI/180) * dtheta; phi_back_rad = (PI/180) * phi_back; phi_fwd_rad = (PI/180) * phi_fwd; Xmf = 0; Ymf = ((l_flight_fwd-17)/2) * sin(phi_fwd_rad); Zmf = ((l_flight_fwd-17)/2) * cos(phi_fwd_rad); Xdf = 0; Ydf = (l_flight_fwd-17) * sin(phi_fwd_rad); Zdf = 17.002-17; Xmb = 0; Ymb = ((l_flight_back-17)/2) * sin(phi_back_rad); Zmb = ((l_flight_back-17)/2) * cos(phi_back_rad); Xdb = 0; Ydb = (l_flight_back-17) * sin(phi_back_rad); Zdb = 16.998-17; dx_shield = 2 * Ymb * (tan(dtheta_rad/2))%}
TRACE
COMPONENT Origin = Progress_bar() AT (0,0,0) ABSOLUTE
COMPONENT arm1 = Arm() AT (0,0,0) ABSOLUTE
COMPONENT arm_b1 = Arm() AT (-0.20023, 0.1156, 16.7897) RELATIVE arm1 ROTATED (0, 90, 0) RELATIVE arm1
COMPONENT arm_60 = Arm() AT (0,0,17) RELATIVE arm1 ROTATED (0, 0, dtheta) RELATIVE arm1

COMPONENT arm_120 = Arm() AT (0,0,17) RELATIVE arm1 ROTATED (0, 0, dtheta*2) RELATIVE arm1
COMPONENT arm_180 = Arm() AT (0,0,17) RELATIVE arm1 ROTATED (0, 0, dtheta*3) RELATIVE arm1
COMPONENT arm_240 = Arm() AT (0,0,17) RELATIVE arm1 ROTATED (0, 0, dtheta*4) RELATIVE arm1
COMPONENT arm_300 = Arm() AT (0,0,17) RELATIVE arm1 ROTATED (0, 0, dtheta*5) RELATIVE arm1
//————————————MODERATOR
COMPONENT isis_moderator = ISIS_moderator(Face = "tosca", Emin = E_min, Emax = E_max, dist = 1.625, focus_xw = s_x, focus_yh = s_y, xwidth = s_x, yheight = s_y, CAngle = 0, SAC = 1) AT (0, 0, 0) RELATIVE arm1
//————————————BEAM MONITOR: DET-141
COMPONENT TOFlog_141 = TOFlog_monitor(tmin = t_min, tmax = t_max, ndec = 4000, yheight = 0.05, xwidth = 0.05, restore_neutron = 1) AT (0, 0, 15.794) RELATIVE arm1
//————————————SAMPLE
SPLIT COMPONENT arm_sample = Arm() AT (0, 0, 17.000) RELATIVE arm1 EXTEND %{ flag_env=flag_sample=0; %}
COMPONENT powder = PowderN(reflections = sample, d_phi = 105, xwidth = 2*s_radius, yheight = s_y, zdepth = s_thick) AT (0, 0, 0) RELATIVE arm_sample EXTEND %{ if (!SCATTERED) ABSORB; %}
//————————————SHIELDING
COMPONENT Mirror_bank0 = Mirror(xwidth = dx_shield, yheight = dz_shield, m = 0, center = 1, transmit = 0) AT (0, Ymb, 0) RELATIVE arm_sample ROTATED (90, 0, 0) RELATIVE arm_sample
COMPONENT Mirror_bank1 = Mirror(xwidth = dx_shield, yheight = dz_shield, m = 0, center = 1, transmit = 0) AT (0, Ymb, 0) RELATIVE arm_60 ROTATED (90, 0, 0) RELATIVE arm_60
COMPONENT Mirror_bank2 = Mirror(xwidth = dx_shield, yheight = dz_shield, m = 0, center = 1, transmit = 0) AT (0, Ymb, 0) RELATIVE arm_120 ROTATED (90, 0, 0) RELATIVE arm_120
COMPONENT Mirror_bank3 = Mirror(xwidth = dx_shield, yheight = dz_shield, m = 0, center = 1, transmit = 0) AT (0, Ymb, 0) RELATIVE arm_180 ROTATED (90, 0, 0) RELATIVE arm_180
COMPONENT Mirror_bank4 = Mirror(xwidth = dx_shield, yheight = dz_shield, m = 0, center = 1, transmit = 0) AT (0, Ymb, 0) RELATIVE arm_240 ROTATED (90, 0, 0) RELATIVE arm_240
COMPONENT Mirror_bank5 = Mirror(xwidth = dx_shield, yheight = dz_shield, m = 0, center = 1, transmit = 0) AT (0, Ymb, 0) RELATIVE arm_300 ROTATED (90, 0, 0) RELATIVE arm_300
//————————————BACKWARD BANK 1
COMPONENT monocr_b1 = Monochromator_curved(order=order_mono, mosaich = M_Mosaic, mosaicv = M_Mosaic, width = monochr_wdt, height = monochr_hgt, DM = d_spacing, reflect="HOPG.rfl", NH = 15, NV = 10, RH = 0, gap = 0.001) AT (Xmb, Ymb, Zmb) RELATIVE arm_60 ROTATED (0, 90, 0) RELATIVE arm_60
COMPONENT monocr_b1_A = Monochromator_curved(order=order_mono, reflect="HOPG.rfl", mosaich = M_Mosaic, mosaicv = M_Mosaic, width = monochr_wdt, height = monochr_hgt, DM = d_spacing*(1+deltad_mono), NH = 15, NV = 10, RH = 0, gap = 0.001) AT (0, 0, 0) RELATIVE monocr_b1 ROTATED (0, 0, 0) RELATIVE monocr_b1
COMPONENT monocr_b1_B = Monochromator_curved(order=order_mono, reflect="HOPG.rfl", mosaich = M_Mosaic, mosaicv = M_Mosaic, width = monochr_wdt, height = monochr_hgt, DM = d_spacing*(1-deltad_mono), NH = 15, NV = 10, RH = 0, gap = 0.001) AT (0, 0, 0) RELATIVE monocr_b1 ROTATED (0, 0, 0) RELATIVE monocr_b1

COMPONENT TOF_He3_b1 = Monitor_nD(options = "box, time limits=[0.017,0.025] bins = 500 parallel 3He_pressure=20", xwidth = DWidth, yheight = DHeight, zdepth=0.0025, restore_neutron = 1) AT (Xdb, Ydb, Zdb) RELATIVE arm_60
//—————————BACKWARD BANK 2
COMPONENT monocr_b2 = Monochromator_curved(order=order_mono, mosaich = M_Mosaic, mosaicv = M_Mosaic, width = monochr_wdt, height = monochr_hgt, DM = d_spacing, reflect="HOPG.rfl", NH = 15, NV = 10, RH = 0, gap = 0.001) AT (Xmb, Ymb, Zmb) RELATIVE arm_120 ROTATED (0, 90, 0) RELATIVE arm_120
COMPONENT monocr_b2_A = Monochromator_curved(order=order_mono, reflect="HOPG.rfl", mosaich = M_Mosaic, mosaicv = M_Mosaic, width = monochr_wdt, height = monochr_hgt, DM = d_spacing*(1+deltad_mono), NH = 15, NV = 10, RH = 0, gap = 0.001) AT (0, 0, 0) RELATIVE monocr_b2 ROTATED (0, 0, 0) RELATIVE monocr_b2
COMPONENT monocr_b2_B = Monochromator_curved(order=order_mono, reflect="HOPG.rfl", mosaich = M_Mosaic, mosaicv = M_Mosaic, width = monochr_wdt, height = monochr_hgt, DM = d_spacing*(1-deltad_mono), NH = 15, NV = 10, RH = 0, gap = 0.001) AT (0, 0, 0) RELATIVE monocr_b2 ROTATED (0, 0, 0) RELATIVE monocr_b2
COMPONENT TOF_He3_b2 = Monitor_nD(options = "box, time limits=[0.017,0.025] bins = 500 parallel 3He_pressure=20", xwidth = DWidth, yheight = DHeight, zdepth=0.0025, restore_neutron = 1) AT (Xdb, Ydb, Zdb) RELATIVE arm_120
//—————————BACKWARD BANK 3
COMPONENT monocr_b3 = Monochromator_curved(order=order_mono, mosaich = M_Mosaic, mosaicv = M_Mosaic, width = monochr_wdt, height = monochr_hgt, DM = d_spacing, reflect="HOPG.rfl", NH = 15, NV = 10, RH = 0, gap = 0.001) AT (Xmb, Ymb, Zmb) RELATIVE arm_180 ROTATED (0, 90, 0) RELATIVE arm_180
COMPONENT monocr_b3_A = Monochromator_curved(order=order_mono, reflect="HOPG.rfl", mosaich = M_Mosaic, mosaicv = M_Mosaic, width = monochr_wdt, height = monochr_hgt, DM = d_spacing*(1+deltad_mono), NH = 15, NV = 10, RH = 0, gap = 0.001) AT (0, 0, 0) RELATIVE monocr_b3 ROTATED (0, 0, 0) RELATIVE monocr_b3
COMPONENT monocr_b3_B = Monochromator_curved(order=order_mono, reflect="HOPG.rfl", mosaich = M_Mosaic, mosaicv = M_Mosaic, width = monochr_wdt, height = monochr_hgt, DM = d_spacing*(1-deltad_mono), NH = 15, NV = 10, RH = 0, gap = 0.001) AT (0, 0, 0) RELATIVE monocr_b3 ROTATED (0, 0, 0) RELATIVE monocr_b3
COMPONENT TOF_He3_b3 = Monitor_nD(options = "box, time limits=[0.017,0.025] bins = 500 parallel 3He_pressure=20", xwidth = DWidth, yheight = DHeight, zdepth=0.0025, restore_neutron = 1) AT (Xdb, Ydb, Zdb) RELATIVE arm_180
//—————————BACKWARD BANK 4
COMPONENT monocr_b4 = Monochromator_curved(order=order_mono, mosaich = M_Mosaic, mosaicv = M_Mosaic, width = monochr_wdt, height = monochr_hgt, DM = d_spacing, reflect="HOPG.rfl", NH = 15, NV = 10, RH = 0, gap = 0.001) AT (Xmb, Ymb, Zmb) RELATIVE arm_240 ROTATED (0, 90, 0) RELATIVE arm_240
COMPONENT monocr_b4_A = Monochromator_curved(order=order_mono, reflect="HOPG.rfl", mosaich = M_Mosaic, mosaicv = M_Mosaic, width = monochr_wdt, height = monochr_hgt, DM = d_spacing*(1+deltad_mono), NH = 15, NV = 10, RH = 0, gap = 0.001) AT (0, 0, 0) RELATIVE monocr_b4 ROTATED (0, 0, 0) RELATIVE monocr_b4
COMPONENT monocr_b4_B = Monochromator_curved(order=order_mono, reflect="HOPG.rfl", mosaich = M_Mosaic, mosaicv = M_Mosaic, width = monochr_wdt, height = monochr_hgt, DM = d_spacing*(1-deltad_mono), NH = 15, NV = 10, RH = 0, gap = 0.001) AT (0, 0, 0) RELATIVE monocr_b4 ROTATED (0, 0, 0) RELATIVE monocr_b4
COMPONENT TOF_He3_b4 = Monitor_nD(options = "box, time limits=[0.017,0.025] bins = 500 parallel 3He_pressure=20", xwidth = DWidth, yheight = DHeight, zdepth=0.0025, restore_neutron = 1) AT (Xdb, Ydb, Zdb) RELATIVE arm_240
//—————————BACKWARD BANK 5

COMPONENT monocr_b5 = Monochromator_curved(order=order_mono, mosaich = M_Mosaic, mosaicv = M_Mosaic, width = monochr_wdt, height = monochr_hgt, DM = d_spacing, reflect="HOPG.rfl", NH = 15, NV = 10, RH = 0, gap = 0.001) AT (Xmb, Ymb, Zmb) RELATIVE arm_300 ROTATED (0, 90, 0) RELATIVE arm_300

COMPONENT monocr_b5_A = Monochromator_curved(order=order_mono, reflect="HOPG.rfl", mosaich = M_Mosaic, mosaicv = M_Mosaic, width = monochr_wdt, height = monochr_hgt, DM = d_spacing*(1+deltad_mono), NH = 15, NV = 10, RH = 0, gap = 0.001) AT (0, 0, 0) RELATIVE monocr_b5 ROTATED (0, 0, 0) RELATIVE monocr_b5

COMPONENT monocr_b5_B = Monochromator_curved(order=order_mono, reflect="HOPG.rfl", mosaich = M_Mosaic, mosaicv = M_Mosaic, width = monochr_wdt, height = monochr_hgt, DM = d_spacing*(1-deltad_mono), NH = 15, NV = 10, RH = 0, gap = 0.001) AT (0, 0, 0) RELATIVE monocr_b5 ROTATED (0, 0, 0) RELATIVE monocr_b5

COMPONENT TOF_He3_b5 = Monitor_nD(options = "box, time limits=[0.017,0.025] bins = 500 parallel 3He_pressure=20", xwidth = DWidth, yheight = DHeight, zdepth=0.0025, restore_neutron = 1) AT (Xdb, Ydb, Zdb) RELATIVE arm_300

//————————————FORWARD BANK 1

COMPONENT monocr_f1 = Monochromator_curved(order=order_mono, reflect="HOPG.rfl", mosaich = M_Mosaic, mosaicv = M_Mosaic, width = monochr_wdt, height = monochr_hgt, r0 = 1, DM = d_spacing*(1), NH = 15, NV = 10, RH = 0, gap = 0.001) AT (Xmf, Ymf, Zmf) RELATIVE arm_60 ROTATED (0, 90, 0) RELATIVE arm_60

COMPONENT monocr_f1_A = Monochromator_curved(order=order_mono, reflect="HOPG.rfl", mosaich = M_Mosaic, mosaicv = M_Mosaic, width = monochr_wdt, height = monochr_hgt, r0 = 1, DM = d_spacing*(1+deltad_mono), NH = 15, NV = 10, RH = 0, gap = 0.001) AT (0, 0, 0) RELATIVE monocr_f1 ROTATED (0, 0, 0) RELATIVE monocr_f1

COMPONENT monocr_f1_B = Monochromator_curved(order=order_mono, reflect="HOPG.rfl", mosaich = M_Mosaic, mosaicv = M_Mosaic, width = monochr_wdt, height = monochr_hgt, r0 = 1, DM = d_spacing*(1-deltad_mono), NH = 15, NV = 10, RH = 0, gap = 0.001) AT (0, 0, 0) RELATIVE monocr_f1 ROTATED (0, 0, 0) RELATIVE monocr_f1

COMPONENT f1_TOFlog_He3 = Monitor_nD(options = "box, time limits=[0.017,0.025] bins = 500 parallel 3He_pressure=20", xwidth = DWidth, yheight = DHeight, zdepth=0.0025, restore_neutron = 1) AT (Xdf, Ydf, Zdf) RELATIVE arm_60

//————————————FORWARD BANK 2

COMPONENT monocr_f2 = Monochromator_curved(order=order_mono, reflect="HOPG.rfl", mosaich = M_Mosaic, mosaicv = M_Mosaic, width = monochr_wdt, height = monochr_hgt, r0 = 1, DM = d_spacing*(1), NH = 15, NV = 10, RH = 0, gap = 0.001) AT (Xmf, Ymf, Zmf) RELATIVE arm_120 ROTATED (0, 90, 0) RELATIVE arm_120

COMPONENT monocr_f2_A = Monochromator_curved(order=order_mono, reflect="HOPG.rfl", mosaich = M_Mosaic, mosaicv = M_Mosaic, width = monochr_wdt, height = monochr_hgt, r0 = 1, DM = d_spacing*(1+deltad_mono), NH = 15, NV = 10, RH = 0, gap = 0.001) AT (0, 0, 0) RELATIVE monocr_f2 ROTATED (0, 0, 0) RELATIVE monocr_f2

COMPONENT monocr_f2_B = Monochromator_curved(order=order_mono, reflect="HOPG.rfl", mosaich = M_Mosaic, mosaicv = M_Mosaic, width = monochr_wdt, height = monochr_hgt, r0 = 1, DM = d_spacing*(1-deltad_mono), NH = 15, NV = 10, RH = 0, gap = 0.001) AT (0, 0, 0) RELATIVE monocr_f2 ROTATED (0, 0, 0) RELATIVE monocr_f2

COMPONENT f2_TOFlog_He3 = Monitor_nD(options = "box, time limits=[0.017,0.025] bins = 500 parallel 3He_pressure=20", xwidth = DWidth, yheight = DHeight, zdepth=0.0025, restore_neutron = 1) AT (Xdf, Ydf, Zdf) RELATIVE arm_120

//————————————FORWARD BANK 3

COMPONENT monocr_f3 = Monochromator_curved(order=order_mono, reflect="HOPG.rfl", mosaich = M_Mosaic, mosaicv = M_Mosaic, width = monochr_wdt, height = monochr_hgt, r0 = 1, DM = d_spacing*(1), NH = 15, NV = 10, RH = 0, gap = 0.001) AT (Xmf, Ymf, Zmf) RELATIVE arm_180 ROTATED (0, 90, 0) RELATIVE arm_180

COMPONENT monocr_f3_A = Monochromator_curved(order=order_mono, reflect="HOPG.rfl", mosaich = M_Mosaic, mosaicv = M_Mosaic, width = monochr_wdt, height = monochr_hgt, r0 = 1, DM = d_spacing*(1+deltad_mono), NH = 15, NV = 10, RH = 0, gap = 0.001) AT (0, 0, 0) RELATIVE monocr_f3 ROTATED (0, 0, 0) RELATIVE monocr_f3
COMPONENT monocr_f3_B = Monochromator_curved(order=order_mono, reflect="HOPG.rfl", mosaich = M_Mosaic, mosaicv = M_Mosaic, width = monochr_wdt, height = monochr_hgt, r0 = 1, DM = d_spacing*(1-deltad_mono), NH = 15, NV = 10, RH = 0, gap = 0.001) AT (0, 0, 0) RELATIVE monocr_f3 ROTATED (0, 0, 0) RELATIVE monocr_f3
COMPONENT f3_TOFlog_He3 = Monitor_nD(options = "box, time limits=[0.017,0.025] bins = 500 parallel 3He_pressure=20", xwidth = DWidth, yheight = DHeight, zdepth=0.0025, restore_neutron = 1) AT (Xdf, Ydf, Zdf) RELATIVE arm_180
//———————————FORWARD BANK 4
COMPONENT monocr_f4 = Monochromator_curved(order=order_mono, reflect="HOPG.rfl", mosaich = M_Mosaic, mosaicv = M_Mosaic, width = monochr_wdt, height = monochr_hgt, r0 = 1, DM = d_spacing*(1), NH = 15, NV = 10, RH = 0, gap = 0.001) AT (Xmf, Ymf, Zmf) RELATIVE arm_240 ROTATED (0, 90, 0) RELATIVE arm_240
COMPONENT monocr_f4_A = Monochromator_curved(order=order_mono, reflect="HOPG.rfl", mosaich = M_Mosaic, mosaicv = M_Mosaic, width = monochr_wdt, height = monochr_hgt, r0 = 1, DM = d_spacing*(1+deltad_mono), NH = 15, NV = 10, RH = 0, gap = 0.001) AT (0, 0, 0) RELATIVE monocr_f4 ROTATED (0, 0, 0) RELATIVE monocr_f4
COMPONENT monocr_f4_B = Monochromator_curved(order=order_mono, reflect="HOPG.rfl", mosaich = M_Mosaic, mosaicv = M_Mosaic, width = monochr_wdt, height = monochr_hgt, r0 = 1, DM = d_spacing*(1-deltad_mono), NH = 15, NV = 10, RH = 0, gap = 0.001) AT (0, 0, 0) RELATIVE monocr_f4 ROTATED (0, 0, 0) RELATIVE monocr_f4
COMPONENT f4_TOFlog_He3 = Monitor_nD(options = "box, time limits=[0.017,0.025] bins = 500 parallel 3He_pressure=20", xwidth = DWidth, yheight = DHeight, zdepth=0.0025, restore_neutron = 1) AT (Xdf, Ydf, Zdf) RELATIVE arm_240
//———————————FORWARD BANK 5
COMPONENT monocr_f5 = Monochromator_curved(order=order_mono, reflect="HOPG.rfl", mosaich = M_Mosaic, mosaicv = M_Mosaic, width = monochr_wdt, height = monochr_hgt, r0 = 1, DM = d_spacing*(1), NH = 15, NV = 10, RH = 0, gap = 0.001) AT (Xmf, Ymf, Zmf) RELATIVE arm_300 ROTATED (0, 90, 0) RELATIVE arm_300
COMPONENT monocr_f5_A = Monochromator_curved(order=order_mono, reflect="HOPG.rfl", mosaich = M_Mosaic, mosaicv = M_Mosaic, width = monochr_wdt, height = monochr_hgt, r0 = 1, DM = d_spacing*(1+deltad_mono), NH = 15, NV = 10, RH = 0, gap = 0.001) AT (0, 0, 0) RELATIVE monocr_f5 ROTATED (0, 0, 0) RELATIVE monocr_f5
COMPONENT monocr_f5_B = Monochromator_curved(order=order_mono, reflect="HOPG.rfl", mosaich = M_Mosaic, mosaicv = M_Mosaic, width = monochr_wdt, height = monochr_hgt, r0 = 1, DM = d_spacing*(1-deltad_mono), NH = 15, NV = 10, RH = 0, gap = 0.001) AT (0, 0, 0) RELATIVE monocr_f5 ROTATED (0, 0, 0) RELATIVE monocr_f5
COMPONENT f5_TOFlog_He3 = Monitor_nD(options = "box, time limits=[0.017,0.025] bins = 500 parallel 3He_pressure=20", xwidth = DWidth, yheight = DHeight, zdepth=0.0025, restore_neutron = 1) AT (Xdf, Ydf, Zdf) RELATIVE arm_300
END

A.4. Model of TOSCA beamline with the neutron guide

/* Created by: Roberto Simone Pinna, ISIS, RAL, 2014. */

DEFINE INSTRUMENT tosca(m_shutter = 0, m_monolith1 = 0, m_monolith2 = 0 ,m_vac1 = 0, m_vac2 = 0, m_vac3 = 0, m_bef_chop = 0, m_lfp1 = 0, m_lfp2 = 0, m_lfp3 = 0, m_lfp4 = 0, m_lfp5 = 0, m_last = 0, nu_chop = 0, phase_chop = 28, E_min = 1, E_max = 1000)

DECLARE %{ double v_foc, c_h1, c_h2, slit_curv, num_slits; double E_min, E_max; double m_shutter, m_monolith1, m_monolith2, m_vac1, m_vac2, m_vac3, m_bef_chop1, m_lfp1, m_lfp2, m_lfp3, m_lfp4, m_lfp5, m_last; double lam, deg_phase, phase_time; double phase; double monitor_dimx = 0.10; double monitor_dimy = 0.10; int resx = 500; int resy = 500; double Emon_min = 1; double Emon_max = 1000; double L_min = 0.2; double L_max = 5; double t_min = 1000; double t_max = 40000;%}

TRACE

//————————MODERATOR

COMPONENT isis_moderator = ISIS_moderator(Face = "tosca", Emin = E_min, Emax = E_max, dist = 1.625, focus_xw = 0.12, focus_yh = 0.115, xwidth = 0.12, yheight = 0.115, CAngle = 0, SAC = 1) AT (0, 0, 0) RELATIVE arm1

//————————SHUTTER

COMPONENT slit_tosca1 = Slit(xmin = -0.05, xmax = 0.05, ymin = -0.05, ymax = 0.05) AT (0, 0, 1.625) RELATIVE arm1

COMPONENT guide1 = Guide_channeled(w1 = 0.10, h1 = 0.10, w2 = 0.10, h2 = 0.10, l = 1.938, alphax = 4.38, alphay = 4.38 , W=3e-3, mx = m_shutter, my = m_shutter) AT (0, 0, 1.625) RELATIVE arm1

//————————MONOLITH

COMPONENT gap1 = Guide_channeled(w1 = 0.1, h1 = 0.1, w2 = 0.1, h2 = 0.1, l = 0.110, alphax = 4.38, alphay = 4.38 , W=3e-3, mx = 0, my = 0) AT (0, 0, 3.563) RELATIVE arm1

COMPONENT guide2_1 = Guide_channeled(w1 = 0.1, h1 = 0.1, w2 = 0.0928, h2 = 0.0928, l = 1.500, alphax = 4.38, alphay = 4.38 , W=3e-3, mx = m_monolith1, my = m_monolith1) AT (0, 0, 3.673) RELATIVE arm1

COMPONENT guide2_2 = Guide_channeled(w1 = 0.0928, h1 = 0.0928, w2 = 0.0889, h2 = 0.0889, l = 0.800, alphax = 4.38, alphay = 4.38 , W=3e-3, mx = m_monolith2, my = m_monolith2) AT (0, 0, 5.173) RELATIVE arm1

//————————VACUUM VALVE

COMPONENT gap2 = Guide_channeled(w1 = 0.0889, h1 = 0.0889, w2 = 0.0889, h2 = 0.0889, l = 0.003, alphax = 4.38, alphay = 4.38 , W=3e-3, mx = 0, my = 0) AT (0, 0, 5.973) RELATIVE arm1

COMPONENT guide3_1 = Guide_channeled(w1 = 0.0889, h1 = 0.0889, w2 = 0.0817, h2 = 0.0817, l = 1.500, alphax = 4.38, alphay = 4.38, W=3e-3, mx = m_vac1, my = m_vac1) AT (0, 0, 5.976) RELATIVE arm1

COMPONENT guide3_2 = Guide_channeled(w1 = 0.0817, h1 = 0.0817, w2 = 0.0745, h2 = 0.0745, l = 1.500, alphax = 4.38, alphay = 4.38, W=3e-3, mx = m_vac2, my = m_vac2) AT (0, 0, 7.476) RELATIVE arm1

COMPONENT guide3_3 = Guide_channeled(w1 = 0.0745, h1 = 0.0745, w2 = 0.0745, h2 = 0.0745, l = 0.034, alphax = 4.38, alphay = 4.38, W=3e-3, mx = m_vac3, my = m_vac3) AT (0, 0, 8.976) RELATIVE arm1

//————————CHOPPER

COMPONENT guide4_1 = Guide_channeled(w1 = 0.0745, h1 = 0.0745, w2 = 0.0725, h2 = 0.0725, l = 0.400, alphax = 4.38, alphay = 4.38, W=3e-3, mx = m_bef_chop1, my = m_bef_chop1) AT (0, 0, 9.010) RELATIVE arm1

COMPONENT chop1 = DiskChopper(theta_0 = 336, radius = 0.298, yheight = 0.086, nu =

nu_chop, nslit = 1, jitter = 0.000009, phase = 200.4+phase_chop, isfirst = 0, n_pulse = 1, abs_out = 1) AT (0, 0, 9.455) RELATIVE arm1
//————————————JOINT
COMPONENT slit_tosca2 = Slit(xmin = -0.03625, xmax = 0.03625, ymin = -0.03625, ymax = 0.03625) AT (0, 0, 9.496) RELATIVE arm1
COMPONENT guide5_1 = Guide_channeled(w1 = 0.0725, h1 = 0.0725, w2 = 0.0708, h2 = 0.0708, l = 0.360, alphax = 4.38, alphay = 4.38, W=3e-3, mx = m_lfp1, my = m_lfp1) AT (0, 0, 9.497) RELATIVE arm1
COMPONENT gap3 = Guide_channeled(w1 = 0.0708, h1 = 0.0708, w2 = 0.0708, h2 = 0.0708, l = 0.003, alphax = 4.38, alphay = 4.38 , W=3e-3, mx = 0, my = 0) AT (0, 0, 9.857) RELATIVE arm1
//————————————LONG FLIGHT PATH
COMPONENT guide6_1 = Guide_channeled(w1 = 0.0708, h1 = 0.0708, w2 = 0.0634, h2 = 0.0634, l = 1.538, alphax = 4.38, alphay = 4.38, W=3e-3, mx = m_lfp2, my = m_lfp2) AT (0, 0, 9.860) RELATIVE arm1
COMPONENT guide6_2 = Guide_channeled(w1 = 0.0634, h1 = 0.0634, w2 = 0.0560, h2 = 0.0560, l = 1.538, alphax = 4.38, alphay = 4.38, W=3e-3, mx = m_lfp3, my = m_lfp3) AT (0, 0, 11.398) RELATIVE arm1
COMPONENT guide6_3 = Guide_channeled(w1 = 0.0560, h1 = 0.0560, w2 = 0.0486, h2 = 0.0486, l = 1.538, alphax = 4.38, alphay = 4.38, W=3e-3, mx = m_lfp4, my = m_lfp4) AT (0, 0, 12.936) RELATIVE arm1
COMPONENT guide6_4 = Guide_channeled(w1 = 0.0486, h1 = 0.0486, w2 = 0.0411, h2 = 0.0411, l = 1.538, alphax = 4.38, alphay = 4.38, W=3e-3, mx = m_lfp5, my = m_lfp5) AT (0, 0, 14.474) RELATIVE arm1
//————————————BEAM MONITOR: DET-141
COMPONENT TOFlog_141 = TOFlog_monitor(tmin = t_min, tmax = t_max, ndec = 4000, yheight = 0.05, xwidth = 0.05, restore_neutron = 1) AT (0, 0, 15.794) RELATIVE arm1
//————————————GUIDE END
COMPONENT gap4 = Guide_channeled(w1 = 0.0411, h1 = 0.0411, w2 = 0.0411, h2 = 0.0411, l = 0.008, alphax = 4.38, alphay = 4.38 , W=3e-3, mx = 0, my = 0) AT (0, 0, 16.012) RELATIVE arm1
COMPONENT guide7_1 = Guide_channeled(w1 = 0.0411, h1 = 0.0411, w2 = 0.040, h2 = 0.040, l = 0.230, alphax = 4.38, alphay = 4.38, W=3e-3, mx = m_last, my = m_last) AT (0, 0, 16.020) RELATIVE arm1
//————————————SAMPLE MONITOR
COMPONENT sample_PSD = PSD_monitor(nx = 500, ny = 500, restore_neutron = 1, xwidth = monitor_dimx, yheight = monitor_dimy) AT (0, 0, 16.997) RELATIVE arm1
COMPONENT PSD_lin_mon = PSDlin_monitor(nx = 500, xwidth = monitor_dimx, yheight = monitor_dimy, restore_neutron = 1) AT (0, 0, 16.997) RELATIVE arm1
COMPONENT sample_div_small = Divergence_monitor(nh = 500, nv = 500, xwidth = 0.04, yheight = 0.04, maxdiv_h = 1, maxdiv_v = 1, restore_neutron = 1) AT (0, 0, 16.997) RELATIVE arm1
COMPONENT sample_Emon = E_monitor(nE = 5000, xwidth = 0.04, yheight = 0.04, Emin = Emon_min, Emax = Emon_max, restore_neutron = 1) AT (0, 0, 16.997) RELATIVE arm1
COMPONENT sample_Lmon = L_monitor(nL = 5000, xwidth = 0.04, yheight = 0.04, Lmin = L_min, Lmax = L_max, restore_neutron = 1) AT (0, 0, 16.997) RELATIVE arm1
END

Bibliography

[1] *Neutron News*, 3(3):29–37, 1992.

[2] H. Abele, D. Dubbers, H. Häse, M. Klein, A. Knöpfler, M. Kreuz, T. Lauer, B. Märkisch, D. Mund, and V. Nesvizhevsky. Characterization of a ballistic supermirror neutron guide. *Nuclear Instruments and Methods in Physics Research Section A: Accelerators, Spectrometers, Detectors and Associated Equipment*, 562(1):407–417, 2006.

[3] B. Boardman. Spallation neutron source: description of accelerator and target. Technical report, Science Research Council, Chilton (UK). Rutherford and Appleton Labs, 1982.

[4] Z.A. Bowden, M. Celli, F. Cilloco, D. Colognesi, R.J. Newport, S.F. Parker, F.P. Ricci, V. Rossi-Albertini, F. Sacchetti, and J. Tomkinson. The TOSCA incoherent inelastic neutron spectrometer: progress and results. *Physica B: Condensed Matter*, 276:98–99, 2000.

[5] J.F. Castanon. Monte Carlo simulations for the development of TOSCA's guide at ISIS. Technical Report RAL-TR-2013-002, RAL, Chilton, UK, 2013.

[6] D. Colognesi, M. Celli, F. Cilloco, R.J. Newport, S.F. Parker, V. Rossi-Albertini, F. Sacchetti, J. Tomkinson, and M. Zoppi. TOSCA neutron spectrometer: the final configuration. *Applied Physics A*, 74(1):s64–s66, 2002.

[7] F. Fernandez-Alonso, F.J. Bermejo, C. Cabrillo, R.O. Loutfy, V. Leon, and M.L. Saboungi. Nature of the bound states of molecular hydrogen in carbon nanohorns. *Phys. Rev. Lett.*, 98:215503, May 2007.

[8] F. Fernandez-Alonso and D.L. Price. *Neutron Scattering*, volume 44. Academic Press, 2013.

[9] D.J.S. Findlay. ISIS-pulsed neutron and muon source. In *Particle Accelerator Conference, 2007. PAC. IEEE*, pages 695–699. IEEE, 2007.

[10] F. James. Monte Carlo theory and practice. *Reports on Progress in Physics*, 43(9):1145, 1980.

[11] L. Jones, D. Jenkins, and C. Nelson. Overview of ISIS moderators. Technical report, ISIS Target Design Group, Chilton (UK). Rutherford and Appleton Labs, 2014.

[12] G.F. Knoll. *Radiation Detection and Measurement*. John Wiley & Sons, 2010.

[13] A. Lovell, F. Fernandez-Alonso, N.T. Skipper, K. Refson, S.M. Bennington, and S.F. Parker. Quantum delocalization of molecular hydrogen in alkali-graphite intercalates. *Phys. Rev. Lett.*, 101:126101, Sep 2008.

[14] P.C.H. Mitchell, S.F. Parker, A.J. Ramirez-Cuesta, and J. Tomkinson. *Vibrational Spectroscopy with Neutrons: With Applications in Chemistry, Biology, Materials Science and Catalysis*. Series on neutron techniques and applications. World Scientific publishing, 2005.

[15] A.W. Moore, M. Popovici, and A.D. Stoica. Neutron reflectivity and lattice spacing spread of pyrolytic graphite. *Physica B: Condensed Matter*, 276:858–859, 2000.

[16] S.F. Parker, C.J. Carlile, T. Pike, J. Tomkinson, R.J. Newport, C. Andreani, F.P. Ricci, F. Sacchetti, and M. Zoppi. TOSCA: a world class inelastic neutron spectrometer. *Physica B: Condensed Matter*, 241:154–156, 1997.

[17] S.F. Parker, F. Fernandez-Alonso, A.J. Ramirez-Cuesta, S. Rudic, R.S. Pinna, G. Gorini, and J.F. Castanon. Recent and future developments on TOSCA at ISIS. *ISIS, Harwell, UK*, 2014.

[18] S.F. Parker, J. Tomkinson, A.J. Ramirez-Cuesta, and D. Colognesi. *The TOSCA I User-Guide*. Central Laboratory of the Research Councils, 1999.

[19] J. Penfold and J. Tomkinson. *The ISIS Time Focussed Crystal Analyser Spectrometer, TFXA*. Science and Engineering Research Council (SERC) Rutherford Appleton Laboratory, 1986.

[20] R.S. Pinna, S. Rudic, S.F. Parker, G. Gorini, and F. Fernandez-Alonso. Monte Carlo simulations of the TOSCA spectrometer: Assessment of current performance and future upgrades. *European Physical Journal Web of Conferences*, 2014.

[21] K. Pokhilchuk. Monte Carlo modelling of the OSIRIS neutron backscattering spectrometer. Technical Report 1358-6254, RAL, Chilton, UK, 2013.

[22] C. Prior. Upgrades to the ISIS spallation neutron source. In *Proc. of APAC*, volume 7, pages 300–304.

[23] V. Rossi-Albertini, D. Colognesi, and J. Tomkinson. A study on the calibration of a time-focused inelastic neutron scattering spectrometer. *Journal of Neutron Research*, 8(4):245–259, 2000.

[24] V.F. Sears. Neutron scattering lengths and cross sections. *Neutron news*, 3(3):26–37, 1992.

[25] G.C. Sterling. International collaboration on advanced neutron sources : proceedings 8th meeting (icans-viii). Technical Report RAL-85-110-2, RAL, Chilton, UK, 1985. Keeble College, Oxford, 8-12th July 1985 : volume 2.

[26] STFC. INES, http://www.isis.stfc.ac.uk/instruments/ines//, June 2014.

[27] STFC. IRIS, http://www.isis.stfc.ac.uk/instruments/iris/, June 2014.

[28] STFC. OSIRIS, http://www.isis.stfc.ac.uk/instruments/osiris/, June 2014.

[29] STFC. Scientific computing technology, http://sct.esc.rl.ac.uk/scarf/index.html, June 2014.

[30] B. Terence, M. Willis, and C.J. Carlile. *Experimental neutron scattering.* Oxford University Press, Oxford, 2009.

[31] C.M. Warsop, D.J. Adams, D.J.S. Findlay, I.S.K. Gardner, S.J.S. Jago, B. Jones, R.J. Mathieson, J. Pasternak, S.J. Payne, and B.G. Pine. Status of injection upgrade studies for the ISIS synchrotron. *Proc. IPAC*, 11:2760, 2011.

[32] P. Willendrup, E. Farhi, K. Lefmann, P.O. Astrand, M. Hagen, and K. Nielsen. User and programmers guide to the neutron ray-tracing package McStas. *Ris DTU*, 2008.

[33] P.K. Willendrup, E. Knudsen, K. Lefmann, E. Farhi, and DTU Risø. Component manual for the neutron ray-tracing package McStas. 2012.

[34] C.G. Windsor. *Pulsed neutron scattering.* Taylor & Francis, 1981.

Nomenclature

EPB	Extracted Proton Beam
HOPG	Highly Oriented Pyrolytic Graphite
INS	Inelastic Neutron Scattering
Linac	Linear Accelerator
MCNP	Monte-Carlo N-Particle Transport
NGS	National Grid Service
PMT	Photomultiplier Tube
PSD	Position Sensitive Detector
RFQ	Quadrupole Radio-Frequency
STFC	Science and Technology Facilities Council
TOF	Time of Flight
TS-1	Target Station 1
TS-2	Target Station 2